ISSN en trámite

Geofísica Internacional

Revista Trimestral Publicada por el Instituto de Geofísica de la Universidad Nacional Autónoma de México

México
Volume 60 Number 4
October -December
2021

— Geofísica Internacional —

GEOFÍSICA INTERNACIONAL, Año 60, Vol. 60, Núm. 4, octubre - diciembre de 2021 es una publicación trimestral, editada por la Universidad Nacional Autónoma de México, Ciudad Universitaria, Alcaldía Coyoacán, C.P. 04150, Ciudad de México, a través del Instituto de Geofísica, Circuito de la Investigación Científica s/n, Ciudad Universitaria, Alcaldía Coyoacán, C.P. 04150, Ciudad de México, Tel. (55)56 22 41 15. URL: http://revistagi.geofisica.unam.mx, correo electrónico: revistagi@igeofisica.unam.mx. Editora responsable: Andrea Rostan Robledo. Certificado de Reserva de Derechos al uso Exclusivo del Título: 04-2022-081610251200-102, ISSN: en trámite, otorgados por el Instituto Nacional del Derecho de Autor (INDAUTOR). Responsable de la última actualización Saúl Armendáriz Sánchez, Editor Técnico. Fecha de la última modificación: 30 de septiembre 2021, Circuito de la Investigación Científica s/n, Ciudad Universitaria, Alcaldía Coyoacán, C.P. 04150, Ciudad de México.

Geofísica Internacional
Vol. 60, Núm. 4, octubre-diciembre de 2021

Contents

Original paper

https://doi.org/10.22201/igeof.00167169p.2021.60.4.1949

Magnetic parameters and paleoclimate: A case study of loess deposits of North-East of Iran

Fereshteh M. Haskouei[1*], Habib Alimohammadian[2], Jafar Sabouri[3]

Recived: March 23, 2019; accepted: May 7, 2021; published online: October 1, 2021.

Resumen

Las técnicas de magnetismo ambiental nos permiten reconstruir las condiciones del paleoclima para obtener resultados como las pérdidas. Las propiedades magnéticas de los minerales se utilizan como sustitutos de los cambios ambientales. En este estudio se investigó la secuencia magnética de loess-paleosol de la sección de Kolet en Neka, al noreste de Irán. Fueron aplicados métodos de magnetismo ambiental para reconstruir los cambios del paleoclima. Se investigó la relación entre los cambios del paleoclima y los proxies del magnetismo ambiental como la variación de la susceptibilidad magnética (χ). Las técnicas de laboratorio indicaron la presencia del factor principal de propiedad magnética en la secuencia de loess-paleosol, como magnetita, maghemita, etc. También, se estimó magnéticamente parámetros (como SIRM, HIRM, etc.) para confirmar concentraciones de partículas tanto eólicas como pedogénicas frente a variaciones de la mejora de la susceptibilidad magnética. Los valores de χ muestran picos prominentes para los tres horizontes de suelos y paleosuelos bien desarrollados, Suelo reciente (S0 por sus siglas en inglés), Paleosol superior (S1, por sus siglas en inglés) y Paleosol inferior (S2, por sus siglas en inglés); que se refieren a condiciones más cálidas y húmedas. Como resultado se obtuvo que el aumento/disminución de la susceptibilidad magnética coincide con la secuencia paleosol-loess, y probablemente con condiciones húmedas/áridas. Además, las variaciones de la susceptibilidad magnética versus la columna litológica de la sección de Kolet permitieron reconocer períodos paleoclimáticos conocidos como ciclos interglaciares/glaciales. Se trazó la variación de la susceptibilidad magnética (MS, por sus siglás en inglés), la magnetización del remanente natural (NRM, por sus siglás en inglés), la susceptibilidad dependiente de la frecuencia (χfd) y de χfd% versus la gráfica litológica del perfil de loess para confirmar que los depósitos de loess/paleosol de la sección de Kolet tienen partículas magnéticas. Luego, aplicamos los datos magnéticos obtenidos como variación de susceptibilidad magnética (MS, por sus siglás en inglés) para indicar que ha habido períodos glaciales/interglaciares durante los últimos 50 ka. Por lo tanto, durante este período de tiempo, hay tres ocurrencias glaciares importantes en el área de estudio. Además, concluimos que no hubo ocurrencia de glaciaciones principales desde los últimos 20.5 ka.

Palabras clave: Magnetismo de Loess, Parámetros magnéticos, Paleoclima, Períodos interglaciares/glaciares, Neka e Irán.

**Corresponding author: haskouei@gmail.com*

[1] *F. Mahdipour. Haskouei is a PhD student of Paleontology, University of Isfahan, Isfahan, Iran*

[2] *H. Alimohammadian is with Geological Survey of Iran, Tehran, Iran*
Instituto Mexicano del Petróleo
México City, México

[3] *J. Sabouri is Principal Investigator palynology of Department of Paleontology, Geological Survey of Iran, Tehran, Iran*

Abstract

Environmental magnetism techniques enable us to reconstruct paleoclimate conditions in some deposition such as losses. The magnetic properties of minerals are used as proxies for environmental changes. For this study, loess/paleosol sequence of Kolet section at Neka, north-east of Iran were magnetically investigated. We applied environmental magnetism methods, to reconstruct paleoclimate changes. We investigated relationship between paleoclimate changes and environmental magnetism proxies like magnetic susceptibility (χ) variation. The laboratory techniques indicated the presence of main factor of magnetic property in loess/paleosol sequence, such as magnetite, maghemite and etc. We also estimated magnetically parameters (like SIRM, HIRM and etc.) to confirm concentrations of both aeolian and pedogenic particles versus variations of magnetic susceptibility enhancement. The χ values show prominent peaks for the three well developed soil and paleosol horizons, Recent Soil (S0), Upper Paleosol (S1) and Lower Paleosol (S2); which refer to warmer and wetter conditions. As result, we concluded that the increase/decreasing of magnetic susceptibility is coinciding with palaeosol/loess sequence, and probably with humid/arid conditions. Moreover, variations of magnetic susceptibility versus lithological column of Kolet section enabled us to recognize paleoclimatically periods known as interglacial/glacial cycles. We plotted variation of magnetic susceptibility (MS), Natural Remnant Magnetization (NRM), Frequency Dependent Susceptibility (χfd) and χfd% versus lithological plot of the loess profile to confirm loess/paleosol deposits of Kolet section bear magnetic particles. Then, we applied the obtained magnetic data as variation of magnetic susceptibility (MS) to indicate that there have been glacial/interglacial periods during over the past 50 ka. Hence, during this period of time, there are three major glacial occurrences in the study area. Also, we conclude there was no main glaciation occurrence since last 20.5 ka.

Key words: Loess Magnetism, Magnetic parameters, Palaeoclimate, Interglacial/glacial periods, Neka and Iran.

Introduction

The northern Iranian loess record is in excellent agreement with the loess record of the Northern Hemisphere, e.g., Europe (Frechen *et al.*, 2003), Central Asia (Frechen and Dodonov 1998; Machalett *et al.*, 2006), or southern Middle Siberia (Frechen *et al.*, 2005). During the 1960s and the 1970s, loess and the intercalated palaeosols were correlated with moist and dry periods of the Holocene (Barbier, 1960; Ehlers, 1971; Frechen, *et al.*, 2009). Generally, little information is available about the climate change in the dry regions of central and northeast Iran, although an argument commonly accepted is that loess accumulated during cold and dry glacial periods and the results of numerous investigations on loess deposits have led to a common acceptance of the close relationship between loess accumulation and soil formation with dry-cold and moist-warm periods, respectively (Karimi, *et al.*, 2009). Similarly, the initial hypothesis of our studies is probably over the past 50ka, loess particles of Kolet Section transported by wind during glacial periods, and then paleosol horizons formed during interglacial periods. First of all we applied some magnetics methods to confirm our deposits bear enough magnetical particles, and it is a good idea to using environmental magnetic proxies such as variation of magnetic susceptibility (MS) to detect glacial/interglacial cycles versus lithological profile.

There is some investigation such as Kehl *et al.* (2005) that inform us the loess record from north of Iran is an excellent archive of climate and environmental changes at least for the past 800ka as demonstrated by up to eight intercalated pedocomplexes in the Neka area. On the other hand there is not any investigation or working on paleomagnetism of Neka loesses. There was some doubt about magnetic capacity of Neka loess for environmental magnetism studies, specially using magnetic susceptibility (χ) curve to detect paleoclimatically changes (glacial/interglacial cycles). In fact, the loess record of Northern Iran perhaps provides a missing link for the correlation between Central Asian and European loess archives, as well as Frechen, *et al.*, 2009 mentioned the Caspian Lowland of Northern Iran is part of the Eurasian loess belt extending from Northwest Europe to Central Asia and China.

This study aims to confirm reconstruction of climatically changes by using magnetic methods and comparing the curves of magnetic parameters together. As have been explained before, little information has been published on records of past climate change in Northern Iran. Moreover, in order to improve the environmental magnetism studies of Iran and reconstruct paleoclimate changes, loess records of northern Iran especially in this area require more information from other field investigations. Actually there is no magnetically investigation on Neka loess has done before; also no investigation of magnetical capacities of loess/paleosol sequences of Iran has been studied. However this study detect the models of paleoclimate changes, by using an environmental magnetism proxy, variation of magnetic susceptibility (χ) curve for Neka loess/paleosol sequence, but it is necessary to assemble more investigation results for this area in the future works.

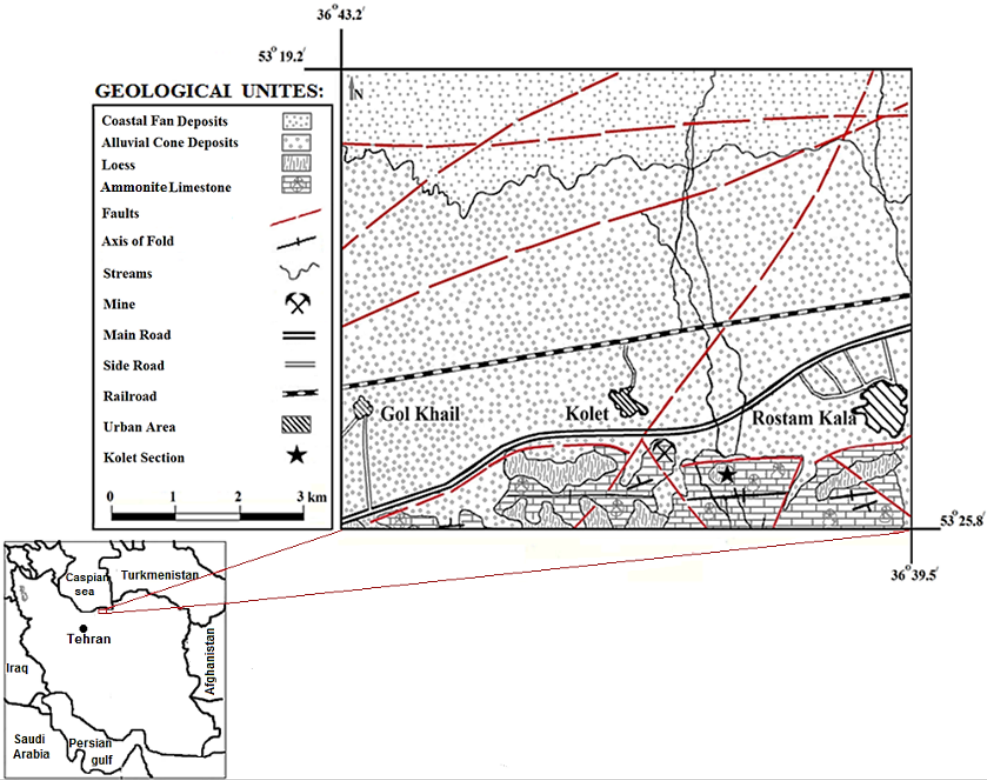

Figure 1. The Geological Map of the study area illustrates Geological structures and lithology of costal and mountainous region (Haskouei and Alimohammadian, 2020).

Study area

The study area is located in the Caspian Lowland of Northern Iran, on the northern foothills of the Alborz Mountains east of Sari (Fig. 1), which is a little piece of loess deposits in the east of north-central of Iran. This zone consists of areas that are located in the north of the Alborz fault, bounded to the north by the Caspian Sea, and the northern coastal plain of Iran, which are covered with thick layers of loess, to the east. Loess profile is found in a mine, on the northern foothills of the Alborz Mountains near the main road of Sari-Behshahr, Mazandaran providence (Fig. 1). The oldest deposits of area are Jurassic limestones and dolomites covered by wind-blown loesses with a significant expansion (Kabirnia *et al.*, 2003), in most parts of study area. Northern of Iran is mentioned by Tietze (1877), Stahl (1923) and Bobek (1937) as little information loess deposits about the nature, origin and chronology of the loess has ever been published. Kehl *et al.*, (2006) studied some part of this area and found several well-developed palaeosol horizons intercalated in the loess record indicate an alternation of comparatively dry and cold climate phases with increased dust accumulation including loess formation, and moist and warm phases with soil formation, respectively. Furthermore, this area was described by Frechen, *et al.* (2009), who suggested that the loess/palaeosol sequences of the Caspian Low land in Northern Iran provide detailed archives of climate and environmental change showing a close relationship to global cooling and warming trends for the late Pleistocene and Holocene period.

The study section which is informally named as Kolet Section falls between 36° 39' 44" N and 53° 23' 56" E. It is situated at about 8 km away of Neka city, almost opposite of Kolet Village, near the main road of Sari-Behshahr, in Mazandaran Province, north of Iran. It is bounded by Alborz fault in the south and Caspian Sea coast line in the north (Fig. 1). Based on field observations, Loess/paleosol sequence followed the paleogeomorphology patterns and deposited on altitudes and lowlands of the older rocks (Fig. 2), which are probably late Jurassic marl limestones, or perhaps the same Ammonite limestone shown in the geological map of the study area (Fig. 1).

OSL dates for studied section are obtained by Kehl, *et al.*, (2005), and described loess/palaeosol sequences a maximum thickness of approximately 20m covers Jurassic limestone of the Alborz front hills. The lithological units are described as the following: 0-2 m is composed of Recent Soil horizon (S0). OSL age of the bottom of S0 is 20.5±2.0ka; 2-8.3 m is Upper Loess with a buffed-yellow color (L1). OSL age of the bottom of L1 is 37.8±3.6ka; 8.3-8.7m is Upper paleosol, a developed narrow paleosol (S1) with a red brown color. From top to bottom of S1, the color becomes light, and pedogenesis become weaker. Second loess deposit is Lower Loess (L2) with buffed-yellow color at the depths from 8.7 to 9.9m; 9.9-10.7m is composed of dark brown paleosol (S2). OSL age of S2 is 48.7±4.7ka (Fig. 2).

Sampling and Methodes

The total number of 117 samples with 10 cm intervals (in thinner layers 5 cm intervals) were collected from loess (paleosol) units (Fig. 3-a to d). Magnetic susceptibility (MS), magnetic mineralogy, Isothermal remnant magnetization (IRM), Saturation Induced Remnant Magnetization (SIRM) carried out on samples. Natural Remnant Magnetization (NRM) was measured, using Spinner (JR-6A). Isothermal Remnant Magnetization (IRM) acquisition experiments were carried out using a Pulse Magnetizer, a T electromagnet and a spinner magneto¬meter. Isothermal Remnant

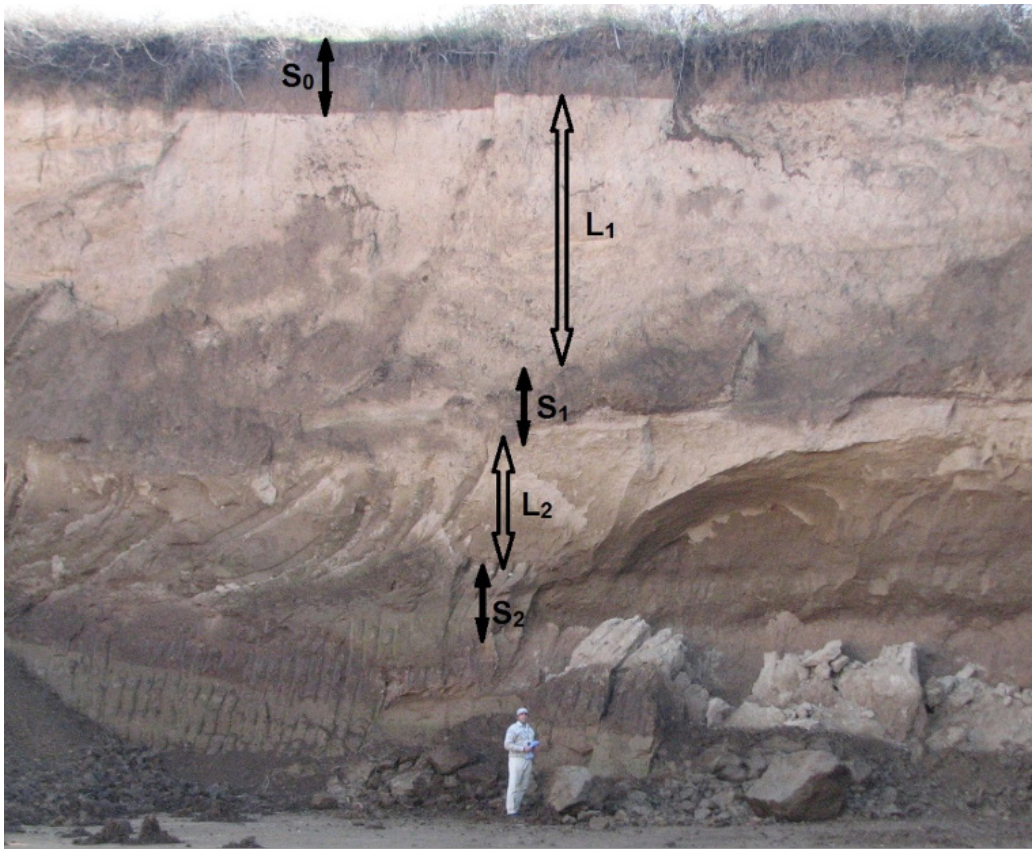

Figure 2. the loess/palaeosol sequence of Kolet section, at Neka, Mazandaran Province, northern of Iran. Black color arrows show two loess sub-divisions (L1 and L2). Upper Palaeosol (S1) is limited between two red lines; and Lower Palaeosol (S2) is under white line; and Recently Soil sub-division (S0) is marked on top, with yellow line (Haskouei and Alimohammadian, 2020).

Figure 3. sampling of loess/paleosol to exactly 117 packs. (a) 10 cm intervals for loess units; (b) 5 cm intervals for paleosol; (c) a good view of Recent Soil and 5 cm intervals for packing ; (d) some pack samples of loess deposits during field working and packing.

Magnetization (IRM) curves acquired in 13 incremental steps up to a maximum field of 800mT, using Pulse Magnetizer (MMPM10). Hence, the intensity of the magnetic field gradually was increased, from 10 mT to 2 T, on 13 steps; and NRM of samples were measured each time, again and again, to calculate Saturation Induced Remnant Magnetization (SIRM). Also, to reveal the presence and kind of magnetic minerals, the AF demagnetization experiments have been applied by using an Alternative Field Demagnetizer, and instantly, the variation of remnant magnetism of samples have been measured again, using a spinner magnetometer. Furthermore, magnetically parameters like S-ratio, HIRM, and S-0.3T were estimated (Tab. 1) to quantify the relative and absolute concentrations of antiferro¬magnetic minerals (e.g., hematite and goethite). It should be noted that, in addition to AF demagneti¬zation experiment, thermomagnetic analysis have been applied aside from the magnetic mineralogy experiment, to confirm the presence and kind of magnetic minerals, using Multi-Function Kappabridge and a thermal furnace is referred to as CS-3.

Also, Magnetic susceptibility of bulk samples, (χ), was measured as main parameter to reconstruct paleoclimate changes, using Multi-Function Kappabridge (MFK1-A). It measured for 117 individual samples were collected from about 10 m profile of Loess/palaeosol sequence (Fig. 4).

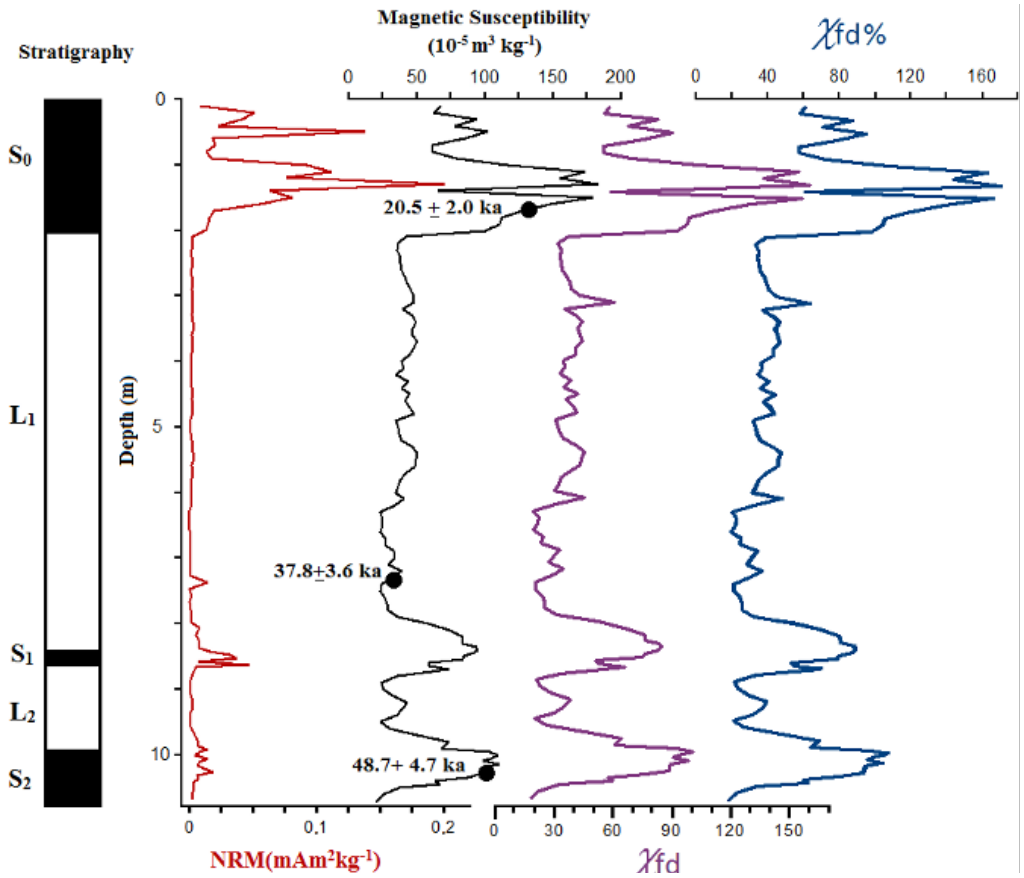

Figure 4. Lithology, Natural Remnant Magnetization (NRM), and Magnetic Susceptibility (χ), Frequency Dependent Susceptibility (χfd) and χ fd% of the loess profile from Kolet Section, at Neka, north-east of Iran. χfd is sensitive to the absolute concentration of superparamagnetic particles; and χ is contributed from both aeolian and pedogenic particles; and χfd% is sensitive to the grain size distribution of superparamagnetic particles. OSL dates (solid circles) for loess/paleosol sequence are from Kehl, *et al.*, (2005). Please refer to text for further description.

Totally, to confirm magnetical capacities of Neka loess magnetical proxies were investigated, such as:

1) Curved Magnetic Susceptibility (χ) to reveal cool/arid (=glacial/perglacial) and humid/warmer (=interglacial) cycles
2) Identity and demonization of size of magnetic minerals by plotting SIRM curve
3) Assessment of magnetic mineralogy in loess and paleosols by estimation of saturation ratio (S-ratio).
4) Investigating of the presence of magnetical particles like magnetite, maghemite and other iron-bearing minerals, to identification of magnetical capacities of loess/paleosol sequences
5) Plotting HIRM and cure to showing the presence of high and low coercivity minerals
6) Plotting χfd% and χfd parameters to reveal presence of viscous magnetical component and grains.

Table 1. Magnetic analysis and measurement such as Magnetic Susceptibility (M.S.), Induced Remnant Magnetization (IRM), SIRM, S-ratio and etc. (LR and UR refer to Lower Red palaeosol and Upper Red palaeosol sub-divisions, respectively). Please refer to text for further description.

Samples No.	Depth (cm)	S-ratio	χ ($10^{-5}m^3kg^{-1}$)	SIRM	S -0.3T	IRM–0.3T	HIRM
KO01	10	0.838721	67	5.506	0.080639	4.618	3.172
KO10	100	0.866991	117	8.225	0.066505	7.131	4.55
KO20	200	0.878472	100	7.776	0.060764	6.831	4.33
KOB10	310	0.850567	48	4.41	0.074717	3.751	2.63
KOB20	410	0.836097	41	4.161	0.081951	3.479	2.5
KOB30	510	0.837142	37	4.157	0.081429	3.48	2.5
KOB40	610	0.840844	41	4.216	0.079578	3.545	2.53
KOB50	710	0.851059	29	4.109	0.074471	3.497	2.5
KOB60	810	0.835368	74	6.961	0.082316	5.815	3.9
KOB66UR	850	0.842847	85	7.165	0.078576	6.039	4
KOB70	870	0.821962	73	5.628	0.089019	4.626	3.225
KOB80	970	0.795291	50	4.162	0.102355	3.31	2.5
KOB83LR	995	0.841182	103	6.498	0.079409	5.466	3.669
KOB90LR	1030	0.851347	96	6.902	0.074326	5.876	3.876
KOB97	1070	0.754974	21	2.865	0.122513	2.163	1.81

Results

1) The χ values show prominent peaks for the three well developed soil and paleosol horizons, (S0), (S1) and (S2); In contrast, the χ curve for Upper Loess (L1) is relatively smoothed. The second Loess horizon (L2), in the 860-990 cm interval, corresponds to a moderate magnetic susceptibility peak (Fig, 4).
2) As figure 4, magnetic enhancement (pedogenic ferrite formation) is evident from increased values of χ and χfd%; and Frequency Dependent Susceptibility (χfd) [percentage or m3kg-1] is variation in χ between low (0.47 kHz) and high frequencies (4.7 kHz).
3) There is determined for 15 representative samples spread throughout the profile (Tab. 1). All samples reach their ultimate maximum values in a field of 300 mT. The backfield necessary to reduce the saturation IRM (SIRM) to zero) fall in the range -30 to -60 mT for most of samples, while the SIRMs themselves range from 2.8 to 8.2 mA m2 kg–1 (Tab. 1).
4) To confirm the presence of ferromagnetic minerals, IRM acquisition experiments were carried out (Fig. 5 and 6). Samples containing ferromagnetic minerals (magnetite) are completely saturated when the magnetic field reaches to less than 2 Tesla (2000 ml); as can be seen on Fig. 5, samples contain ferromagnets particles show steep increases in magnetization with applied field, until reaching saturation magnetization (SIRM).
5) According to figure 6, the discontinuity of the magnetic field line, in the range of -30 to -60 mT, where the magnetic field line is near to reach to zero, indicates the presence of magnetic minerals like magnetite and maghemite. Also, the acquisition (forward direction) and demagnetization (backfield) curves are all similar and are dominated by low-coercivity minerals. All samples reach at least 90 percent of their ultimate maximum values in a field of 300 mT.
6) In figure 7, red diagram is HIRM with sharp increases in three maximum points of the cure for the three well developed soil and paleosol horizons, (S0), (S1) and (S2)
7) Variations of the SIRM showed that the concentration of total ferrimagnetic (ferromagnetic) a material in the paleosols is enhanced (Fig. 7, green colored diagram).
8) The results of thermomagnetic analysis reveal the presence of magnetite as a ferromagnetic (ferrimagnetic) mineral. It is expectable that the ferromagnetic minerals in the magnetic field saturate with less than 1 Tesla for Kolet samples by figuring black colored diagram in figure 7.
9) Total decreasing S-0.3T (from 0.06 to 0.12 A/m) versus total increasing HIRM (from 2 to 5 A/m), shows the amount of low coercivity minerals (including magnetite and maghemite) in the paleosols is much less than high coercivity minerals; and to the contrary, the amount of low coercivity minerals in loess horizons, is much more than high coercivity minerals (Fig. 7).
10) All data and results of magnetism methods, above all variation of Magnetic susceptibility (MS) curve confirm loess-paleosol sequences of Kolet section as suitable sediments with enough magnetic particles capacity (Fig.8).

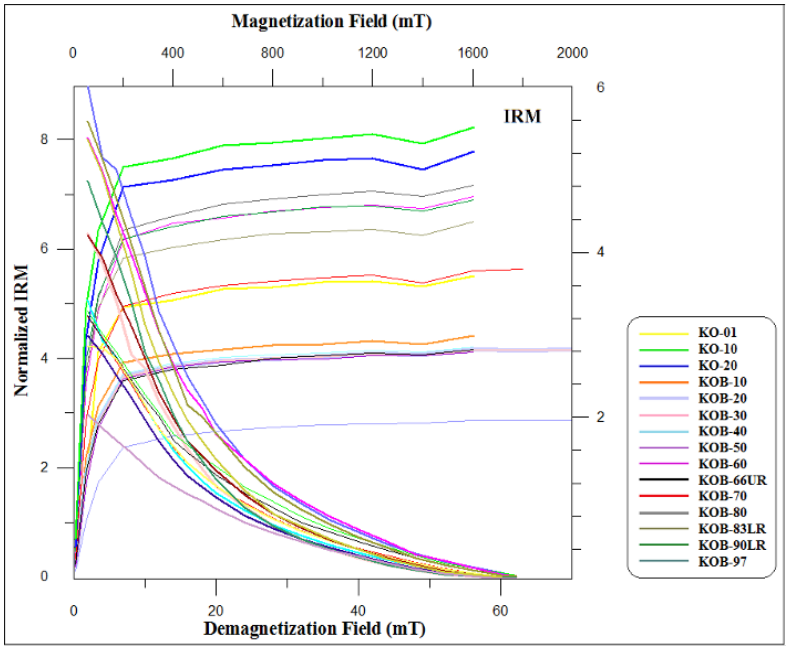

Figure 5. Variations of the Isothermal Remnant magnetization (IRM) versus demagnetization field, for 15 samples in Tab. 1; the rising lines on the left of the graph, starting from zero, curved near 300mT which represent the magnetic saturation of the samples; completely saturation of Kolet samples, acquired at about 1600 mT; and the downward-curved lines to the right of the graph, which are zero at about 60 degree, indicating the AF demagnetization of samples.

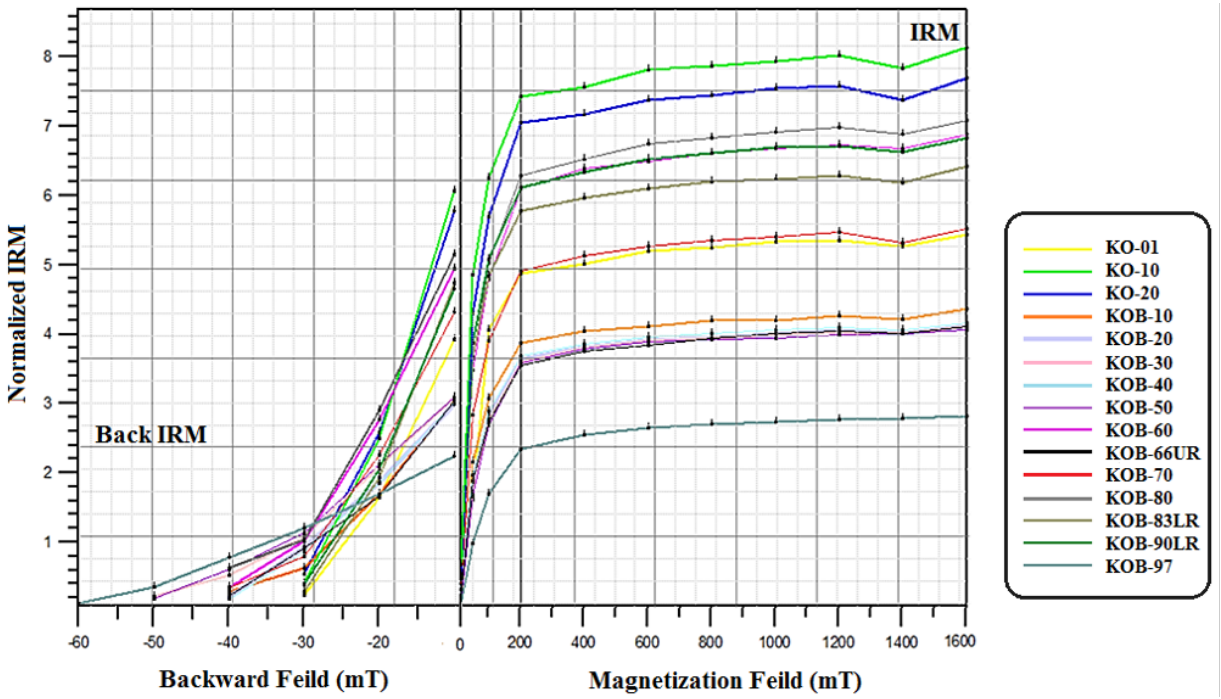

Figure 6. Variations of the Isothermal Remnant magnetization (IRM) versus backward field, for 15 samples in Tab. 1; the rising lines on the right of the graph, starting from zero, curved near 300 mT which represent the magnetic saturation of the samples; and the downward-curved lines to the left of the graph, which are zero in the range of -30 to -60 mT, indicating the back IRM.

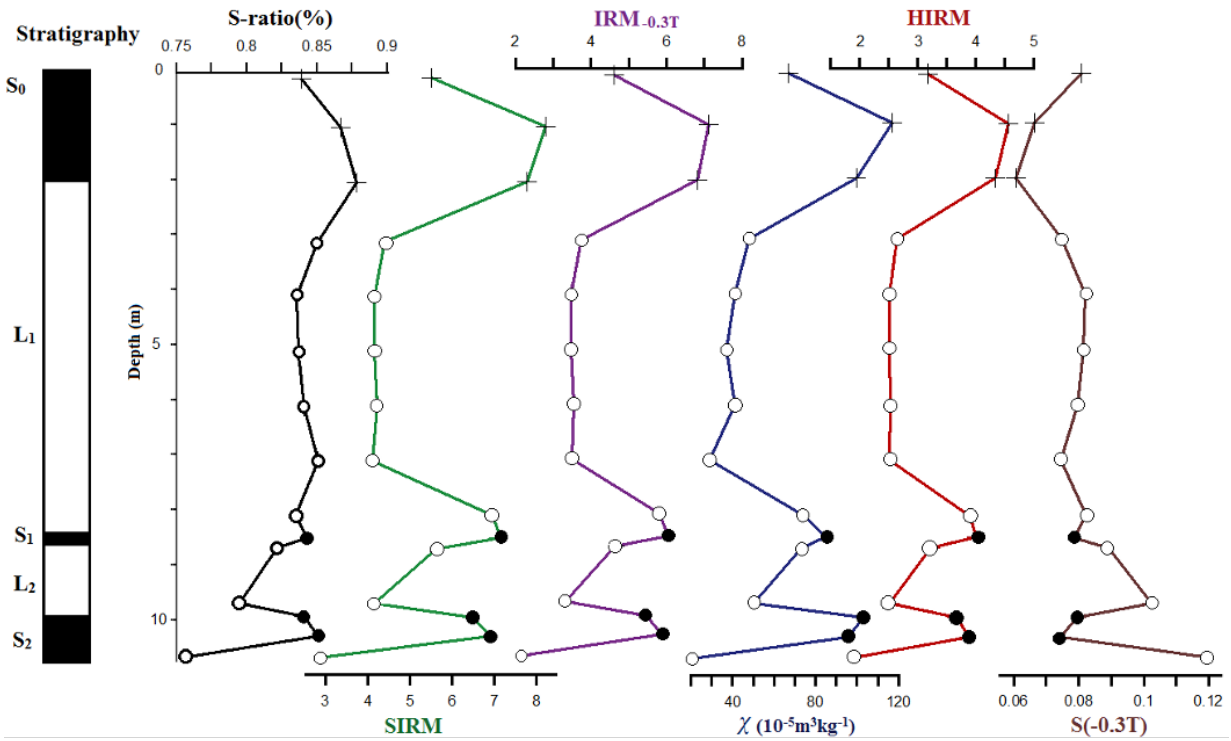

Figure 7. Variations of the IRM saturation ratio (S ratio %), and SIRM (IRM at 2T), Magnetic Susceptibility (χ), and IRM0.3T, and HIRM and the mineral-magnetic parameter S–0.3T, for 15 selected samples (Tab. 1), in the Kolet Loess-Paleosol sequence. Open circles: loess data, closed circles: paleosol data, crossed-out symbols: Recent Soil data. The IRM–0.3T denotes 0.3T back-field IRM values. Please refer to text for further description.

Discussion

Many environmental scientists are familiar with the use of one magnetic parameter, magnetic susceptibility, measurements of magnetic susceptibility are normally just the first, and most basic, step in characterising the magnetic properties of any sample (Maher, 2011). The very comprehensive and detailed study of Liu *et al.*, (1985) verified that highs and lows of the susceptibility curves are closely correlated with the occurrence of paleosols and loess layers, respectively (Heller and Liu, 1984; Heller *et al.*, 1991). Briefly, Less-weathered loess sequences, therefore, represent an arid and probably cool (=glacial/perglacial) climate during their accumulation, while the paleosols correspond to a more humid and warmer (=interglacial) climate (Akram, *et al.*, 1998).

Maher (1998) mentioned that Magnetite and maghemite are responsible for most of the signal because their susceptibility is three orders of magnitude greater than that of other iron-bearing minerals such as goethite, hematite, lepidocrocite and ferrihydrite.

IRM and back-field IRM values yield useful parameters for estimating the enrichment of low coercivity or high coercivity minerals in the samples. To make a simple statement, the IRM and back-IRM acquisition experiments acquired under the 2.5T revealed the presence of magnetite/maghemite along with some high coercive mineral, maybe goethite. Also, saturation isothermal Remnant magnetization (SIRM) crossover plots are a simple way of determining the identity and domain size of magnetic minerals, through the use of SIRM acquisition and demagnetization curves

and the position of the crossover point of the curves. Also, SIRM is a concentration-dependent parameter, i.e. it is high if the amount of ferromagnetic material present is high and vice versa (Szabo and Cioppa, 2004; Akram *et al.*, 1998).

Jin and Liu (2011) mentioned, whenever the IRM acquisition curves with similar shapes for all samples; and it climbs rapidly below 200 mT and reaches approximate saturation at about 300 mT; this behavior reveals the existence of soft magnetic minerals, such as magnetite and/or maghemite. They suggested that for loess samples, the IRM curves show slight increases from 300 mT up to 2 T, indicating presence of hard magnetic components, such as hematite and/or goethite.

In the other words, the sudden rise below 300 mT in all of the IRM acquisition curves indicates the presence of low coercivity minerals, like magnetite and/or maghemite. The unsaturated component (>300 mT) is carried by a high coercivity mineral, possibly goethite (Akram, *et al*., 1998).

The saturation ratio (S-ratio) is a parameter to assess magnetic mineralogy in loess and paleosols; and where "S" is the absolute value of the IRM remaining after exposure to a reversed field of 0.3 T divided by the saturation IRM (or SIRM), which is usually acquired in a field of 1–2T. This parameter is calculated from IRM-0.3T/SIRM and represents the properties of magnetic minerals; and it is also serves as a measure of the proportion of high coercivity minerals (i.e., hematite and goethite) to low coercivity minerals (i.e., magnetite and maghemite) in a material (King and Channell, 1991; Roberts *et al.*, 1995; Verosub and Roberts, 1995). For most samples, the "S" values are close to 1, suggesting low-coercivity and ferri-magnetic mineralogy (Deng *et al.*, 2004; Akram *et al.*, 1998).

Next parameter is HIRM, a measure of the concentration of high coercivity minerals which its values become large if high coercivity minerals are relatively abundant. Another parameter, S–0.3T is a contrasting measurement to indicate the relative abundance of low coercivity mineral (Bloemendal *et al.*, 1992; Akram *et al.*, 1998). Sharp increases in magnetic susceptibility and in HIRM indicate enhanced aeolian influx of ferrimagnets and of haematite/goethite, respectively (Maher, 2011).

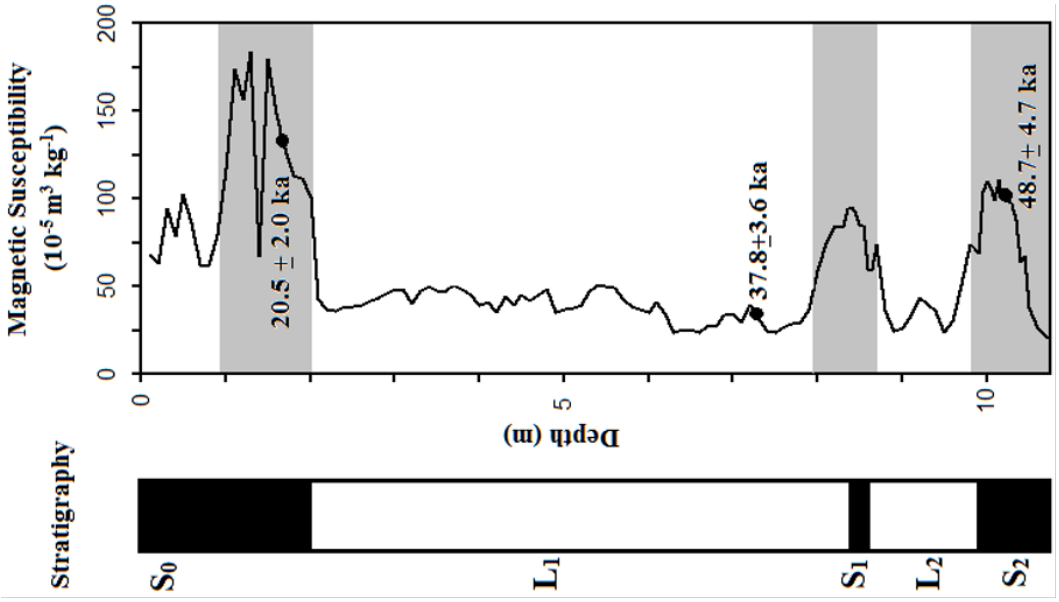

Figure 8. Variation of MS for loess-paleosol sequences of Kolet section, NE of Iran.

Also, it is well accepted that whenever χfd%, measured between ~10% or 5-10%, it would indicate a large fine viscous (magnetite) component of SP range; and χfd indicates viscous grains at the superpara¬magnetic/stable single-domain boundary; and χfd% is a sensitive parameter for detecting the presence of SP grains in soils (Maher, 1988, 2011). In the other words, χfd is sensitive to the absolute concentration of SP particles; χ is contributed from both aeolian and pedogenic particles; and χfd% is sensitive to the grain size distribution of SP particles. Hence, Very special adjustment of the grain size distribution is needed to keep both the linear relationship between χfd and χ and the constant χfd% (Liu *et al.*, 2004c).

Conclusion

(1) χ and χfd and χfd% show a perfect linear correlation and a high degree of similarity, in their variations and as we mentioned before, the χ values show prominent peaks for the three well developed soil and paleosol horizons, Recent Soil (S0), Upper Paleosol (S1) and Lower Paleosol (S2); which refer to the presence and concentration of single domains magnetic minerals such as magnetite and maghemite.

(2) The results of Environmental magnetism techniques confirmed increasing/decreasing of magnetic susceptibility plot, as instance the results of the magnetic mineralogy experiment indicated the presence of ferromagnetic such as magnetite in the samples, which is the main factor of magnetic property in loess/paleosol sequence. Also, IRM and SIRM diagrams, and variations of magnetically parameters like HIRM and S-0.3T indicated the presence of low coercivity minerals such as magnetite in loess accumulations more than high coercivity minerals. The presence of high coercivity minerals like hematite, indicate weathered conditions for paleosols horizons. On the other hand, the results of both Back-field and Frequency Dependent Susceptibility (χfd) diagrams indicated the presence of single domains magnetic minerals like magnetite.

(3) The obtained magnetic data indicate that over the past 50 ka, there have been at least two glacial/interglacial periods in the study area and since last 20 ka, there was no glaciations in the study area to produce loess deposits. The χ values show prominent peaks for the three well developed soil and paleosol horizons, Recent Soil (S0), Upper Paleosol (S1) and Lower Paleosol (S2); which probably refer to warmer and wetter conditions of interglacial periods.

(4) Increasing/decreasing of magnetic susceptibility probably is coinciding with palaeosol/loess and interglacial/glacial cycles, respectively, which means probably Loess was transported and deposited during cooler, drier periods; after then paleosols formed when the climate became warmer and wetter in northern Iran.

Acknowledgements

The authors gratefully acknowledge support of the Head of the Department of Geology and Exploration, Mineralogy of the country, Head of Geosciences Research Institute, Managing Director of Marine Geology and other colleagues, Managing Director of Laboratory Affairs of the Geological Survey and my dear colleagues, including Ms. Dehghan, Ms. Rahimzadeh and Mr. Moeini for their support and laboratory facilities.

References

Akram, H., Yoshida, M., & Ahmad, M.N., (1998). Rock magnetic properties of the late Pleistocene Loess–Paleosol deposits in Haro River area, Attock basin, Pakistan: Is magnetic susceptibility a proxy measure of paleoclimate. *Earth Planets Space*, Vol. 5, pp. 129–139

Barbier, R., (1960). Decouverte de l'effet d'une ancienne vallée de remblai dans le cours inférieur du Sefid-Roud (versant nord del'Elbourz, Iran). *Comptes Rendus de l'Academie des Sciences Paris* 250, 1097–1098.

Bloemendal, J., J. W. King, F. R. Hall, and S. J. Doh, (1992). Rock magnetism of late Neogene and Pleistocene deep-sea sediments: Relationship to sediment source, diagenetic processes, and sediment lithology, *J. Geophys. Res.*, 97, 4361–4375.

Bobek, H. (1937): Die Rolle der Eiszeit in Nordwestiran. – Z. Gletscherk., 25: 130-183, 13 Abb., 17 Photos; Berlin Zehlendorf.

Deng, C., Zhu, R., Verosub, K.L., Singer, M.J., and Vidic, N.J., (2004). Mineral magnetic properties of loess/paleosol couplets of the central loess plateau of China over the last 1.2 Myr. *Journal of Geophysical Research*, Vol. 109, pp. 1–109.

Ehlers, E. (1971): Sudkaspisches Tiefl and (Nordiran) und Kaspisches Meer. Beitrage zuihrer Entwicklungsgeschichte im Jung- und Postpleistozan. – Tubinger Geogr. Stud., 44, 184 S., 54 Fig., 29 Photos; Tubingen.

Frechen, M., Dodonov, A., (1998). Loess chronology of the middle and upper Pleistocene in Tajikistan. *International Journal of Earth Sciences* 87, 2–20.

Frechen, M., Oches, E.A., Kohfeld, K.E., (2003). Loess in Europe – mass accumulation rates during the last glacial period. *Quaternary Science Reviews* 22, 1835–1857.

Frechen, M., Zander, A., Zykina, V., Boenigk, W., (2005). The loess record from the section at Kurtak in Middle Siberia. *Palaeogeography, Palaeoclimatology, Palaeoecology* 228, 228–244.

Frechen, M., Kehl, M., Rolfa, C., Sarvati, R., Skowronek, A., (2009). Loess chronology of the Caspian Lowland in Northern Iran. Quaternary International 198, 220–233.

Haskouei F. M., and Alimohammadian, H., (2020), The Magnetic Susceptibility of the Late Quaternary Loess in North-East of Iran and Its Correlation with Other Palaeoclimatical Parameters: World Academy of Science, Engineering and Technology, *International Journal of Geological and Environmental Engineering*, Vol:14, No:2, Fig. 1.

Heller, F., Liu, T.S., (1984). Magnetism of Chinese Loess deposits. Geophysical Journal of the Royal Astronomical Society 77, 125.

Heller, F., Liu, X.M., Liu, T.S., Xu, T.C., (1991). Magnetic-susceptibility of Loess in China. *Earth and Planetary Science Letters* 103, 301–310

Jin, C., and Liu, Q., (2011). Remagnetization mechanism and a new age model for L9 in Chinese loess. Physics of the *Earth and Planetary Interiors*. doi: 10.1016/j.pepi.2011.03.010

Kabirnia, A. R., Asadi, A., Khan Nazari, N. E., Vakili, F, Bahremand, M., Masoumi, R. And Qomishi, A., (2003). 1:100,000 scale geology map of Sari, Geological Survey of Iran (in Persian).

Karimi, A., Frechen, M., Khademi, H., Kehl, M., Jalalian, A., (2009). Chronostratigraphy of loess deposits in northeast Iran, Quaternary International, 1–9. doi:10.1016/j.quaint.2009.08.002

Kehl, M., Sarvati, R., Ahmadi, H., Frechen, M., Skowronek, A., (2005). Loess paleosol–sequences along a climatic gradient in Northern Iran. *Eiszeitalter und Gegenwart* 55, 149-173.

Kehl, M., Sarvati, R., Ahmadi, H., Frechen, M., Skowronek, A., (2006). Loess/paleosol-sequences along a climatic gradient in Northern Iran. *Eiszeitalter und Gegenwart* 55, 149–173.

King, J.W., and Channell, J.E.T., (1991). Sedimentary magnetism, environmental magnetism, and magnetostratigraphy. *Review Geophysical*, Vol. 34, pp. 358–370

Liu, T. S. *et al.*, (1985). Loess and the Environment. *China Ocean Press*, Beijing, 1-251.

Liu, Q.S., Jackson, M.J., Yu, Y., Chen, F., Deng, Ch., and Zhu R., (2004c). Grain size distribution of pedogenic magnetic particles in Chinese loess/paleosols. *Geophysical Research Letters*, 31, 506–514

Machalett, B., Frechen, M., Hambach, U., Oches, E.A., ZÖller, L., Markovic, S.B., (2006). The loess sequence from Remisowka (northern boundary of the Tien Shan Mountains, Kazakhstan) – part I: luminescence dating. *Quaternary International* 152/153, 192–201.

McLaren, P., (1980). "An Interpretation of Trends in Grain Size Measures". *Journal of Sedimentary Petrology* 51(2), 611-623.

Maher, B. A., (1988). Magnetic properties of some synthetic sub-micron magnetites. *Geophys. J.*, 94, 83 – 96.

Maher, B.A., (1998). "Magnetic properties of modern soils and Quaternary loessic paleosols:Paleoclimatic implications", *Palaeogeography Palaeoclimatology Palaeoecology*, Vol. 137, 25–55.

Maher, B. A., (2011). The magnetic properties of Quaternary Aeolian dusts and sediments, and their Palaeoclimatic significance. *Aeolian Research*, 145-387.

Roberts, A.P., Cui, Y., and Verosub, K.L., (1995), Wasp–waisted hysteresis loops: Mineral magnetic characteristics and discrimination of components in mixed magnetic systems. Journal of Geophysical Research, Vol. 100, pp. 17909–924

Robinson, S. G., (1986). The late Pleistocene paleoclimatic record of North Atlantic deep-sea sediments revealed by mineral-magnetic measurements, Phys. *Earth Planet. Inter.*, 42, 22–47.

Stahl, A.F.v. (1923): Zur Frage der Losbildung. – Z. dt. geol. Ges., 74: 320-325; Stuttgart.

Szabo, E.; and Cioppa, M. T. (2004). Saturation Isothermal Remnant Magnetization Crossover Plots: Case Study for a Bimodal Population of Low and High Coercivity Magnetic Minerals. American Geophysical Union, Spring Meeting 2004, abstract id. GP34A-06.

Tietze, E. (1877): Uber Lossbildung und uber die Bildung von Salzsteppen. – Verh. k. u. k. geol. Reichsanstalt, 15: 264-268; Berlin.

Verosub, K.L., and Roberts, A.P., (1995), Environmental magnetism: Past, present, and future. *Journal of Geophysical Research*, Vol. 100, pp. 2175–2192

Original paper

https://doi.org/10.22201/igeof.00167169p.2021.60.4.2118

Micromechanical modeling of ultrasonic velocity for pore-structure and porosity characterization considering anisotropy in carbonate samples

J. Mena-Negrete[1], O. C. Valdiviezo-Mijangos[2], E. Coconi-Morales[2]* and R. Nicolás-López[3].

Recived: November 24, 2020; accepted: May 3, 2021 ; published online: October 1, 2021.

Resumen

En este trabajo se presenta un enfoque para caracterizar la estructura de poros y la anisotropía en muestras de carbonatos basado en el Método del Medio Efectivo (EMM) dinámico. Este considera una matriz con inclusiones elipsoidales que inducen una anisotropía transversal. Se estiman las velocidades de onda compresional (V_P), de cizalla vertical (V_{SV}) y horizontal (V_{SH}) teniendo en cuenta parámetros como longitud característica, frecuencia, ángulo de incidencia de la onda, razón de aspecto, mineralogía y tipo de fluido en los poros para predecir la forma de poro en carbonatos. Se muestran rangos de razones de aspecto para discriminar los diferentes tipos de poro: intercristalinos, intergranulares, móldicos y vugulares. El ángulo de incidencia de la onda es un parámetro que influye en la estimación de V_P (0°,45°,90°), V_{SV} (0°) y V_{SH} (90°) para calcular el módulo de Young anisótropo dinámico (E_{33}) y la relación de Poisson (υ_{31}), así como los parámetros de Thomsen, ε, γ y δ para cuantificar la anisotropía inducida por la estructura de poros. Los resultados obtenidos establecen que el tamaño y estructura de poro tienen un impacto muy significativo en las propiedades elásticas cuando la porosidad tiene valores mayores al 4% para los tres rangos de frecuencia, ultrasónica, sónica y sísmica. En esta investigación se predice la estructura y el tamaño de los poros para mejorar la caracterización y el modelado de propiedades elásticas de los yacimientos carbonatados. La validación de los resultados incluye la comparación con mediciones de porosidad y datos de velocidad ultrasónica para diferentes muestras de carbonatos.

Palabras clave: anisotropía, velocidad ultrasónica, estructura y geometría de poro, rocas carbonatadas.

*Corresponding author: ecoconi@imp.mx

[1] *Postgraduate Program of Instituto Mexicano del Petróleo*
Eje Central Lázaro Cárdenas Norte 152, Gustavo A. Madero,
San Bartolo Atepehuacan, 07730 Mexico City, Mexico.

[2] *Instituto Mexicano del Petróleo*
Eje Central Lázaro Cárdenas Norte 152, Gustavo A. Madero,
San Bartolo Atepehuacan, 07730 Mexico City, Mexico.
Instituto Politécnico Nacional, ESIA Ticomán
Calz. Ticomán 600, San José Ticomán, Gustavo A. Madero,
07340 México City, Mexico

[3] *Instituto Mexicano del Petróleo*
Eje Central Lázaro Cárdenas Norte 152, Gustavo A. Madero,
San Bartolo Atepehuacan, 07730 Mexico City, Mexico.
División de estudios de Posgrado de la Facultad de Ingeniería,
Universidad Nacional Autónoma de México.
Ciudad Universitaria, Delegación Coyoacán, 04510,
Mexico City, Mexico.

O. C. Valdiviezo-Mijangos, email: ovaldivi@imp.mx
R. Nicolás-López, email: rnlopez@imp.mx

Abstract

This work presents an approach to characterize the pore-structure and anisotropy in carbonate samples based on the Effective Medium Method (EMM). It considers a matrix with spheroidal inclusions which induce a transverse anisotropy. The compressional wave (V_P), vertical (V_{SV}) and horizontal (V_{SH}) shear wave velocities are estimated, taking into account parameters as characteristic length, frequency, wave incidence angle, aspect ratio, mineralogy, and pore-filling fluid to predict pore shape in carbonates. Ranges of aspect ratios are shown to discriminate different pore types: intercrystalline, intergranular, moldic, and vuggy. The wave incidence angle is a determinant parameter in the estimation of V_P (0°,45°,90°), V_{SV} (0°) and V_{SH} (90°) to calculate dynamic anisotropic Young's modulus (E_{33}) and Poisson's ratio (υ_{31}), together with the Thomsen parameters, ε, γ, and δ for quantification of the anisotropic pore-structure. The obtained results establish that the size and the pore-structure have a more significant impact on the elastic properties when the porosity takes values greater than 4% for the three ranges of frequency, ultrasonic, sonic, and seismic. This investigation predicts the pore-structure and pore-size to improve the characterization and elastic properties modeling of carbonate reservoirs. The validation of results includes porosity measurements and ultrasonic velocity data of different carbonate samples.

Keywords: anisotropy, ultrasonic velocity, pore-structure and carbonate rocks.

1. Introduction

Some approaches to characterize siliciclastic reservoirs have limited carbonate applications (Gupta and Gairola, 2020) because carbonates are highly heterogeneous, chemically reactive, and have complex porosity structures (Akbar *et al.*, 1995). Diagenetic processes such as cementation and dissolution control the carbonates' elastic behavior (Anselmetti and Eberli, 1993, Eberli *et al.*, 2003, Brigaud *et al.*, 2010, Fournier *et al.*, 2014, Hairabian *et al.*, 2014). For the static characterization of carbonate reservoirs, the elastic properties play a significant role because they are linked to the wavelength from different frequencies: seismic, sonic, and ultrasonic. A critical issue is the effects of the frequency dependence on the characterization models, which is very useful, in static and dynamic properties relationships, for more realistic wave propagation simulations in rocks (Panizza and Ravazzoli, 2019).

The relationships between P- and S- wave velocities and porosity are highly variable in carbonates and, therefore, each geological environment must be separately characterized (Miller, 1992). Porosity, pore type, fluid-filled pore, mineralogy, and density affect wave velocities (Anselmetti and Eberli, 2008). On the other hand, pore geometry is a crucial factor since it is responsible for the significant scattering in velocity values at a given porosity in carbonates (Eberli *et al.*, 2003).

Several investigations have been carried out in carbonates to determine relationships between velocity, porosity, pore type (Anselmetti and Eberli, 1997, Eberli *et al.*, 2003), and pore-structure (Assefa *et al.*, 2003, Weger *et al.*, 2009). For this reason, the thin sections are used to measure the pore aspect ratio; which in turns supports the investigations about the relationship between compressional (V_P) and shear (V_S) wave velocities of rocks with pore geometries. The thin sections are two-dimensional representations of the rock body in three dimensions (Assefa *et al.*, 2003). Another method for velocity estimation from thin section images is based on numerical modeling using finite difference schemes for acoustic wave propagation; this involves neural networking to compute the pore aspect

ratio (Wardaya *et al.*, 2014). The Digital Image Analysis (DIA) technique has also been applied to quantify the pore geometry's effects on wave velocities (Weger *et al.*, 2009). Both fracture porosity and aspect ratio influence P- wave and two polarized S- wave velocities. These were analyzed using a two-layer physical model with a vertical fracture system. The results indicated that the wave velocities usually increase when the fracture aspect ratio is also increased (Li *et al.*, 2016).

Another research area to predict the relationship between the pore shapes and velocities is based on self-consistent methods, which are efficient tools for estimating effective elastic moduli of two-phase composites (matrix and inclusions). The pioneering works of Budiansky (1965) and Hill (1965) presented self-consistent solutions to estimate macroscopic elastic moduli considering polycrystals and a matrix. Their analysis was based on Eshelby's (1957) investigation for the self-consistent analysis of spherical inclusions embedded in a matrix. Later, O'Connell and Budiansky (1974) extended the self-consistent method for ellipsoidal cracks.

The prediction of the microporosity aspect ratio has been possible to compare the ultrasonic velocities, Digital Image Analysis (DIA) from thin sections, and velocities obtained by Differential Effective Method (DEM). The microporosity effective aspect ratio has been quantified with a minimum error method between the compressional wave velocity measurement and those velocities estimated by DEM. This method enables the pore-geometry characterization from elastic properties measured in carbonate grainstone samples (Lima *et al.*, 2014).

Effective properties have been estimated for microporous cemented grainstone with porous micritic grains of spherical shapes embedding in a non-porous sparry calcite cement. The micritic grains consider spheroidal inclusions within a calcareous host. The grain property and the whole-rock property were modeled with DEM and Self-consistent approximation (SC), respectively. The Equivalent Pore Aspect Ratio (EPAR) was derived from fitting laboratory measurements of velocities with the previous models (Fournier *et al.*, 2011). EPAR was presented as a tool for identifying the dominant pore from velocity and porosity measurements in limestone (Fournier *et al.*, 2014). EPAR has also been modeled using DEM and Keys-Xu approximation. This parameter permits classifying three carbonate groups that reveal a petrophysical indicator representing the pore geometry and their relationship with elastic properties (De Assis *et al.*, 2017, Fournier *et al.*, 2018).

The frequency impact in the estimation of V_P and V_S wave velocities with the effective medium theories have been evaluated by adjusting estimated velocities with the measured velocities from physical models, which consider different crack density and ultrasonic frequencies (100, 250, and 500 kHz). The best matching was reached by the Hudson method at 500 kHz. The velocity measurements decrease while the frequency decreases as the crack density increases (Shuai *et al.*, 2020).

The self-consistent methods usually predict effective elastic moduli of an isotropic medium, although carbonate rocks are anisotropic. Therefore, these models should include the influences of anisotropy, pore sizes, and frequency to gain more representativeness for carbonate reservoir characterization.

In this paper, a new application of the Effective Medium Method (EMM) which considers anisotropy, frequency, and other parameters, is used to model the compressional and shear wave velocities taking into account fluid-saturated carbonate samples to predict pore-structure. The parameters such as characteristic length, wave incidence angle, aspect ratio, mineralogy, and pore-filling fluid, play an important role in describing it. This research includes the validation of results based on experimental data of ultrasonic velocities in carbonate samples which are classified as intercrystalline, intergranular,

moldic, and vuggy pores. The governing equations for the self-consistent scheme by Sabina *et al.* (1988, 1993, 2015) are described in Section 2. The Scanning Electron Microscope (SEM) and Photomicrograph images are used to study the pore's structures in carbonate rocks (Section 3). A case study shows the rock samples' location used to validate this research (Section 4). In Section 5, the results of velocity modeling (V_P, V_{SV} and V_{SH}) and pore-structure prediction in carbonates are presented at different frequencies. The anisotropy analysis is also included where Young's modulus (E_{33}) and the Poisson's ratio (υ_{31}), as well as Thomsen's parameters (ε, γ and δ) are estimated. This work concludes with a discussion of parameters that chiefly affect the wave velocities' propagation in carbonate reservoirs (Section 6).

2. The Effective Medium Method (EMM) applied to anisotropy modeling

Different methods have been used to model heterogeneous medium considering inclusions embedded in a matrix; these inclusions can be solid- or fluid-filled pores. Various geometries of inclusions have been considered, and their effective properties have been estimated using a homogenization process. For example, O'Connell and Budiansky (1974) considered a homogenization method on a self-consistent approximation with a crack density parameter. The Kuster-Toksöz method (1974) neglects the interaction between inclusions. In spite of, the non-interaction assumption is not valid at a high concentration of inclusions or with porosities more significant than 20% (Berryman and Berge, 1996). The Differential Effective Medium (DEM) scheme (Cleary *et al.*, 1980, McLaughlin, 1977, Norris, 1985, Zimmerman, 1991) considers an iterative homogenization process until the inclusions' concentration of the modeled composite is reached. Berryman's method is a variation of the Kuster and Toksöz method to minimize the multiple scattering effects on a simpler scheme (Berryman, 1980).

The self-consistent methods mentioned above have been used to obtain effective moduli from a two-phase medium's macroscopic properties. Sabina and Willis (1988) extended the static model of Budiansky (1965) and Hill (1965) to estimate dynamic properties; from these, they determined scattering and attenuation patterns of heterogeneous media with spherical inclusions, which lead to isotropic medium.

Hudson (1980, 1981) based on scattering theory, proposed a method to determine effective moduli for an anisotropic medium (transversely isotropic medium), assuming aligned inclusions which can be fluid-filled, dried, or filled with a weak material when a dilute distribution of cracks is considered. Sabina *et al.* (1993, 2015) presented a model to estimate effective dynamic properties for transverse isotropic composites. In these models, aligned spheroidal inclusions are considered. The self-consistent method assumes a single scattering problem whose solutions will depend on the inclusion shape, size, and quantity. In this way, effective moduli are determined from the frequency and mechanical properties of the matrix and constituents. From these effective moduli and the inclination angle of the inclusions, it is possible to estimate a compressional (V_p) wave velocity, horizontally (V_{SH}) and vertically (V_{SV}) polarized shear wave velocities (Figure 1a).

This work presents the equations by Sabina *et al.* (1993, 2015) to predict anisotropic elastic moduli, Thomsen parameters, and pore-structure of carbonate rocks. The effective elastic moduli (c_0) and the effective density (ρ_0) for a transversely isotropic medium are:

$$c_0 = c_{n+1} + \sum_{r=1}^{n} \phi_r h_r(k\boldsymbol{s}) h_r(-k\boldsymbol{s})(c_r - c_{n+1}) \left[I + \overline{T}_x^{(r)} (c_r - c_0) \right]^{-1} \tag{1}$$

$$\rho_0 = \rho_{n+1} + \sum_{r=1}^{n} \phi_r h_r(k\boldsymbol{s}) h_r(-k\boldsymbol{s})(\rho_r - \rho_{n+1}) \left[I + \overline{Q}_T^{(r)} (\rho_r - \rho_0) \right]^{-1} \tag{2}$$

where ϕ_r is the volume fraction of the inclusions (r), n is the number of inclusions embedded in the medium, k corresponds to the propagation's wavenumber in the heterogeneous medium, $\boldsymbol{s}$ is the unit vector, I is the identity matrix, $\overline{T}_x^{(r)}$ and $\overline{Q}_t^{(r)}$ result from differentiating symmetric and asymmetric Green's function respectively (Sabina *et al.*, 2015), c_r is the tensor of elastic moduli of inclusions (r), ρ_r is the density for each inclusion and h_r ($k\boldsymbol{s}$) is defined as:

$$h_r(ks) = \frac{1}{|\Omega_r|} \int_{\Omega_r} e^{(iks \cdot x)} dx, \tag{3}$$

from the latter equation, Ω is:

$$\Omega = \left\{ \mathbf{x} : x_1^2 + x_2^2 + \frac{x_3^2}{\alpha^2} < a^2 \right\}, \tag{4}$$

where a is the inclusion radius of the x_1, x_2 plane and α is the aspect ratio which is defined as the quotient of the semi-axis in x_3 (b) and semi-axis in the x_1, x_2 plane, $\alpha = b/a = 1$ refers to a sphere; $\alpha > 1$ represents a prolate spheroid, and an oblate spheroid considers $\alpha < 1$ (Figure 1a).

The size of the inclusions depends on the volume fraction, their radius (a) and aspect ratio (α). The dimensions of the inclusions are given by a characteristic length $\beta = 2a$ which is related to the response of the elastic properties (Figure 1b), depending on the wavelength at different frequencies; ultrasonic, sonic, and seismic. The dimensionless frequency is calculated with matrix compressional wave velocity (V_m), frequency (f) and inclusions radius as:

$$\varpi = \frac{2\pi a f}{V_m}. \tag{5}$$

Based on Kinra and Anand (1982), there is a parameter of the layer thickness connected with the long-wavelength resolution that relates radius a with the semi-axis b of an ellipsoidal inclusion embedding in a layer with a porosity (ϕ):

$$L_r = a^{2/3} \left(\frac{4\pi b}{3\phi} \right)^{1/3} \tag{6}$$

If b=a, then the shape of the inclusions is spherical. It means that there is a dependence between the radius of the inclusions and the frequency associated with different sizes of these employing a scaling factor throughout the frequency band (Valdiviezo-Mijangos and Nicolás-López, 2014, Valdiviezo-Mijangos *et al.*, 2020).

Figure 2 shows the flow chart for solving Eqs. 1 and 2. These equations are a system of nonlinear equations of the complex variable for each frequency. Note that when calculating some coefficients, the calculation of numerical integrals is necessary (Appendix A). The method of successive iterations is used to solve the system of equations since the unknowns (c_0 and ρ_0) are implicit. The following describes how the algorithm solution is implemented. First, the input parameters are defined as the density (ρ_2), compressional wave (V_{P2}) and shear wave (V_{S2}) velocities of the matrix; density (ρ_1), compressional wave (V_{P1}) and shear wave (V_{S1}) velocities, volume fraction (ϕ), radius (a), characteristic length (β) and aspect ratio (α) of inclusions; as well as dimensionless frequency (ϖ) and wave incidence angle (θ). Matrix' properties are then assigned, such as the initial values c_0 and ρ_0 in c_0=c_{n+1} and ρ_0=ρ_{n+1}. It is worth mentioning that matrix's properties are identified with the subscript n+1, and the number of inclusions is r=1,…n (Eqs. 1 and 2). The iterative process runs from the initial values until a values' succession is obtained and until the value of the solution converges to an assigned tolerance. To seek each of the effective elastic moduli, different tolerances (Tol_m) are assigned. When these tolerances are not satisfied, and if the maximum number of iterations (Max i) is exceeded, the flow chart does not converge.

The vector notation from applying Hill's notation is:

$$c=\left(2k,l,q,n,2m,2p\right),\rho=\left(\rho_{\mathrm{I}},\rho_{\mathrm{III}}\right) \tag{7}$$

To determine $\overline{T}_x^{(r)}$ and $\overline{Q}_t^{(r)}$, it is necessary to calculate the auxiliary functions M_r y N_r, which are described in Appendix A. When auxiliary functions are obtained, the integrals (Eqs. 10 to 16) are solved to determine the vectors:

$$\overline{T}_x^{(r)}=\left(2k_T,l_T,q_T,n_T,2m_T,2p_T\right),\overline{Q}_t^{(r)}=\left(Q_I,Q_{III}\right) \tag{8}$$

Applying the vectors $\overline{T}_x^{(r)}$ and $\overline{Q}_t^{(r)}$ in the self-consistent implementation in Eqs. 1 and 2, the solution helps to estimate the effective dynamic properties:

$$L_0=[k_0,\ l_0,\ q_0,n_0,m_0,p_0,\rho_{01},\rho_{03}]. \tag{9}$$

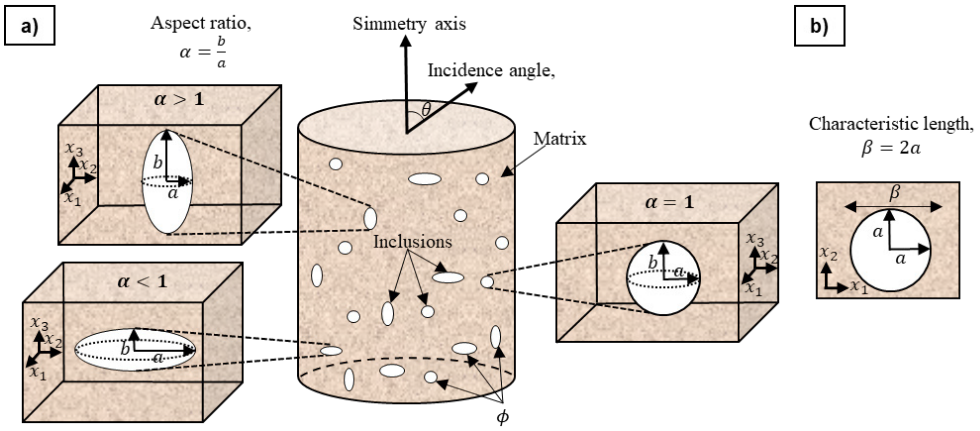

Figure 1. Schematic diagram showing the geometries and parameters used in the anisotropic model. a) Vertical and horizontal ellipsoidal and sphere inclusions considering volume fraction (ϕ), aspect ratio (α) that relates to radius (a) and semi-axis (b) embedded in the matrix. b) The inclusion in the plane (x_1, x_2) is a circle with a radius a and characteristic length (β).

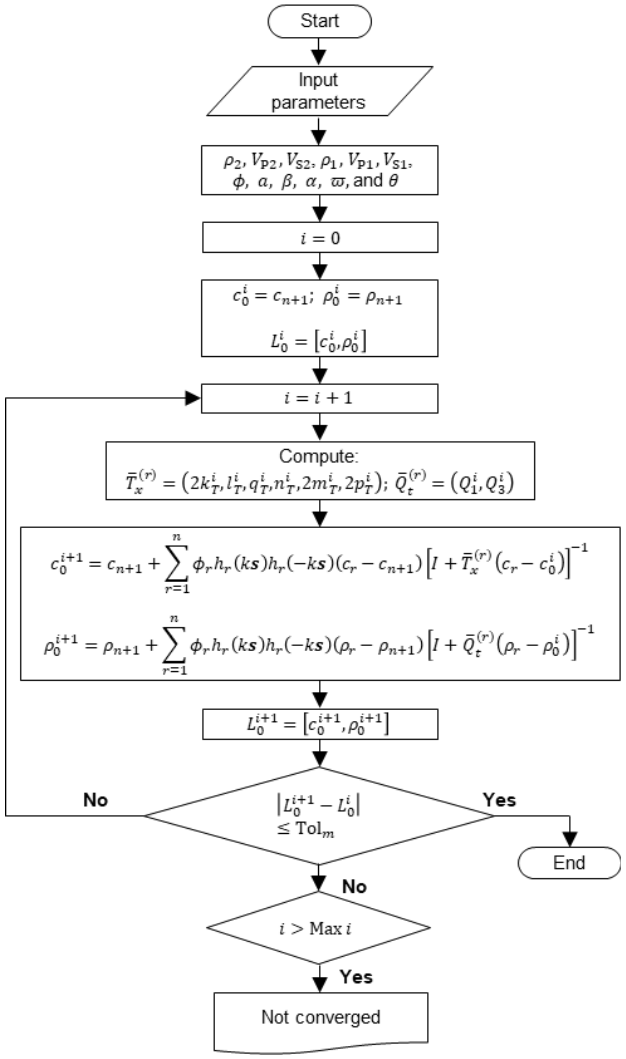

Figure 2. Flow chart of the self-consistent method solution to estimate effective dynamic properties.

3. Identification of pore-structure in images

Several pore classifications have been developed by Archie, Choquette and Pray, and Lucia (Lucia, 1983, 1995). The Archie classification (1952) emphasizes pore-structure with petrophysical properties, considering matrix porosity and visible pores. This classification is difficult to apply in geological models because it is not defined from depositional or diagenetic terms (Moore, 2001). The Choquette and Pray classification (1970) was designed as a descriptive and genetic system, identifying 15 types of pores which are divided into the selective fabric and non-selective fabric. They are associated with the pore boundary configuration and the pore's position relative to the fabric. The most abundant porosities are interparticle, intraparticle, intercrystalline, moldic, fenestral, fracture, and vuggy. This classification includes genetic modifiers, time of porosity formation, pore shapes (regular and irregular), and sizes. This classification has a wide diversity of pore network structures for each pore type that cannot be distinguished in the velocity-porosity relationship; for this is necessary to consider grain and pore shape, grain contact, cement occurrence, and particle packing (Fournier *et al.*, 2018). The Lucia classification integrates the rock fabric with the petrophysical properties since pore distribution controls permeability and saturation. Two classes of porosities are defined: interparticle, which indicates the pore space between grains or crystals (intergranular and intercrystalline); and vuggy porosity, that is subdivided according to how the vugs are interconnected; it can be separate vugs (moldic, intragranular, intraparticle, shelter) and touching vugs (fractures, cavernous, breccia, and fenestral) (Lucia, 1983, 1995).

Scanning Electron Microscope (SEM) and Photomicrographs images permit identifying a type of characteristic shape associated with different porosities. Three types of porosity are illustrated, where

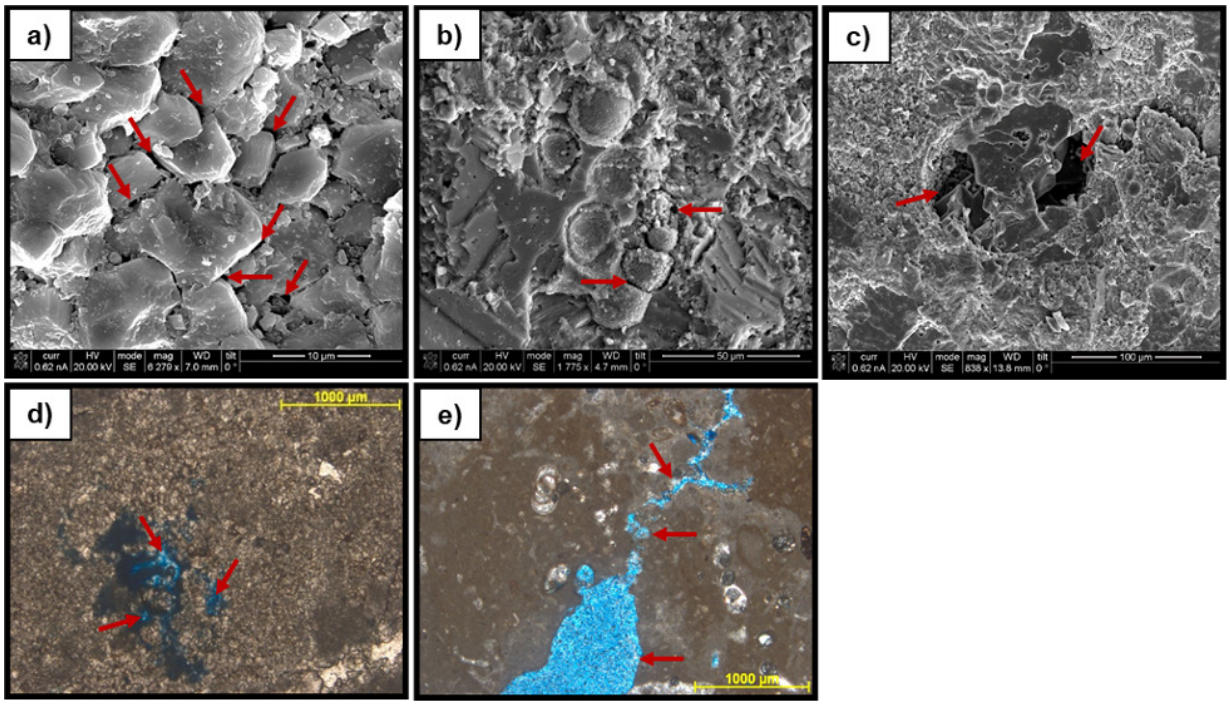

Figure 3. Carbonate rocks pores' shape analysis from SEM images with different porosities, **a)** intercrystalline, **b)** partially cemented moldic, **c)** moldic, and from Photomicrograph images with **d)** a connected vug and **e)** a vug with intense dissolution (arrows indicate pore shapes).

intercrystalline pore shapes are elongated, they become rounded and with a smaller size (Figure 3a). The moldic pores' shape will depend on the constituents that formed it, such as shells, grains, salts, or plant roots (Wang, 1997). In particular, the partially cemented moldic pores are rounded but of a smaller size than moldic pores (Figure 3b and c). The vug pores are sub-rounded to rounded and show elongated ellipsoidal shapes (Figure 3d and e).

In summary, it is essential to identify the pore shape of carbonates to analyze the velocity-porosity relationship since it is related to the aspect ratio (α) for characterizing the pore-structure from ultrasonic velocity data.

4. Case study: Application in carbonate samples

The published database of 117 limestone samples was taken from Fournier *et al.* (2014); P-wave and S-wave ultrasonic velocity values are measured at 1 MHz, and porosity data (0-15%) and dominant pore type were considered. The porosity is classified as intercrystalline, intergranular macropores, moldic macropores (open and cemented), and open vugs. Ultrasonic velocities at 40 MPa were chosen to conserve the elastic properties. The samples correspond to the Lower Cretaceous platform located in three zones, Rustrel, Nesque, and Fontaine-De-Vaucluse in Provence, southeastern France (Figure 4).

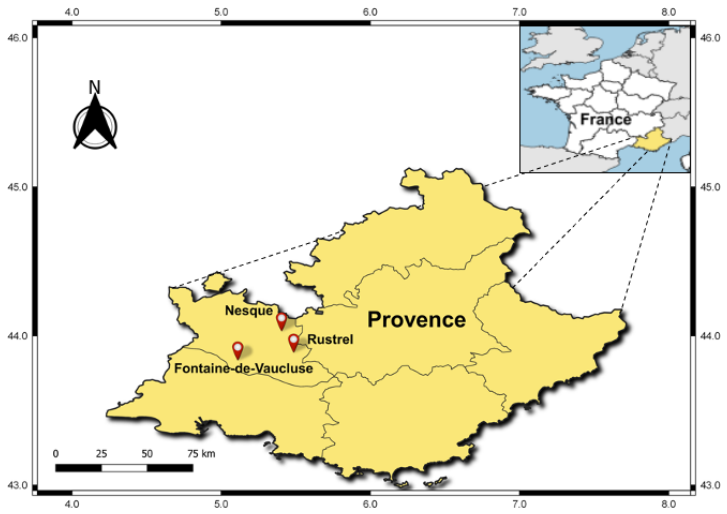

Figure 4. Location of carbonate sample data, Provence, southeastern France.

During the Lower Cretaceous, the lithology type in Provence corresponds to limestone, also known as Urgonian. It is a carbonate platform system isolated from terrigenous sediments of Valanginian to the Lower Aptian age. A carbonate belt was developed around the Vocontian basin in the western Alpine basin during this age (Masse, 1993). The Urgonian platform was marked by drowning events that interrupted three growth and progradation stages (Masse, 1993, Masse and Fenerci-Masse, 2011).

This case study has been used for the EMM modeling of velocities. A calcite matrix and air inclusion were chosen to simulate experimental data's real conditions, samples of dry carbonates. The input parameters (Figure 2) of the matrix are density, ρ_2=2710 kg/m^3, compressional wave velocity, V_{P2}=6400 m/s and shear wave velocity, V_{S2}=3250 m/s and for the inclusion are ρ_1=1204.1kg/m^3,

V_{P1}=343.2 m/s associated with sound propagation and V_{S1}=0 m/s (at 20 °C). The selected parameters are within the variation of values for calcite, i.e., P-wave velocity ranges between 6260 and 6640 m/s and S-wave velocity ranges approximately between 3240 and 3440 m/s (Mavko *et al.*, 2009).

5. Results and discussion

The results from estimating effective dynamic properties based on the Effective Medium Method (EMM) for the transversely isotropic medium are analyzed and discussed in four sections. First, characteristic length (β) is determined to identify pore sizes (Section 5.1). Section 5.2 presents the impact of the wave incidence angle (θ) on the velocities. The pore-structure prediction from the velocity-porosity relationship is analyzed in Section 5.3. Finally, a section of anisotropy includes Young's modulus (E_{33}) and Poisson's ratio (υ_{31}), as well as Thomsen's parameters (ε,γ and δ) for different aspect ratios (Section 5.4).

5.1 Determination of characteristic pore length

The effects of characteristic length (β) on estimated velocities at ultrasonic (1 MHz), sonic (10 kHz), and seismic (85 Hz) frequencies (f) are shown in Figure 5. This Figure shows smaller pore sizes affect velocities more than larger pores with increasing porosity at the frequencies analyzed.

The best characteristic length describing the pore size in the experimental data is β=0.001 m (Figure 5a and b) which will be used to predict pore-structure in Section 5.3. This parameter was determined from the minimum curve that encompasses the maximum amount of velocity measurements. The velocities change with frequency because of wavelength changes as well as pore sizes. It means that at a sonic frequency, the size of pores or inclusions (β) ranging from 0.09 to 0.33 m (Figure 5c and d) and from 10 to 36 m at the seismic frequency in P- wave and S-wave velocities (Figure 5e and f). The parameters of β=0.09 m and β=10 m were chosen to predict the pore-structure at these frequencies. It is important to note that there is not velocity data from the same area of study using sonic and seismic frequencies.

These results display that f is a parameter related to the prediction of pore size (Figure 5). Indeed, the characteristic length is defined for identifying the pore sizes, which depend on the investigation scales (ultrasonic, sonic, and seismic) to predict the pore geometry since pore sizes influence the velocities.

5.2 Influence of wave incidence angle on anisotropic velocities

One of the fundamental parameters for predicting the pore-structure, considering anisotropy in carbonate rocks, is the wave incidence angle (θ); this represents the angle at which an electrical pulse is induced on the laboratory samples to measure ultrasonic velocities. Generally, these measurements are taken at 0° of incidence angle. Despite the difficulty represented by ultrasonic velocity measurements taken at a different angle, in this paper θ is included as an input parameter on the micromechanical model (Figure 2) to estimate compressional wave velocity (V_P), horizontally (V_{SH}) and vertically (V_{SV}) polarized shear wave velocities at different angles. The propagation direction of V_P(0°) is on the axis x_3, and the polarization direction for V_{SH}(0°) is on the axis x_2 and V_{SV}(0°) on the axis x_1.

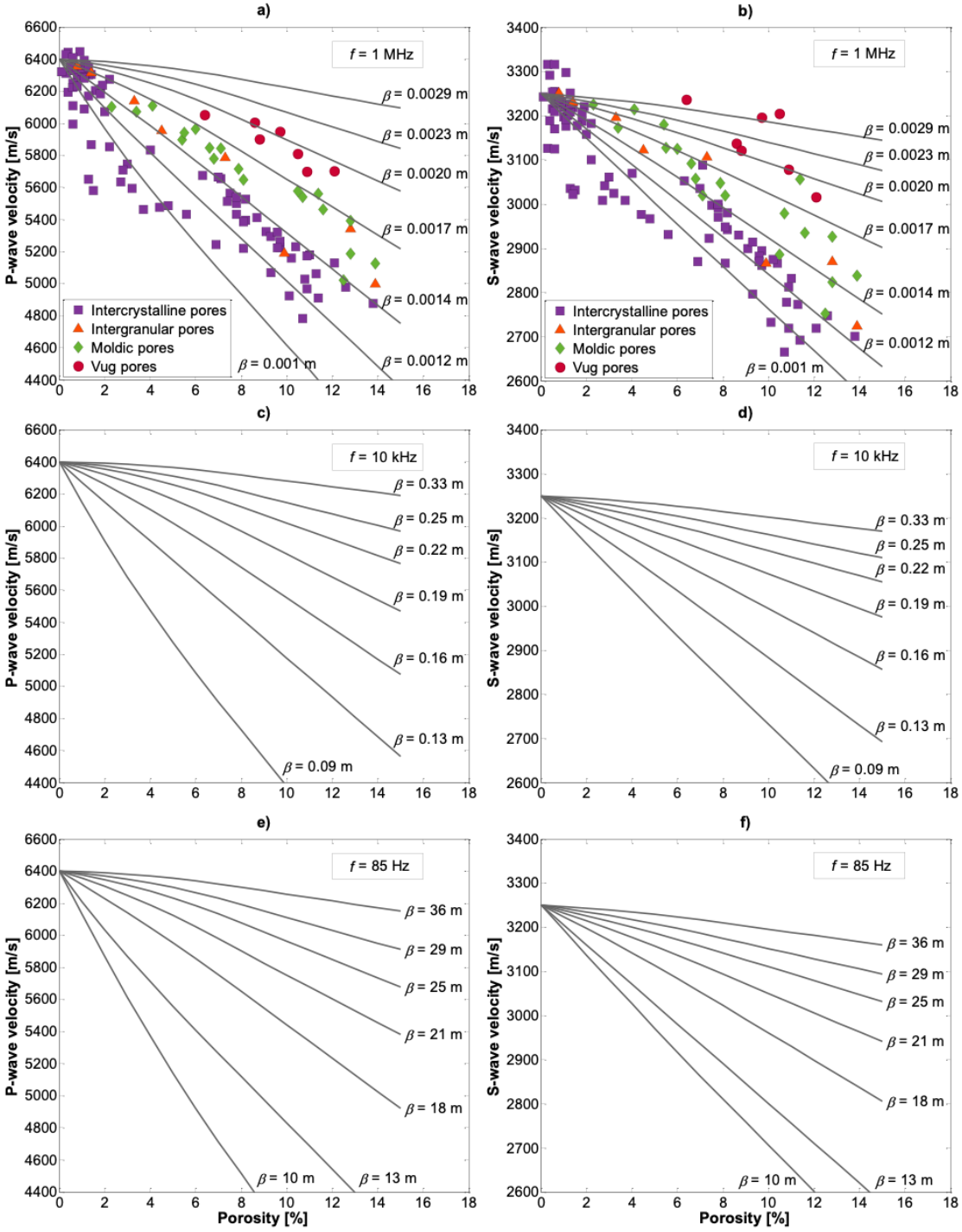

Figure 5. Effect of characteristic length (β) on modeled velocities taking into account θ=0° and α=0.15 plotted against porosity at different frequencies. **a)** P-wave and **b)** S-wave modeled velocities with different β on experimental data of P-wave and S- wave velocities, porosity, and pore type reported by Fournier *et al.* (2014) at ultrasonic frequency; **c)** compressional wave and **d)** shear wave velocities estimated with β values ranging from 0.09 to 0.33 m at sonic frequency; **e)** compressional waves and **f)** shear waves velocities estimated using effective dynamic properties with different values of β at seismic frequency.

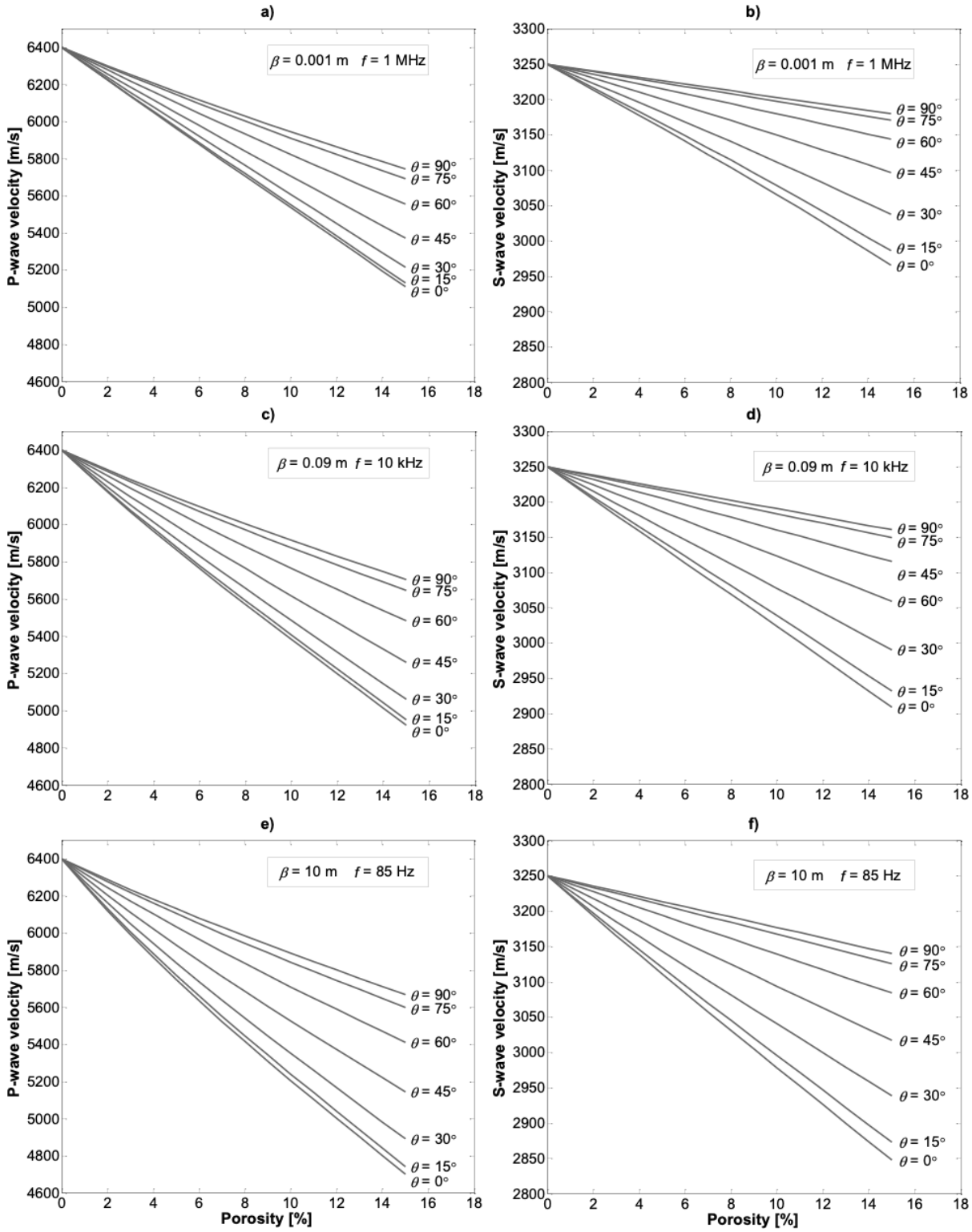

Figure 6. Anisotropy of P-wave and S-wave velocities estimated considering the wave incidence angle ranges from 0° to 90° with α=0.4 as a function of porosity; **a)** compressional wave and **b)** shear wave velocities at the ultrasonic frequency with a pore size of β=0.001 m; **c)** P-wave and **d)** S-wave velocities estimated at the sonic frequency with a pore size of β=0.09 m; **e)** P-wave and **f)** S-wave velocities at the seismic frequency with β=10 m.

The impact of varying θ between 0° to 90° on P-wave and S-wave velocities are shown in Figure 6a and b, respectively. The velocity variations from one angle (0°) to another (90°) are smaller at lower porosities (<4%); for example, when porosity is ϕ=4%, the compressional velocities are V_P (0°)=6057 m/s and V_P (90°)=6207 m/s; and shear wave velocities are V_{SH}(0°)=3178 m/s and V_{SH} (90°)=3231 m/s. But, if the porosity increases, the velocity variation become significantly higher than at low porosities, since V_P (0°)=5196 m/s and V_P (90°)=5785 m/s; V_{SV}(0°)=V_{SH}(0°)=2986 m/s and V_{SH} (90°)=3185 m/s at ϕ=14%. This analysis also displays that the angle impacts more V_P than V_S at the ultrasonic frequency. Vertical and horizontal shear wave velocities are the same at θ=0° in transversely isotropic medium (Mavko *et al.*, 2009).

The effect of θ in velocities at seismic frequency is higher than in sonic and ultrasonic frequencies as porosity increases (Figure 6), i.e., at 85 Hz, V_P varies 912 m/s and V_{SH} varies 273 m/s while at

10 kHz, V_P varies 732 m/s and V_{SH} varies 235 m/s between 0° and 90° at ϕ=14%. It was identified that θ influences the velocities when the porosity increases, and the effect is more significant as the frequency decreases. The incidence angle aims to upgrade the rock samples' anisotropic analysis because the micromechanical model can estimate anisotropic elastic moduli. It could also identify the preferential pore direction in rocks depending on the different pore shapes, but this needs to be validated.

5.3 Characterization and prediction of pore-structure

The Micromechanical model was applied to estimate effective dynamic properties considering the characteristic length (β), frequency (f), wave incidence angle (θ), aspect ratio (α), mineralogy, porosity (ϕ) and type of fluid to predict pore-structure in carbonates (Figure 7). The present work considers a long-wavelength (static) analysis according to Kinra and Anand (1982), which means that the wavelength is greater than the radius of the inclusion.

The estimations of V_P and V_S consider parameters such as f =1 MHz and θ=0° to have the same conditions in which ultrasonic velocities were measured in the laboratory. Figure 7a shows that the pore-structure was identified from velocity modeling with different aspect ratio on experimental data of V_P, where intercrystalline pores are elastically similar to flat ellipsoidal shape characterized by low α values (<0.35), while intergranular pores show aspect ratios ranging from 0.25 to 0.5. The intergranular and intercrystalline pores also reach α values up to 1 and 2 at low porosities (<2%), respectively. The pore geometries associated with moldic pores ($0.3 < \alpha < 0.5$) are very similar to intergranular pores with an ellipsoidal shape. Finally, vug pores show a variation of $0.6 < \alpha < 1$ that geologically represents pores with a geometrical tendency to be under-rounded and spherical.

In contrast to V_P, the prediction of pore-structure with V_S is slightly different due to the deformation experienced by pores' motion when the elastic waves propagate through the rock. The results of pore-structure characterization from modeled shear wave indicates that intercrystalline pores have aspect ratio values similar to the predictions obtained with V_P; intergranular pores show α values between 0.2 and 2. Moldic and vug pores exhibit α values ranging from 0.2 to 0.7 and 0.4 to 1.5, respectively (Figure 7b).

The velocity modeling results with characteristic length β=0.001 m at ultrasonic frequency show that higher porosities present greater error in estimating velocities if pore-structure is not considered (Figure 7a and b). According to aspect ratio values between 0.15 and 2, the variations of

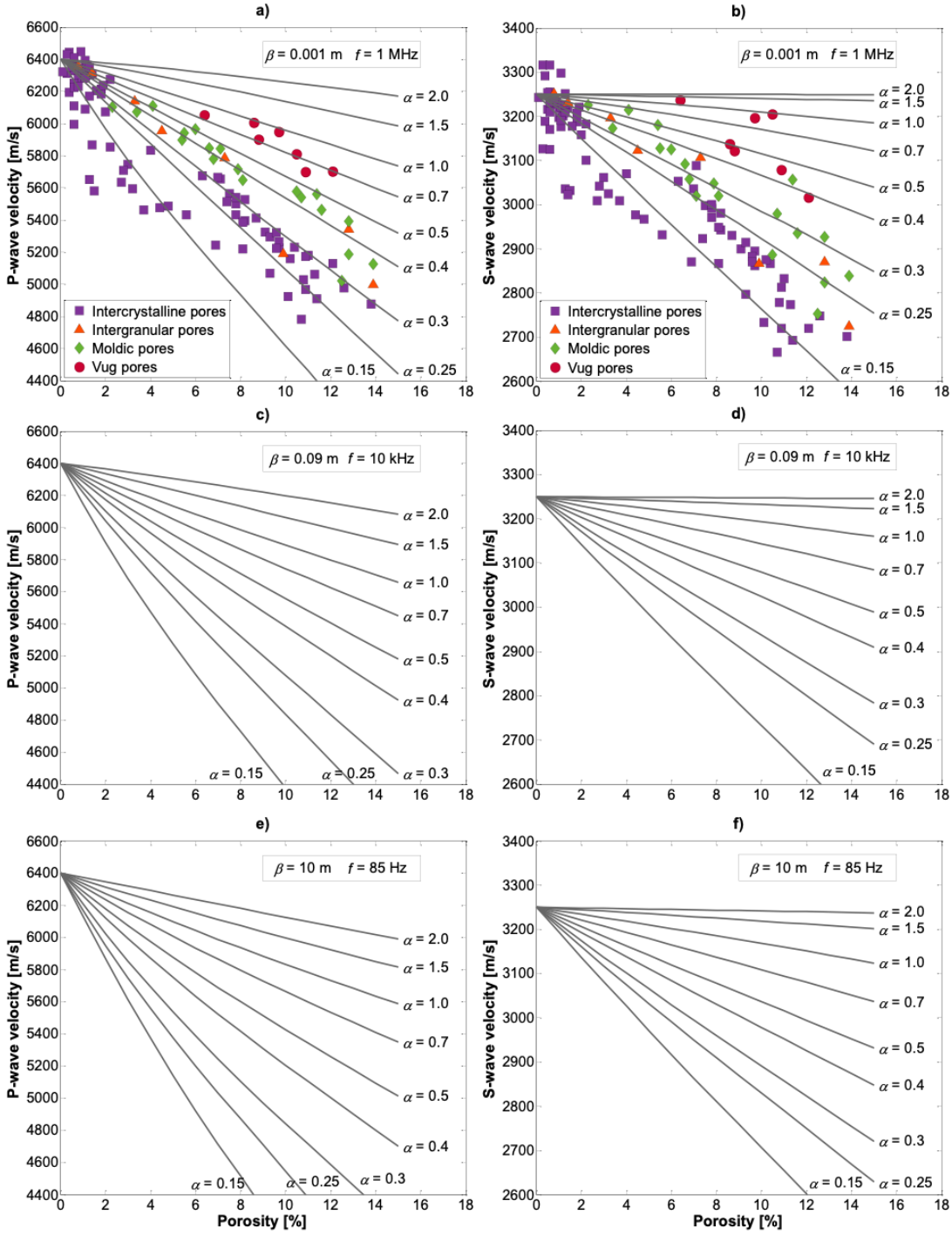

Figure 7. Characterization of the pore-structure considering different aspect ratios and θ=0° with the micromechanical model. **a)** Compressional wave and **b)** shear wave modeled as a function of porosity validated with experimental data of P-wave and S- wave velocities, porosity, and pore type taken from Fournier *et al.* (2014) at the ultrasonic frequency. **c)** P- wave and **d)** S- wave velocities plotted against porosity at the sonic frequency and **e)** P- wave and **f)** S- wave velocities versus porosity with a pore size of 10 m at seismic frequency. The velocity modeling predictions represent a velocity recognition pattern of dry samples at sonic and seismic frequencies.

compressional velocities are 759 m/s, 1640 m/s, and more than 2000 m/s to 4%, 10%, and 15% porosities, respectively. For the shear wave velocities, the velocity discrepancies at the same porosities are 198 m/s, 485 m/s, and 720 m/s. The relative error of velocities at the porosities above mentioned are approximately 10%, 25%, and 35% in V_P and 5%, 15%, and 20% in V_S. In general, the relative error increases slightly as the frequency decreases (Figure 7).

According to Wang (1997), flat pores are easier to deform when waves propagate, in contrast to rounded pores, which are difficult to deform. It is important to point out that there are pore shapes that are more susceptible to a quick decline of velocity curves with porosity changes, i.e., pores with $\alpha > 0.7$ do not show a pronounced decrease in the velocity-porosity relationship, pores with α=1 are considered isotropic and pores with low aspect ratios ($0.15 < \alpha < 0.5$) whose velocity curves begin to decline at low porosities. The pore-structure at different pore sizes impacts velocity modeling almost the same way for the three ranges of frequency (Figure 7).

The results of pore-structure prediction in carbonate samples at ultrasonic frequency are different from those obtained by Fournier *et al.* (2014) and Fournier *et al.* (2018) that considers a pore type classification which can belong to reference, stiff and soft pores (Xu and Payne, 2008) with DEM. This method assumes an isotropic, linear, and elastic media with random inclusions inside a host, and the effective properties describe an isotropic medium. Only P- and S- wave velocities are predicted to high frequency with DEM (Appendix C). However, this method does not indicate a specific frequency, which is necessary to produce the ultrasonic pulse to obtain velocity measurements in the laboratory. In this research, the transversely isotropic media is considered, which means anisotropic media where the randomly aligned inclusions are embedded in the matrix (Figure 1a). Either vertical or horizontal, P- and S- wave velocities are computed with EMM at different angles and frequencies.

5.4 Prediction of anisotropy in carbonate rocks

The static moduli are obtained by measuring rock deformation in response to pressure applied; in contrast, dynamic moduli are calculated from acoustic velocities (Wang *et al.*, 2016) through deformation of the rock experienced as the waves travel through a medium. The response of an isotropic medium is independent of the orientation of stress, the main axes of stress and strain coincide (Fjaer *et al.*, 2008), but in an anisotropic medium, these vary axially and transversally.

In this section, Young's modulus (E_{33}) and Poisson's ratio (υ_{31}) were calculated for a transversely isotropic medium from elastic constants of stiffness matrix (Appendix B). These are a function of V_P (0°), V_P (45°), V_P (90°), V_{SH} (0°) and V_{SH} (90°) which were estimated considering three parameters: the frequency (f), characteristic length (β) and aspect ratio (α).

The predictions of E_{33} were compared with dynamic Young's moduli from ultrasonic velocity data (Figure 8a). There are two main classes of intercrystalline pores: the first type has variation in dynamic Young's moduli of 70 to 78 GPa with aspect ratio values ranging from 0.15 to 2 at low porosities(<2%); the second class presents a more significant dynamic Young's moduli variation of around 49 to 70 GPa with α values from 0.15 to 0.7, which indicates that the pores of rock samples are more deformable than the first class. Intergranular and moldic pores shown high variation in dynamic Young's moduli between 52 and 76 GPa, with $0.35 < \alpha < 2$. Finally, the vug pores present a pore-structure of 1 to greater than 2 of the aspect ratio. This analysis of E_{33} versus porosity helps to understand the elastic behavior of pores.

In Figure 8b, the pore-structure predictions with υ_{31} were compared with dynamic Poisson's ratio. There are also two types of pores with dynamic Poisson's ratio values ranging approximately between 0.27 to 0.31 and 0.31 to 0.34. However, there was no trend of pore geometry for the different porosity types, probably due to the lateral strain induced in the x_1 plane by uniaxial stress in the x_3 plane. Another factor could be that the values of dynamic Poisson's ratio are not anisotropic, for this is necessary to measure the ultrasonic velocities as V_P (45°), V_P (90°) and V_{SH} (90°) in the laboratory.

The E_{33} and υ_{31} curves calculated at sonic frequency are shown in Figure 8c and d, respectively. The variation of E_{33} in the range of pore shapes ($0.15 < \alpha < 2$) do not vary much (57-73 GPa) at 4% porosity, but for a high porosity (8%), E_{33} tends to vary in a more considerable proportion (45-70 GPa). The behavior of E_{33} is similar to dynamic Poisson's ratio because these curves ($0.27 < \upsilon_{31} < 0.322$) are not affected at 4% porosity, but when porosity increases (>8%), the discrepancy from the υ_{31} curves for the same aspect ratio range is greater than 0.08.

The pore-structure that most affect Young's modulus and Poisson's ratio are those which have aspect ratios (α) ranging from 0.15 to 0.5, showing an abrupt decline of the elastic moduli curves with increasing porosity, while pores with $\alpha > 0.7$ are less anisotropic at the frequencies analyzed. Indeed, the impact of pore shapes is critical in anisotropic elastic moduli. If pore-structure is considered, the anisotropic Young's modulus and Poisson's ratio will reduce the relative error in the interpretation of about 35% and 25%, respectively, at different frequencies for ϕ=15% (Figure 8).

Thomsen parameters ε, γ, and δ (Appendix B) were calculated to quantify anisotropy caused by the pore-structure at the ultrasonic frequency. The parameter ε refers to P-wave anisotropy, γ measures S-wave anisotropy, and δ is related to anellipticity of P-wave Meléndez-Martínez and Schmitt, (2013). The results show that the degree of P-anisotropy is greater ($0.3 < \varepsilon$) for pore shapes with $0.15 < \alpha < 0.25$ in porosity ranges between 9% and 15% than in pores with aspect ratios ranging from $0.3 < \alpha < 0.7$, whose ε curves are defined by values of $0 < \varepsilon < 0.22$. As mentioned before, pore types with α=1 lead an isotropic medium; for this reason, the calculated ε curve stays on the zero-line in the porosities analyzed here. When $\alpha > 1$, the range of anisotropy is from $-0.04 < \varepsilon < 0$. The curves with negative ε values indicate that the pore shapes change, i.e., horizontal ellipsoidal pore shape changes to vertical ellipsoidal shape (Figure 9a).

The parameter γ was compared with an apparent γ estimated with two polarized shear wave velocities orthogonal along the core axis. This data was taken from Fournier *et al.* (2014) of the same study area. Based on this analysis, it is observed that the pore-structure predictions in the estimations of V_S (Figure 7b) do not coincide with the anisotropic parameter γ for different pore shapes (Figure 9b). γ remains constant for aspect ratio values between 0.7 and 2 in the pore types, except in moldic and intergranular pores whose α values also vary from 0.4 to 0.5 and 0.25, respectively. The S-wave anisotropy show values from $-0.012 < \gamma < 0.083$, which are within the γ values in carbonates samples by (Meléndez-Martínez and Schmitt, 2013). To obtain a more appropriate γ it would be necessary to measure V_{SH} (90°) in the laboratory.

The analysis of δ parameter with $0.15 < \alpha < 0.25$ shows a convex tendency at high porosity values (>6%) (Figure 9c). The interval of aspect ratio ranging from $0.3 < \alpha < 0.7$ is similar to ε results but with a lower degree of anisotropy, $0 < \delta < 0.07$ in the porosity range from 0 to 15%.

To summarize, the degree of anisotropy also depends on porosity and pore-structure. ε and δ are not as significant at porosities between 0 and 2% and the same for γ from 0 to 4%. When the porosity increases, the pores with α values between 0.15 to 0.5 show greater anisotropy (Figure 9).

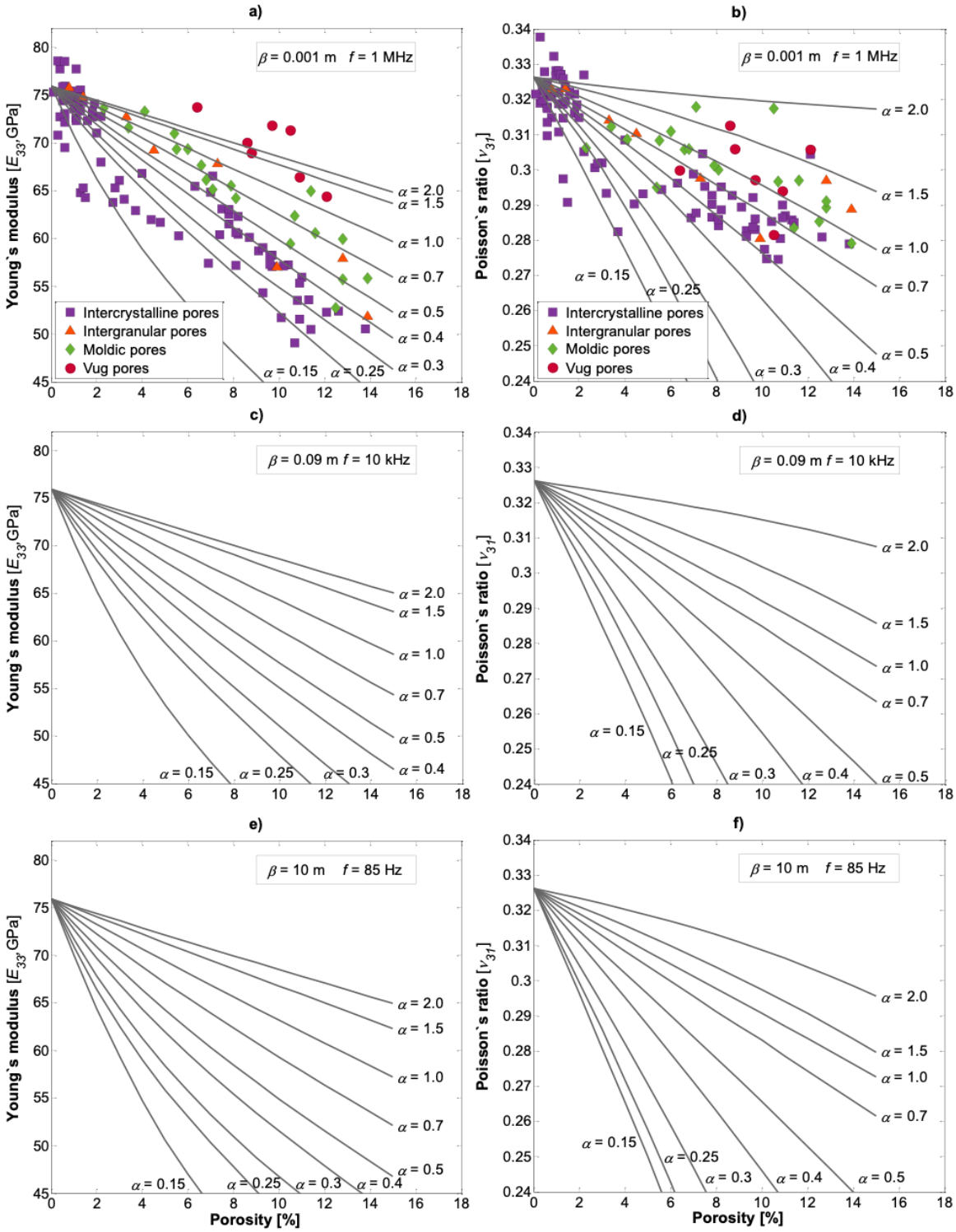

Figure 8. Anisotropic elastic moduli calculated to carbonates samples plotted against porosity considering different aspect ratios and frequencies. **a)** Young's modulus E_{33} and **b)** Poisson's ratio υ_{31} compared with dynamic moduli of carbonate samples calculated from V_p and V_S taken from Fournier *et al.* (2014). **c)** Young's modulus E_{33} and **d)** Poisson's ratio υ_{31} predicted at sonic frequency. **e)** Displaying E_{33} of 45-75 GPa considering aspect ratio variation and **f)** υ_{31} decreases with increasing porosity at seismic frequency.

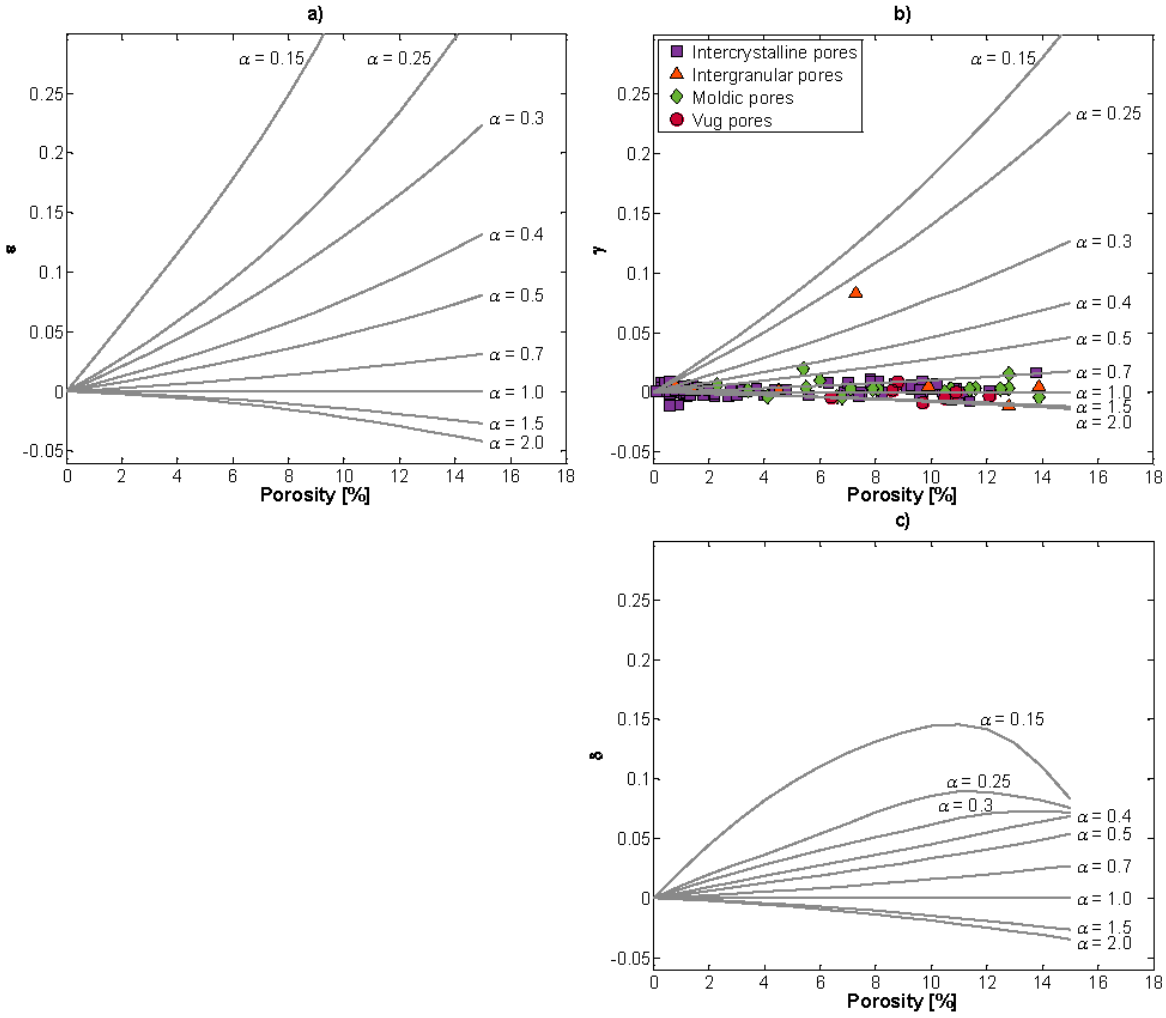

Figure 9. Thomsen parameter calculated as a function of porosity and aspect ratio at the ultrasonic frequency (1 MHz). a) Epsilon, b) γ curves are compared with an apparent γ estimated from two polarized shear wave velocities with an angle of incidence at 0° reported by Fournier et al. (2014) and c) Delta.

6. Conclusions

A micromechanical model based on the Effective Medium Method (EMM), which considers anisotropy, is used to improve the pore-structure characterization of carbonate rocks. This model predicts innovative effective dynamic properties for a transversely isotropic medium based on the rock microstructure. From these properties, velocities (V_P, V_{SH} and V_{SH}) are estimated considering the mineralogy, porosity, type of fluid filling the pore space, aspect ratio, characteristic length, wave incidence angle, and frequency.

The application of the EMM in carbonates describes a new element for a better understanding of how parameters such as characteristic length, aspect ratio, and frequency can modify the values of V_P and V_S for more than 35% and 20%, respectively. These percentages are according to the V_P and

V_S measurements of carbonate samples. Another improvement of this work is the analysis of wave incidence angle on elastic responses, since measuring velocities at different frequencies from different directions, 0° to 90°, is currently a research challenge.

The pore-structure results with DEM are different from those obtained with EMM since this model considers an anisotropic medium together with the parameters mentioned above, enhancing the predictions of P- and S- wave velocities considering more realistic properties of the rocks.

Pore-structure in carbonate samples is characterized by aspect ratio (α). The analysis of V_p modeling with velocity and porosity measurements, and pore type identifies that α values between 0.15 to 0.35 discriminate the intercrystalline pores, while intergranular pores are characterized by α from 0.25 to 0.5. Moldic pores present pore shapes similar to intergranular pores ($0.3 < \alpha < 0.5$) except at low porosities, and, finally, the vug pores are larger than the previous ones with α range between 0.6 and 1. There is significant variability of velocity-porosity relationship with different α, and it is more relevant for pore shape with $\alpha < 0.5$ than pore shape with $\alpha > 0.7$. It is related to velocity delay from 4% of porosity.

The shape of the pores also affects the estimation of dynamic anisotropic Young's modulus (E_{33}) and Poisson's ratio (υ_{31}). An increase in porosity causes an abrupt decrease in elastic moduli of rocks with aspect ratio values between 0.15 and 0.5. Based on the dynamic elastic moduli obtained from the model, the Thomsen parameters (ε, γ, and δ) were computed to quantify anisotropy. It was found that for pore shapes ranging from 0.15 to 0.5, there is the most considerable variation of anisotropy.

The characteristic length is associated with pore sizes. The wavelength is different at ultrasonic, sonic, and seismic frequencies. Therefore, geoscientists can establish a recognition pattern for velocities related to pore-structure or geologic structures, depending on the analysis level.

The results provide additional elements based on micromechanical models to improve characterization and better understand carbonate reservoirs to identify major oil interest zones. The pore-structure prediction could be analyzed in saturated samples with water or oil and include more inclusions as mineralogical composition.

Acknowledgments

The author Joseline Mena-Negrete would like to express her gratitude for the scholarship granted by CONACYT (Consejo Nacional de Ciencia y Tecnología) and the support provided by the Postgraduate Program of Instituto Mexicano del Petróleo. The authors state their appreciation to Instituto Mexicano del Petróleo for permitting to publish this article. This work was sponsored by Fondo Sectorial SENER-CONACYT-Hidrocarburos, with project number 280097 (Y.61067).

References

Akbar M., Petricola M., Watfa M., Badri M., Charara M., Boyd A., Cassell B., Nurmi R., Delhomme J.-P., Grace M., Kenyon B., Roestenburg J., 1995, Classic interpretation problems: evaluating carbonates. *Oilfield Review*, 7, 38-57.

Anselmetti F. S., Eberli G.P., 1993, Controls on sonic velocity in carbonates. *Pure and Applied Geophysics*, 141, 287-323.

Anselmetti F.S., Eberli G.P., 1997, Sonic velocity in carbonate sediments and rock. In: Palaz, I., Marfurt, K. J. (eds.) Carbonate Seismology. Society of Exploration Geophysicists, Tulsa, 443 pp.

Archie G.E., 1952, *Classification of carbonate reservoir rocks and petrophysical considerations. American Association of Petroleum Geologists Bull.*, 36, 278-298.

Assefa S., McCann C., Sothcott J., 2003, Velocities of compressional and shear waves in limestones. *Geophysical Prospecting*, 51, 1-13.

Berryman J.G., 1980, Long-wavelength propagation in composite elastic media II. Ellipsoidal inclusions. *J. Acoust. Soc. Am.*, 68, 1820-1831.

Berryman J. G., 1992., Single-scattering approximations for coefficients in Biot's equations of poroelasticity. *J. Acoust. Soc. Am.*, 91, 551–571.

Berryman J. G., 1995, Mixture Theories for rock properties. In: Ahrens, T.J. (eds.) Rock Physics and Phase Relations: a Handbook of Physical Constants. American Geophysical Union, Washington, 237 pp.

Berryman J.G., Berge P.A., 1996, Critique of two explicit schemes for estimating elastic properties of multiphase composites. *Mechanics of Materials*, 22, 149-164.

Brigaud B., Vincent B., Durlet C., Deconinck J.-F., Blanc P., Trouiller A., 2010, Acoustic properties of ancient shallow-marine carbonates: effects of depositional environments and diagenetic processes (Middle Jurassic, Paris Basin, France). *Journal Sedimentary Research*, 80, 791-807.

Budiansky B., 1965, On the elastic moduli of some heterogeneous materials. *J. Mech. Phys. Solids*, 13, 223-227.

Choquette P.W., Pray LL.C., 1970, Geologic nomenclature and classification of porosity in sedentary carbonates. *American Association of Petroleum Geologists Bull.*, 54, 207-250.

Cleary, M.P., Lee S.-M., Chen I.-W., 1980, Self-consistent techniques for heterogeneous media. *ASCE. J. Eng. Mech.*, 106, 861-887.

De Assis P.C., Moraes F., Tabelini Junior R.J., Freitas U.O., 2017, On the influence of texture on ultrasonic velocities of carbonate rocks using a global petrophysical database in Society of Exploration Geophysicists International Exposition and 87th Annual Meeting, Houston, Texas, 24-September-27 September.

Eberli G.P., Baechle G.T., Anselmetti F.S., Incze M.L., 2003, Factors controlling elastic properties in carbonate sediments and rocks. *The Leading Edge*, 654-660.

Eshelby J.D., 1957, The determination of the elastic field of an ellipsoidal inclusion, and related problems. *Proceedings of the Royal Society of London. Series A. Mathematical and Physical Science*, 241, 376-396.

Fjaer E., Holt R.M., Horsrud P., Raaen A.M., Risnes R., 2008, Petroleum Related Rock Mechanics. Elsevier, Amsterdam, 491 pp.

Fournier F., Leonide P., Biscarrat K., Gallois A., Borgomano J., Foubert A., 2011, Elastic properties of microporous cemented grainstones. *Geophysics*, 76, E211-E226.

Fournier F., Leonide P., Kleipool L., Toullec R., Reijmer J.J.G., Borgomano J., Klootwijk T., Van Der Molen J., 2014, Pore space evolution and elastic properties of platform carbonates (Urgonian limestone, Barremian-Aptian, SE France). *Sedimentary Geology*, 1-43.

Fournier F., Pellerin M., Villeneuve Q., Teillet T., Hong F., Poli E., Borgomano J., Léonide P., Hairabian, A., 2018, The equivalent pore aspect ratio as a tool for pore type prediction in carbonate reservoirs. *American Association of Petroleum Geologists Bull.*, 102, 1343-1377.

Gupta A., Gairola G.S., 2020, Integrated reservoir characterization using petrophysical and petrographical analysis. In: Singh, K. H., Joshi, R. M. (Eds) Petro-physics and rock physics of carbonate reservoirs. Springer Nature, Singapore, 299 pp.

Hairabian A., Fournier F., Borgomano J., Nardon S., 2014, Depositional facies, pore type and elastic properties of deep-water gravity flow carbonates. *Journal of Petroleum Geology*, 37(3), 231-250.

Hill R., 1965, A Self-consistent mechanics of composite materials. *J. Mech. Phys. Solids*, 13, 213-222.

Hudson J.A., 1980, Overall properties of a cracked solid. *Math. Proc. Camb. Phil. Soc.*, 88, 371-384.

Hudson J.A., 1981, Wave speeds and attenuation of elastic waves in material containing cracks. *Geophys. J. R. astr. Soc.*, 64, 133-150.

Kinra V.K., Anand A., 1982, Wave propagation in a random particulate composite at long and short wavelengths. *Int. J. Solids Structures*, 18, 367-380.

Kuster G.T., Toksöz M.N., 1974, Velocity and attenuation of seismic waves in two-phase media: part I, Theoretical formulations. *Geophysics*, 39, 587-606.

Li T., Wang R., Wang Z., Wang Y., 2016, Experimental study on the effects of fractures on elastic wave propagation in synthetic layered rocks. *Geophysics*, 81, D441-D451.

Lima N.I.A., Misságia R.M., Ceia M.A., Archilha N.L., Oliveira L.C., 2014, Carbonate pore system evaluation using the velocity-porosity-pressure relationship, digital image analysis, and differential effective medium theory. *J. of Applied Geophysics*, 110, 23-33.

Lucia F.J., 1983, Petrophysical parameter estimated from visual description of carbonate rocks: a field classification of carbonate pore space. *J. of Petroleum Technology*, 629-637.

Lucia F.J., 1995, Rock-fabric/petrophysical classification of carbonate pore space for reservoir characterization. *American Association of Petroleum Geologists Bull.*, 79, 1275-1300.

Masse J.-P., 1993, Valanginian-early Aptian carbonate platforms from Provence, Southeastern France. In: Simo, J. A. T., Scott, R. W., Masse, J.-P. (eds.) Cretaceous carbonate platforms. American Association of Petroleum Geologist Memoir, 56, 363-374.

Masse J.-P., Fenerci-Masse M., 2011, Drowning discontinuities and stratigraphic correlation in platform carbonates. The late Barremian-early Aptian record of southeast France. *Cretaceous Research*, 32, 659-684.

Mavko G., Mukerji T., Dvorkin J., 2009, The rock physics handbook. Tools for seismic analysis of porous media. Cambridge University Press, Cambridge, 511 pp.

McLaughlin R., 1977, A study of the differential scheme for composite materials. *Int. J. Engng Sci.*, 15, 237-244.

Meléndez-Martínez J., Schmitt D. J., 2013, Anisotropic elastic moduli of carbonates and evaporites from Weyburn-Midale reservoir and seal rocks. Geophysical Prospecting, 61, 363-379.

Miller S.L.M., 1992, Well log analysis of Vp and Vs in carbonates. *CREWES Research Report*, 4, 1-11.

Moore C.H., 2001, Carbonate reservoir. Porosity evolution and diagenesis in a sequence stratigraphic framework. Developments in Sedimentology 55, Amsterdam, 444 pp.

Norris A.N., 1985, A differential scheme for the effective moduli of composites. *Mechanics of Materials*, 4, 1-16.

O'Connell R.J., Budiansky B., 1974, Seismic velocities in dry and saturated cracked solids. *J. of Geophysical Research*, 79, 5412-5426.

Panizza G., Ravazzoli C., 2019, An efficient rock-physics workflow for modeling and inversion in anisotropic organic shales. *J. of Petroleum Science and Engineering*, 180, 1101-1111.

Pyrak-Nolte L.J., Shao S., Abell B.C., 2017, Elastic waves in fractured isotropic and anisotropic media. In: Xia-Ting, F. (eds.) Rock Mechanics and Engineering Volume I: Principles. Taylor & Francis Group, London, 770 pp.

Sabina F.J., Willis J.R., 1988, A simple self-consistent analysis of wave propagation in particulate composites. *Wave Motion*, 10, 127-142.

Sabina F.J., Smyshlyaev V.P., Willis J.R., 1993, Self-consistent analysis of waves in a matrix-inclusion composite-I. Aligned spheroidal inclusions. *J. Mech. Phys. Solids*. 41, 1573-1588.

Sabina F.J., Gandarilla-Pérez C.A., Otero J.A., Rodríguez-Ramos R., Bravo-Castillero J., Guinovart-Díaz R., Valdiviezo-Mijangos O., 2015, Dynamic homogenization for composites with embedded multioriented elipsoidal inclusions. International *J. of Solids and Structures*, 69-70, 121-130.

Shuai D., Wei J., Di B., Guo J., Li D., Gong F., Stovas A., 2020, Experimental study of crack density influence on the accuracy of the effective medium theory. *Geophysical J. International*, 220, 352-369.

Thomsen L., 1986, Weak elastic anisotropy. *Geophysics*, 51, 1954-1966.

Valdiviezo-Mijangos O.C., Nicolás-López R., 2014, Dynamic characterization of shale systems by dispersion and attenuation of P- and S-waves considering their mineral composition and rock maturity. *J. of Petroleum Science and Engineering*, 122, 420-27.

Valdiviezo-Mijangos, O. C., J. Meléndez-Martínez, R. Nicolás-López, 2020, Self-consistent and squirt flow modelling of velocity dispersion and attenuation for effective stress dependent experimental data. *Exploration Geophysics*, 51, (2) 248-255.

Wang F., Bian H., Yu J., Zhang Y., 2016, Correlation of dynamic and static elastic parameters of rock. *Electronic J. of Geotechnical Engineering*, 21, 1551-1560.

Wang Z., 1997, Seismic properties of carbonate rocks. In: Palaz, I., Marfurt, K. J. (eds.) Carbonate Seismology, Society of Exploration Geophysicists, Tulsa (2008), 443 pp.

Wardaya P.D., Noh K.A.B.M., Yusoff W.I.B.W., Ridha S., Nurhandoko B.E.B., 2014, The thin section rock physics: modeling and measurement of seismic wave velocity on the slice of carbonates. AIP Conference Proceedings, 1617, 152-155.

Weger R.J., Eberli G.P., Baechle G.T., Massaferro J.L., Sun Y., 2009, Quantification of pore structure and its effect on sonic velocity and permeability in carbonates. *American Association of Petroleum Geologists Bull.*, 93, 1297-1317.

Xu, S., Payne, M. A., 2009, Modeling elastic properties in carbonate rocks. *The Leading Edge*, 28, 66-74.

Zimmerman R.W., 1991, Elastic moduli of a solid containing spherical inclusions. *Mechanics of Materials*, 12, 17-24.

Appendix A: Auxiliary equations to estimate effective properties

In Eq. 8, the vectors $\overline{T}_x^{(r)}$ and $\overline{Q}_t^{(r)}$ are obtained from solving the integrals by Sabina *et al.* (1993):

$$q_T = l_T = \frac{1}{2\sqrt{\rho_I \rho_{III}}} \int_0^1 u\sqrt{1-u^2}\, m_1 m_3 \left[M_1 - M_3\right] du, \tag{10}$$

$$q_T = l_T = \frac{1}{2\sqrt{\rho_I \rho_{III}}} \int_0^1 u\sqrt{1-u^2}\, m_1 m_3 \left[M_1 - M_3\right] du, \tag{11}$$

$$n_T = \frac{1}{\rho_{III}} \int_0^1 u^2 \left[m_3^2 M_1 + m_1^2 M_3\right] du, \tag{12}$$

$$2m_T = \frac{1}{4\rho_I} \int_0^1 \left(1-u^2\right)\left[m_1^2 M_1 + M_2 + m_3^2 M_3\right] du, \tag{13}$$

$$2p_T = \frac{1}{4\rho_I} \int_0^1 \left\{ \left[u^2 \frac{m_1^2}{\rho_I} + \left(1-u^2\right)\frac{m_3^2}{\rho_{III}} + 2\frac{m_1 m_3 u\sqrt{1-u^2}}{\sqrt{\rho_I \rho_{III}}} \right] M_1 + \frac{u^2}{\rho_I} M_2 \right.$$

$$\left. + \left[u^2 \frac{m_3^2}{\rho_I} + \left(1-u^2\right)\frac{m_1^2}{\rho_{III}} - 2\frac{m_1 m_3 u\sqrt{1-u^2}}{\sqrt{\rho_I \rho_{III}}} \right] M_3 \right\} du \tag{14}$$

$$Q_I = \frac{1}{2\rho_I} \int_0^1 \left[m_1^2 N_1 + N_2 + m_3^2 N_3\right] du, \tag{15}$$

$$Q_{III} = \frac{1}{\rho_{III}} \int_0^1 \left[m_3^2 N_1 + m_1^2 N_3\right] du, \tag{16}$$

where density is defined as $\rho=(\rho_I,\rho_{III})$ and $u=\cos\theta$, those are related to m_1, m_3 and D, which are defined as:

$$m_1 = \sqrt{\frac{\rho_I}{D}} \left[\frac{p_0}{2}\left(1-u^2\right) + n_0 u^2 - \rho_{III} V_1^2 \right] \tag{17}$$

$$D = \rho_I \left[\frac{p_0}{2} + \left(n_0 - \frac{p_0}{2} \right) u^2 - \rho_{III} V_1^2 \right]^2 + \rho_{III} \left(q_0 + \frac{\rho_0}{2} \right)^2 \left(1-u^2\right) u^2 \tag{18}$$

$$D = \rho_I \left[\frac{p_0}{2} + \left(n_0 - \frac{p_0}{2} \right) u^2 - \rho_{III} V_1^2 \right]^2 + \rho_{III} \left(q_0 + \frac{\rho_0}{2} \right)^2 \left(1 - u^2 \right) u^2 \tag{19}$$

In Eqs. 10 to 16, M_r and N_r are auxiliary functions expressed as:

$$M_r = \alpha \frac{\epsilon(z)}{V_i^2 \left| \varphi_n \right|^3}, \tag{20}$$

$$N_r = \alpha \frac{1 - \epsilon(z)}{\left| \varphi_n \right|^3} \tag{21}$$

where V_i is the phase velocity of the wave, α is the aspect ratio that relates to the term φ_n with the cosine of incident angle (θ) mentioned above, as:

$$\varphi_n = \sqrt{\left[1 + \left(\alpha^2 - 1 \right) u^2 \right]} \tag{22}$$

and the term z refers to the relationship between the normalized angular frequency (ϖ), the phase velocity of the wave (V_i) and the compressional wave velocity of the matrix (V_m):

$$z = \frac{\varpi \varphi_n}{V_i} V_m \tag{23}$$

The subscript i=1…3, is associated with the three types of wave velocity, V_P, V_{SV}, and V_{SH} which depends on the angle of incidence. If the z is substituted in M_r and N_r, then result M_1, M_2, M_3 and N_1, N_2, N_3.

Finally, $\in (z)$ is represented as:

$$\epsilon \left(z \right) = \frac{3\left(1 - iz \right)\left(\sin \sin z - z \cos \cos z \right) e^{iz}}{z^3} \tag{24}$$

Appendix B: Transversally isotropic moduli

Mavko *et al.* (2009) present a transversely isotropic Young's modulus as the uniaxial stress is applied along x_3 is:

$$E_{33} = \frac{\sigma_{33}}{\varepsilon_{33}} = c_{33} - \frac{2c_{31}^2}{c_{11} + c_{12}} \tag{25}$$

and the Poisson's ratio is defined as:

$$\nu_{31} = -\frac{\varepsilon_{11}}{\varepsilon_{33}} = \frac{c_{31}}{c_{11} + c_{12}}. \tag{26}$$

The elastic constants of the stiffness matrix are required in the anisotropic moduli mentioned above, these are:

$$c_{11} = \rho V_P^2 \left(90°\right) \tag{27}$$

$$c_{12} = c_{11} - \rho V_{SH}^2 \left(90°\right) \tag{28}$$

$$c_{33} = \rho V_P^2 \left(0°\right) \tag{29}$$

$$c_{44} = \rho V_{SH}^2 \left(0°\right) \tag{30}$$

to calculate c_{13}, it was considered the formulation reported by Pyrak-Nolte *et al.* (2017):

$$c_{13} = \sqrt{\left[2\rho V_{P45°}^2 - \frac{\left(c_{11} + c_{33}\right)}{2} - c_{44}\right]^2 - \frac{\left(c_{11} - c_{33}\right)^2}{4}} - c_{44} \tag{31}$$

Thomsen's parameters are also defined in terms of elastic constant (Thomsen, 1986) as:

$$\varepsilon \equiv \frac{c_{11} - c_{33}}{2c_{33}} \tag{32}$$

$$\gamma \equiv \frac{c_{66} - c_{44}}{2c_{44}} \tag{33}$$

$$\delta \equiv \frac{\left(c_{13} + c_{44}\right)^2 - \left(c_{33} - c_{44}\right)^2}{2c_{33}\left(c_{33} - c_{44}\right)} \tag{34}$$

Appendix C: Differential Effective Medium model

The Differential Effective Medium (DEM) consider a host material with multiple random inclusions. The process indicates that inclusions are added to the matrix until the composite's proportion is reached (Cleary *et al.*, 1980, Norris, 1985, Zimmerman, 1991). According to Berryman (1992), the equations to estimate effective bulk and shear moduli are:

$$(1-y)\frac{d}{dx}\left[K^*(y)\right]=\left(K_2-K^*\right)P^{(*2)}(y) \tag{35}$$

$$(1-y)\frac{d}{dx}\left[\mu^*(y)\right]=\left(\mu_2-\mu^*\right)Q^{(*2)}(y) \tag{36}$$

where K_1 and μ_1 are bulk and shear moduli of the host in the initial conditions $K^*(0)=K_1$ and $\mu^*(0)=\mu_1$, K_2 and μ_2 are bulk and shear moduli of the inclusions, and y is the concentration of the inclusions. P and Q are coefficients for shapes as spheres, needles, disks, and penny cracks (Berryman, 1995). The aspect ratio is included only in penny crack shape.

Original paper

https://doi.org/10.22201/igeof.00167169p.2021.60.4.2119

Wavelet-based Characterization of Seismicity and Geomagnetic Disturbances in the South Sandwich Microplate Area

P. Larocca[1]* M. A. Arecco[1,2] y M. Mora[1]

Recived: November 24, 2020; accepted: Jun 21, 2021; published online: October 1, 2021.

Resumen

En este trabajo se analizan perturbaciones geomagnéticas relacionadas con eventos sísmicos localizados en el margen transcurrente norte de la micro Placa de Sandwich del Sur y la placa Sudamericana, con epicentro a distancias menores de 350 km del observatorio geomagnético King Eduard Point en el archipiélago de las islas Georgias del Sur.

Se estudian registros del campo geomagnético medido en tres observatorios de la red INTERMAGNET próximos a la zona de estudio en un lapso de 1 año. Es posible detectar variaciones anómalas en los registros geomagnéticos en lapsos de aproximadamente 3 horas antes de la manifestación de eventos sísmicos de magnitud superior a 4,4 Mw.

A partir del análisis de las diferencias entre las componentes horizontales del campo de los observatorios King Eduard Point y Orcadas y el espectro de frecuencias de las observaciones de campo geomagnético, a partir del método de wavelet es posible observar oscilaciones de varios nT previas al evento, además de picos magnéticos de amplitud y duración variable.

Cabe destacar que en el periodo de estudio no se registraron tormentas geomagnéticas intensas o superintensas por encontrarse en fase de baja actividad solar (mínimo de ciclo solar 24).

La observación de estos posibles premonitores magnéticos sugiere que hay un tiempo de preparación crítico en una región de fallas geológicas relacionado con la tensión generada en las rocas previo a la liberación de la energía acumulada en la zona del hipocentro, en el interior de la litosfera, que podría anticipar el movimiento mecánico a partir de registros geomagnéticos anómalos.

Palabras clave: variaciones geomagnéticas, sismos, índices de actividad geomagnética.

*Autor de correspondencia: *plarocc@fi.uba.ar*

[1] *Universidad de Buenos Aires, Facultad de Ingeniería, Instituto de Geodesia y Geofísica Aplicadas, Buenos Aires, Argentina.*

[2] *Universidad de la Defensa Nacional, Instituto Universitario Naval, Escuela de Ciencias del Mar, Buenos Aires, Argentina.*

Abstract

This paper analyzes geomagnetic disturbances associated with seismic events in the northern transcurrent margin of the South Sandwich microplate and South American plate, with their epicenter at distances within 350 km from King Edward Point geomagnetic observatory on the archipelago of the Georgias del Sur islands.

Geomagnetic field records measured over a one-year period in three observatories of the INTERMAGNET network near the area under study are examined. Anomalous variations in geomagnetic records can be detected within approximately 3 hours before the manifestation of seismic events with a magnitude above 4.4 Mw.

Based on the analysis of the differences in horizontal field components among the observatories and the frequency spectrum of the geomagnetic field observations using the wavelet method, oscillations of several nT can be observed before an event, in addition to magnetic peaks with variable amplitude and duration.

It is worth noting that, during the period of study, no severe geomagnetic storms were recorded as this was a phase of low solar activity (solar cycle 24 minimum).

The observation of these potential magnetic precursors suggests that there is a critical preparatory period in a region with geological faults related to the stress generated in the rocks before the built-up energy is released in the hypocenter area, within the lithosphere, which may possibly predict the mechanical motion based on anomalous geomagnetic records.

Key words: geomagnetic variations, earthquakes, geomagnetic activity indices.

Introduction

One of the most elusive objectives for seismology is being able to predict an earthquake in the short term. There are numerous studies reporting relationships between earthquakes and physical phenomena, such as significant mechanical effects in the focal area of an earthquake, whether rock changes or deformation; changes in rock properties and stress-deformation state; changes in the chemical composition and/or temperature of the groundwater; electrophysical properties of the medium; increased emanations of natural radon and excitation of seismic signals: all of this affects the regimes of geophysical fields (Hayakawa *et al.* 2010; Takeuchi *et al.* 2012, Varotsos *et al.*, 2013; Spivak and Riabova, 2019).

The geomagnetic field is no exception. It was repeatedly observed that geomagnetic field disturbances occurred during the preparation stage of an earthquake (Kushwah *et al.*, 2009; Ruiz *et al.*, 2011; Takla *et al.*, 2018).

The geomagnetic field that is measured on the earth's surface is the vector sum of various constituent fields, each of which has a different origin and varies differently in time and space. It is mainly made up of two constituents: a global one with great amplitude, whose source is within the earth, and the other one, with a much lesser amplitude, created by more superficial sources. Onlapping them is the outer field caused by electric currents circulating in the ionosphere and the magnetosphere which, when varying in time, generate induced fields. (Mandea and Purucker, 2005, Tackla *et al.*, 2018).

Over 90 percent of the measured field is generated in the outer core of the earth. This part of the geomagnetic field slowly varies in time and can be described by means of mathematical models, such

as the International Geomagnetic Reference Field (IGRF) and the World Magnetic Model (WMM) (Alken *et al.*, 2021, Rother *et al.*, 2021).The intensity of the magnetic signal from rocks is usually below 1 percent of the intensity of the earth's main magnetic field. However, with a geomagnetic field model (for example, the IGRF), these small signals may be recovered from the data measured (Skordas and Sarlis, 2014). Geomagnetic studies can contribute to providing information on the subsoil and the process involving an earthquake.

There are a lot of studies on the mechanisms (Ryu *et al.* 2014) that cause the ionospheric disturbances coupled to seismic activities. Furthermore, recent statistical studies using ground and satellite data have provided convincing correlations between the seismic activities and the ionospheric disturbances preceding earthquakes [Fujiwara *et al.*, 2004; Liu *et al.*, 2006, Larocca *et al.*, 2019].

The analysis of indices of solar and geomagnetic activity serves to account for how rapid variations of geomagnetic activity influence data processing. Dst, Ap and F10.7 cm indices are usually used to monitor this phenomenon (Tsurutani *et al.*, 1997, 1999). The intensity of the equatorial magnetic field, measured by the *Dst* index, is directly related to the total kinetic energy of the ring current particles (Rostoker *et al.*, 1997), thus, the *Dst* index is also often used to determine whether or not a storm occurred, to define the duration of a storm, and to distinguish between quiet and disturbed geomagnetic conditions. *Ap* index characterizes the intensity of geomagnetic activity at planetary scale from the measurement of the horizontal component of the magnetic field observed in 13 stations, of which 11 correspond to the northern hemisphere and two to the south and the solar index F10.7cm measures the radio emissions *F10.7*cm that originate in the upper atmosphere (Perrone & De Franceschi, 1998).

The subduction zone of the South American plate beneath the South Sandwich plate, located in the South Atlantic, is one of the areas with highest seismic activity in the planet —within a year, over 300 seismic events of Mw > 4.1 may occur. This small plate is bounded to the north and east by the South American plate; to the south, by the Antarctic plate; and to the west, by the Scotia plate. The subduction zone shows an active volcanic and tectonically simple intra-oceanic arc. The active arc is largely built on the oceanic crust of the small South Sandwich plate, which was formed approximately 10 Ma ago in the spreading center of the East Scotia ridge (Leat *et al.*, 2003). The arc is being formed in response to an inclined subduction of the South American plate beneath the South Sandwich plate at a velocity of 67–79 km / Ma (Thomas *et al.*, 2003); within a year it accounts for a relative displacement of 7 to 8 cm.

This paper sets out to examine the occurrence of any changes in the earth's magnetic field associated with seismic events of the small South Sandwich plate, in a one-year period from May 17, 2018 to the same date in 2019. To this end, magnetic data records of three observatories closest to the study area were studied, namely King Edward Point (KEP), located in the vicinity, Port Stanley (PST) on the Malvinas islands, and Orcadas (ORC) on the Orcadas del Sur islands, located farther away, in the cited period based on filter processing and wavelet analysis of their differences.

Data and Methodology

This paper used the value of the International Geomagnetic Reference Field available at https://www.ngdc.noaa.gov/geomag/data.shtml as a reference value for the three magnetic observatories, which was then subtracted from their daily observations for the one-year period between May 17, 2018

and May 17, 2019. Data were acquired per minute from observatories King Edward Point (KEP) (54.3° S; 36.5° W), located in the vicinity of the transcurrent margin, Port Stanley (PST) (51.7° S; 57.8° W), and Orcadas (ORC) (60.7° S; 44.7° W). These data were obtained from the International Real-time Magnetic Observatory Network (INTERMAGNET) with a 1-minute resolution, available at https://intermagnet.github.io.

Nearly 300 seismic events of Mw > 4.4 and their respective depths, as extracted from the United States Geological Survey (USGS, https://earthquake.usgs.gov/earthquakes/), were analyzed (Figure 1).

In addition, in order to take into account the rapid variations of the geomagnetic field, this study included information from geomagnetic indices *Dst, Ap* and the solar index F10.7cm. Dst —monitoring the variations of the horizontal component of the earth's magnetic field due to an increase in the ring current derived from a network of geomagnetic observatories symmetrically located in the equatorial area, and measured in nT. The value of the *Dst* index is statistically zero on days considered quiet. *Dst* index is reported by Kyoto University in hourly values. During a geomagnetic storm, its value falls to a minimum value and then recovers to zero. According to the minimum value reached, the onset of an intense storm is considered if *Dst*> -100 nT (Sugiura and Chapman, 1960; Sugiura, 1964), which does not occur in our study period. *Ap* index is reported daily, nevertheless its sampling rate is supposed to be three hourly. Values of *Ap* > 40 nT provide a maximum disturbance measure useful to identify major geomagnetic storms (Perrone and De Franceschi, 1998) but in these periods of time, they are lowest; and *F10.7 cm* solar index is an excellent indicator of the solar activity originating high in the chromosphere and in the corona of the solar atmosphere, and it is reported in "solar flux units" (sfu); as obtained from the Geomagnetic Data Service of Kyoto (http://wdc.kugi.kyoto-u.ac.jp/wdc/Sec3.html). On the other hand, the value of the radio flux index was always below 70 sfu.

The methodology used involved studying intervals with a length from 7 to 10 days, which included seismic events, throughout the year. Because the closest Geomagnetic observatory to the study area is KEP Observatory, it was decided to focus the study on the analysis of the data recorded there.

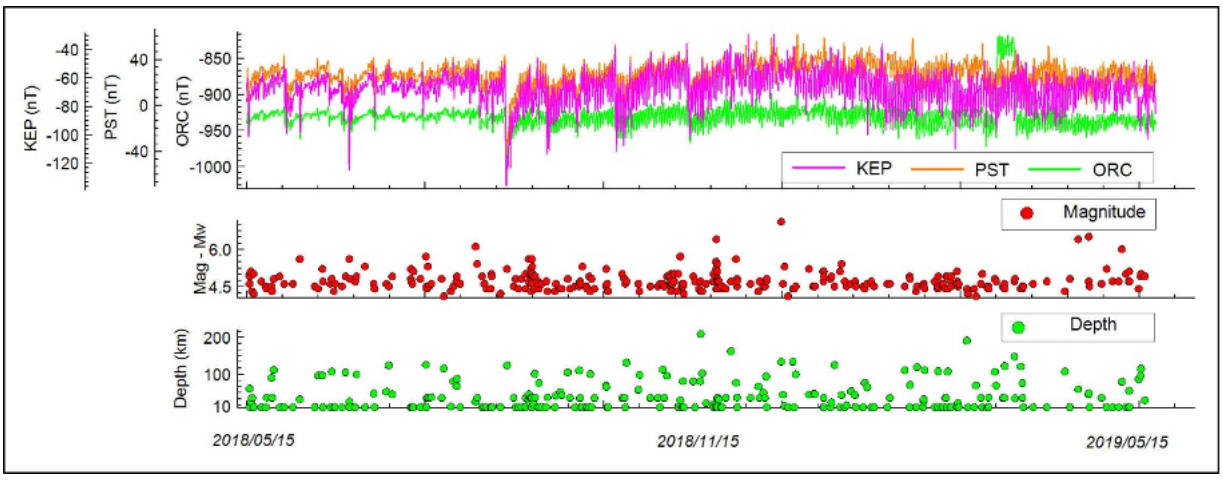

Figure 1. Daily variations of the H component of the earth's magnetic field in PST, KEP and ORC observatories. Magnitudes of earthquakes and their depths during the year of study.

The technique to identify potential anomalous variations of the earth's magnetic field implied examining the wavelet power spectra of magnetic data from KEP Magnetic Observatory, separately analyzing the horizontal and vertical components of the magnetic field measured, and subsequently analyzing the horizontal component with the application of a low pass filter to attenuate the diurnal anomaly (Grinsted *et al.*, 2004) and to be to identify anomalous frequencies around the earthquake detection time.

In addition, in such intervals, for the purposes of isolating the magnetic field caused by the local geomagnetic variation due to solar variability, the field differences (Δ) between KEP and ORC observatories (Δ KEP-ORC) were calculated, the value of the reference magnetic field corresponding to the time and location of each observatory was subtracted. This procedure was used to accentuate the effects of seismic activity given KEP's proximity to the South Sandwich plate. Afterwards, wavelets (wt) were applied with Morlet exponential decay to the time series obtained from the difference of the data recorded (only the horizontal component of the geomagnetic field is analyzed as it is most susceptible to its rapid variations).

Results

Seven representative seismic events were chosen to describe the results obtained (Table 1). These events were selected due to their closeness to King Edward Point observatory (less than 350 km).

Table 1.Selected seismic events close to King Edward Point geomagnetic observatory.

No.	Date	Time	Lat. (°)	Long. (°)	Depth (km)	Mag	Type of Mag.	Place
*1	5/24/2018	12:47	-54.9892	-32.118	10	4.5	Mb	294km ESE of Grytviken
*2	7/05/2018	19:23	-55.096	-30.9409	10	4.4	Mb	240km ESE of Grytviken
*3	9/21/2018	19:07	-55.0491	-33.4245	10	4.5	Mb	216km ESE of Grytviken
*4	9/26/2018	05:28	-55.3485	-31.3375	10	4.5	Mb	298km WNW of Visokoi Island
*5	9/26/2018	14:31	-55.0642	-31.3753	10	4.4	Mb	298km WNW of Visokoi Island
*6	10/11/2018	09:49	-55.1947	-30.9411	10	4.6	Mb	287km NW of Visokoi Island
*7	4/05/2019	16:14	-55.9206	-27.856	58.6	6.4	Mb	95km NW of Visokoi Island

The events selected occurred during periods characterized by the absence of significant magnetic activity manifestations, resulting from the analysis of the geomagnetic indices *Dst, Ap* and the solar index *F10.7cm* as qualitative indicators of the activity, as shown on Figure 2. During the solar minimum the large-scale dynamics of the interplanetary medium is dominated by the stream interaction regions, which they produce most of the small and moderate geomagnetic storms during this period. The space weather events during the solar minimum, are mainly associated with stream interaction regions. Then the geomagnetic activity is not produced by solar flares o coronal mass ejections, but by interaction regions.

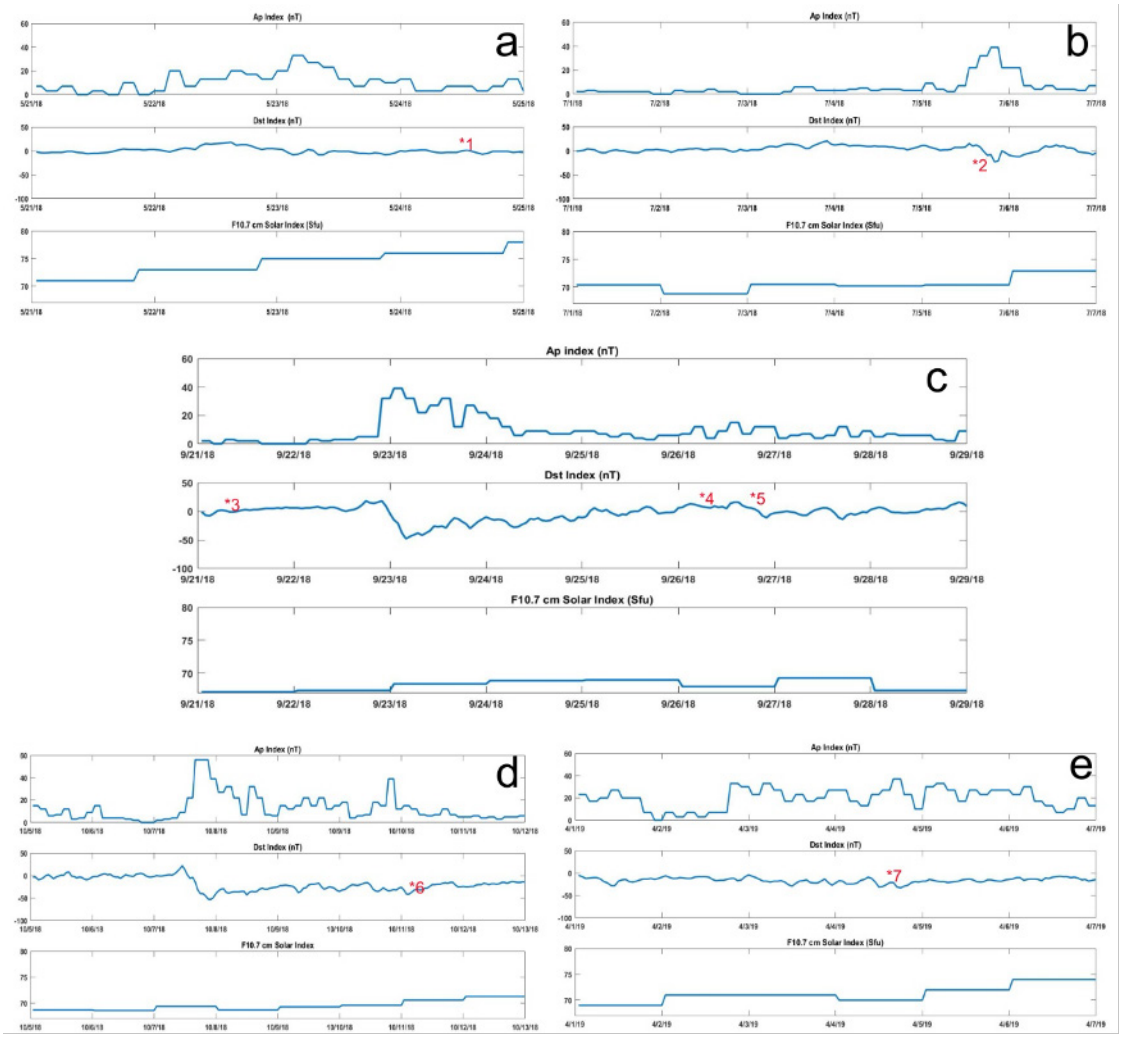

Figure 2. Solar indices *Ap* (nT), *Dst* (nT) and *F10.7* cm (SFU=10^{-22} Wm^{-2} Hz^{-1}) corresponding to periods 21-26 May, 2018; 1-7 July, 2018; 20-27 September, 2018; 5-13 October, 2018; and 1-7 April, 2019.These indices account for a low solar activity period.

Storm type according to Loewe & Prolss (1997) can be classified: a weak storm if it has –30 nT > *Dst* > –50 nT, a moderate storm if it has –50 nT > *Dst* > –100 nT, a strong storm if it has –100 nT > *Dst* > –200 nT, a severe storm : –200 nT > *Dst* > –350 nT, and a great storm with *Dst* < -350 nT. Then, in the selected periods, only two weak storms were observed on 9/22/18 and 10/8/18 with *Dst* ~-48 nT. The study shows that the small geomagnetic variations, presumably associated with seismic events, there were not in fact driven by solar wind stream interactions hitting the Earth's environment because they do not temporarily match those chosen for observation.

For the seven events selected, the magnetic field determined in KEP observatory was plotted, including both its horizontal and vertical components, showing anomalous variations in both components before a seismic event, although with better resolution in the horizontal component. In order to subtract the contribution of the diurnal solar variation and some weak events associated with space weather phenomena, the difference between the horizontal components from KEP and ORC observatories was calculated, and it was subsequently applied a low-pass filter (filtered signal). For

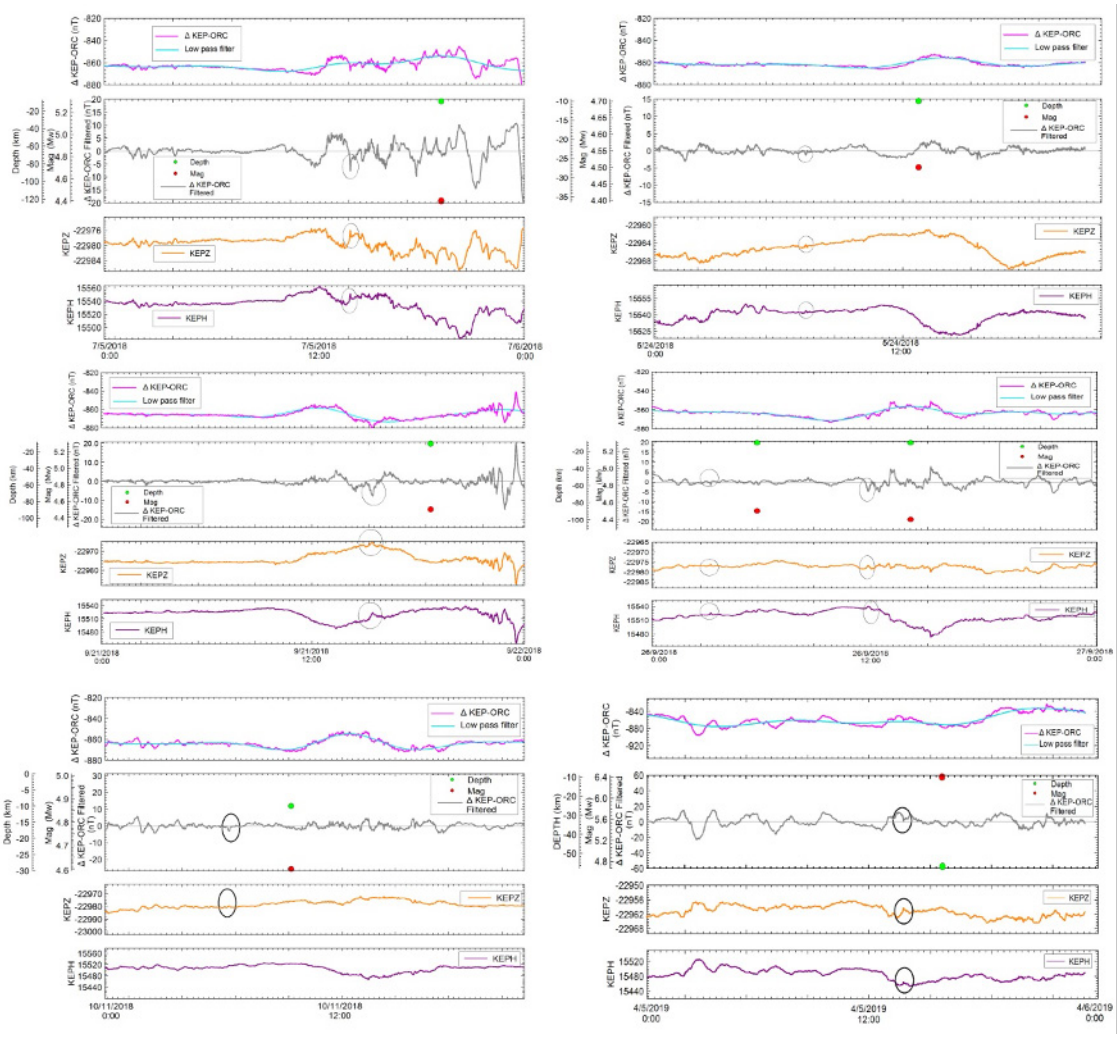

Figure 3. Magnetic data of 24 May, 2018; 5 July, 2018; 21 and 26 September, 2018; 11 October, 2018; and 5 April, 2019. Difference between magnetic data from KEP and ORC observatories.

the purposes of finding small field variations, the differences between Δ KEP-ORC and the filtered signal, were calculated (Figure 3). In all the seismic events, peaks were seen both in the H and Z components, as well as in the filtered variation, as shown on Table 2.

Table 2. Intensity of the peaks observed in figure 3 on the difference of the magnetic data recorded in the KEP and ORC observatories and their anticipation to seismic events.

No.	Date	Magnitude	Peak intensity (nT)	Anticipation (hours)
*1	05/24/2018	4.5	1.56	2h 47m
*2	07/05/2018	4.4	4.4	5h 10m
*3	09/21/2018	4.5	7.58	3h 30m
*4	09/26/2018	4.5	1.49	3h 00m
*5	09/26/2018	4.4	3	2h 30m
*7	04/05/2019	6.4	3.1	2h 07m

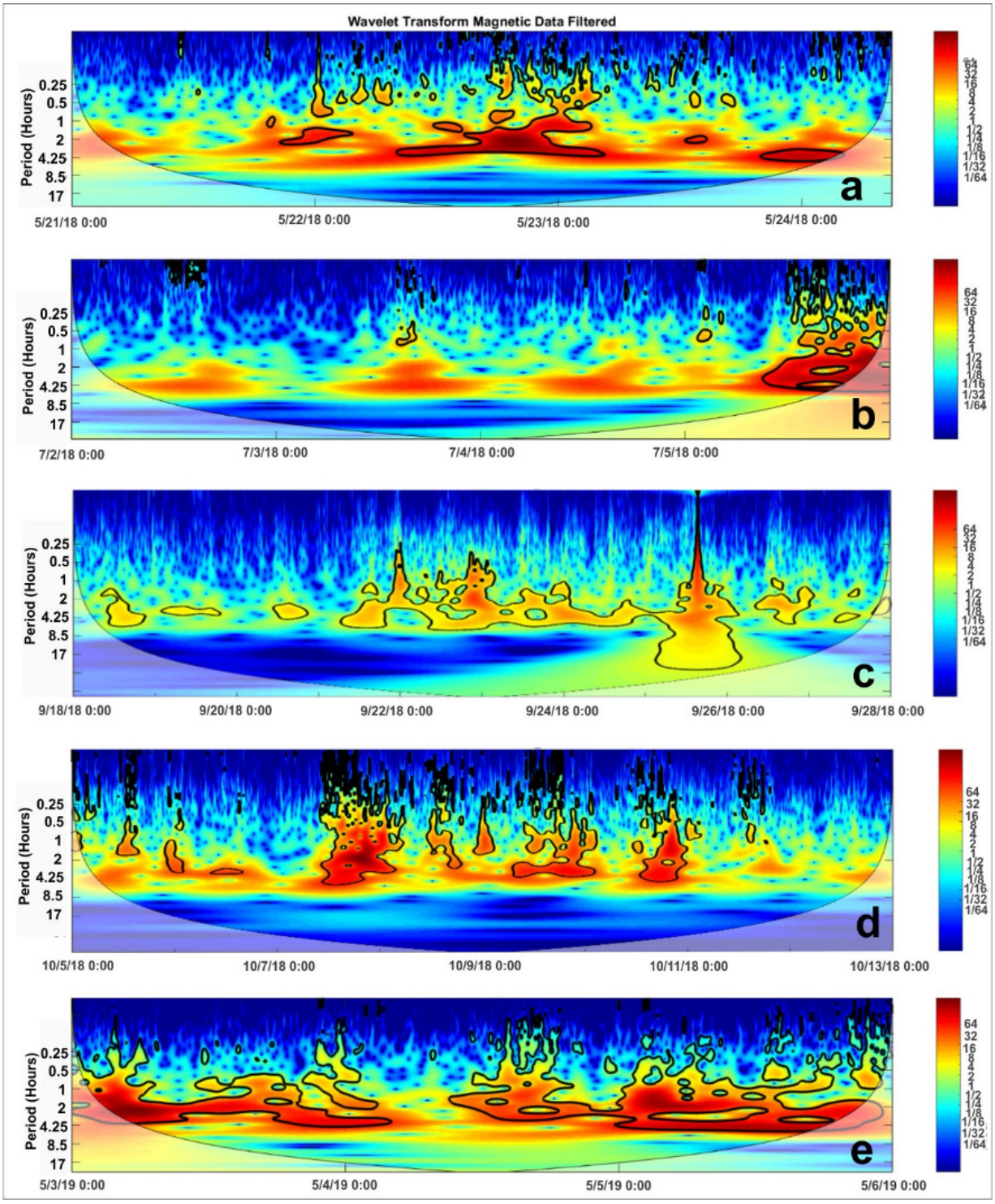

Figure 4. Continuous wavelet transform of the periods from 21 to 24 May, 2018; from 2 to 6 July, 2018; from 18 to 28 September, 2018; from 5 to 12 October, 2018; and from 3 to 6 April 2019 for ΔKEP-ORC The data shown corresponds to the difference between the horizontal components of the magnetic records of the KEP and ORC observatories, where the corresponding local IGRF contribution had already been discounted. These data were called: Filtered data in the figure. The thick black contour shows a 5% significance level against the red noise background, and the cone of influence (COI) where the edge effects may distort the image is blurred.

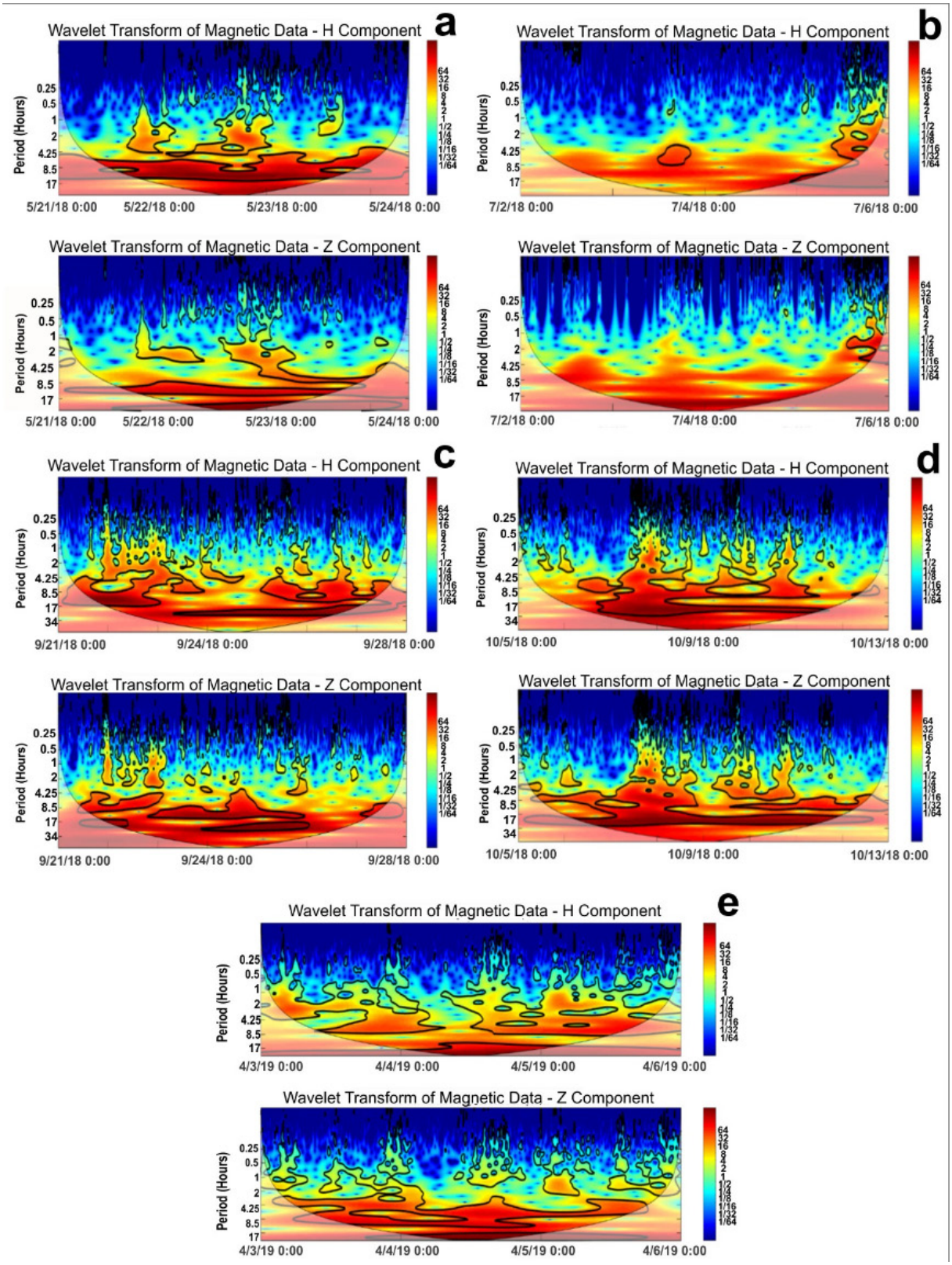

Figure 5. H and Z from 18 to 28 Septembercorresponding to the periods from 21 to 24, May 2018; from 2 to 6 July, 2018; from 18 to 28 September, 2018; from 5 to 12 October, 2018; and from 3 to 6 April, 2019.

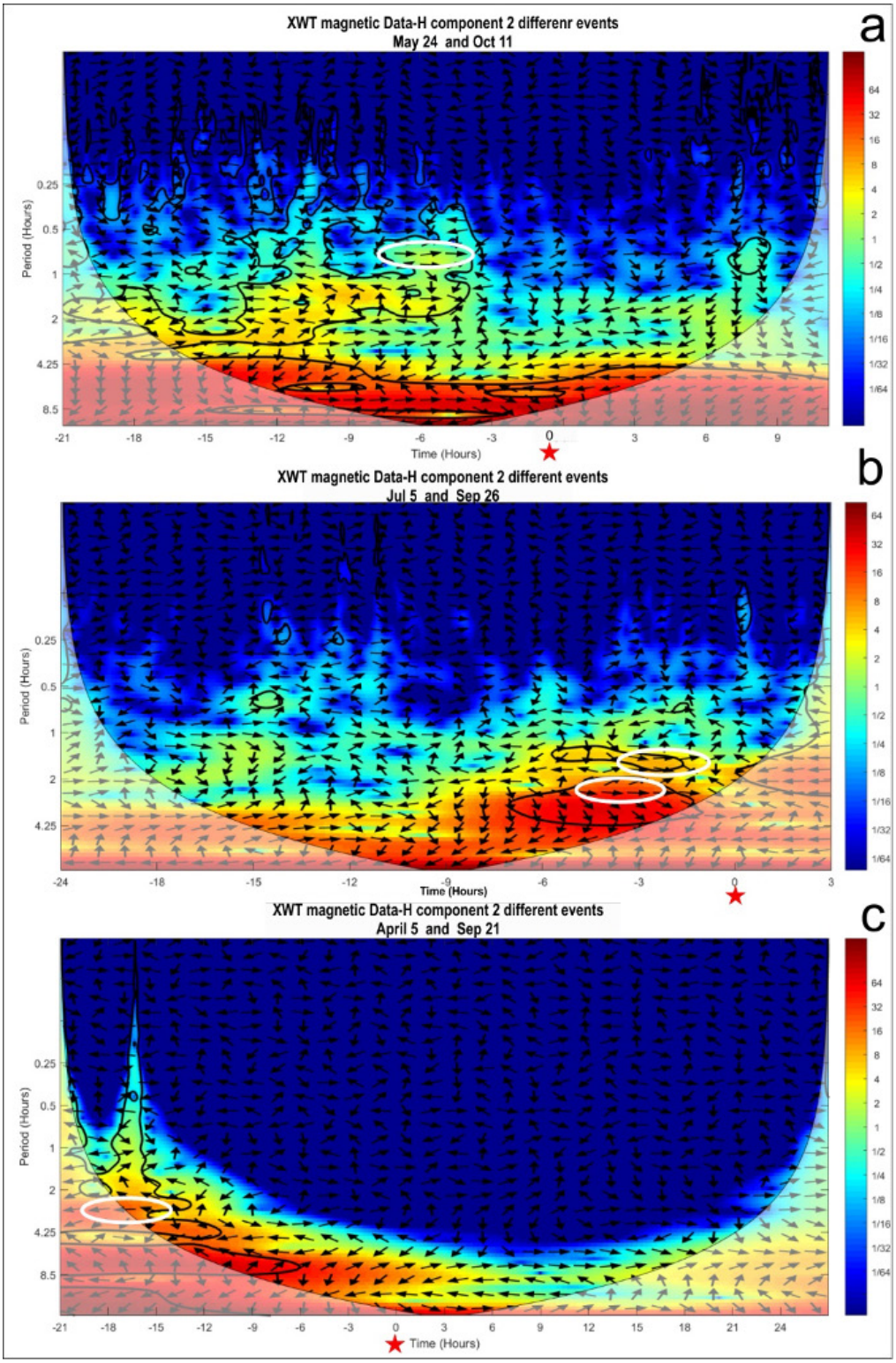

Figure 6. Geomagnetic field XWT from KEP observatory for the following events: a) 24 May and 11 October, 2018; b) 5 July and 26 September, 2018; and c) 21 September, 2018 and 5 April, 2019. Seismic event coincidence instant (red star) and coherent phase (white oval). The arrows show the relative phase (with the phase pointing to the right and the anti-phase pointing to the left).

In addition, the continuous wavelet transform (WT) was applied both to ΔKEP-ORC (Figure 4) and to each H and Z component of the magnetic field observed in KEP (Figure 5). The Morlet wavelet (with $\omega_0 = 6$) was used, as it provides a good balance between the time and frequency location. Figures 4 and 5 show the periodic oscillation of these magnetic data from 21 to 24 May, 2018; from 2 to 6 July, 2018; from 18 to 28 September, 2018; from 5 to 12 October, 2018; and from 3 to 6 April, 2019.

We examined two time series whose interval had the earthquake occurrence moment as a common instant. For the purposes of correlating periodicities between both series, we inspected these series together so as to find common frequencies. Based on their WTs, we constructed the Cross Wavelet Transform (XWT), which exposes their common power and relative phase in the time-frequency space. We used the corresponding software at http://noc.ac.uk/using-science/crosswavelet-wavelet-coherence. Figure 6 shows the result.

We applied a measure of the coherence between both WTs, referred to as wavelet transform coherence (WTC), so as to find significant coherence. If both series are physically related, we should expect a consistent or slowly varying phase. Monte Carlo methods are used to assess the statistical significance against red noise backgrounds.

There are clearly common characteristics in the wavelet power of the paired series, showing on Figure 6 a) and b) very good correlation in the interval between 6 and 4 hours before the occurrence of an earthquake corresponding to a period between 2 and 0.5 hours. For Figure 6 c), the correlation is inverse and it occurs more than 15 hours earlier.

Conclusions

Potential magnetic precursors could be identified for events with a magnitude above 4.4 Mw.

In all the events, peaks between 1.5 and 4.4 nT were observed in the filtered variation around 3 hours before a seismic event, and a 7.58 nT peak corresponding to the earthquake closest to KEP observatory outstands. Their association with solar storms is ruled out as this is a solar minimum period.

The filtering operation to yield the filtered variation was effective, as the wavelet transform studies do not show periods for 24 hs, 12 hs or 6 hs.

When observing the wavelet transform both in the horizontal H and vertical Z components, high coherence was found around the corresponding 2 to 0.25 hour band, which increases over a period near the occurrence of a seismic event, but, as no filters were applied in this case, the diurnal and semi-diurnal components are those with highest energy.

The study of time correlation among seismic events, such as those on 24 May and 11 October, 2018; 5 July and 26 September, 2018; and 21 September, 2018 and 5 April, 2019, using an independent method based on the Cross Wavelet Transform (XWT) (Grinsted *et al.*, 2004), showed that, in a period from 2 to 3 hours before an earthquake, there is high coherence between both analyses, which may be characterizing an alteration in the magnetic field due to seismic activity. This period increases to over 15 hours when the comparison involves a deeper and more intense earthquake, but farther away from the location where the magnetic field is recorded.

It would be inferred that there is a connection between geomagnetic variations and seismic events, nevertheless some signals show similar signatures as those highlighted and not associated to earthquakes.

Further evidence is needed for a better assessment of potential geomagnetic phenomena associated with earthquakes, which is why continuous monitoring is intended over a longer period, including more significant events making it probable to find possible correlations with seismic activity.

Acknowledgements

We thank the referees for their valuable comments.

This work has been supported by the research projects of Science and Technology of the University of Buenos Aires, Argentina, No. 200201601000088BA (UBACYT) and Strategic Research of the University of National Defense No. 279/2018 (UNDEFI), Argentina.

Wavelet software was provided by C. Torrence and G. Compo, and is available at URL: http://atoc.colorado.edu/research/wavelets/.

References

Alken, P., Thébault, E., Beggan, C.D. et al., 2021. International Geomagnetic Reference Field: the thirteenth generation. *Earth Planets Space*, 73, 49. doi: 10.1186/s40623-020-01288.

Fujiwara, H., Kamogawa, M., Ikeda, M., Liu, J. Y. , H. Sakata, H., Chen, Y. I., Ofuruton, H., Muramatsu, S., Chuo, Y. J. and Ohtsuki, Y. H., 2004. Atmospheric anomalies observed during earthquake occurrences, *Geophys.* Res. Lett., 31, L17110. doi:10.1029/2004GL019865.

Grinsted, A., Moore J. C., and Jevrejeva S., 2004. Application of the cross wavelet transform and wavelet coherence to geophysical time series. *Nonlin.* Process. *Geophys.*, 11, 561-566.

Hayakawa, M., Kasahara, Y., Nakamura, T., Muto, F., Horie, T., Maekawa, S., Hobara, Y., Rozhnoi, A. A., Solovieva, M., and Molchanov, O. A. (2010), A statistical study on the correlation between lower ionospheric perturbations as seen by subionospheric VLF/LF propagation and earthquakes, *J. Geophys. Res.*, 115, A09305, doi:10.1029/2009JA015143.

INTERMAGNET International Real-time Magnetic Observatory, https://intermagnet.github.io, last modified date: 2020-02-02.

Kushwah V, Singh V, and Singh B., 2009, Ultra-low frequency (ULF) amplitude observed at Agra (India) and their association with regional earthquakes. *Phys.Chem Earth.* 34, 367–272.

Larocca, P., Fiore, M., Oreiro F., Vilariño, I. and Arecco, M.A., 2019. Estudio de parámetros geo-magnéticos y su posible influencia sobre anomalías sismo-ionosféricas. In Proceedings of the Sixth Biennial Meeting of Latinmag, Fernando Poblete, C. I. Caballero M, (Eds), *Latinmag Letters*, 9, Special Issue, A18-P, 1-6.

Leat, P.T., Smellie, J.L., Millar, I.L. and Larter, R.D., 2003. Magmatism in the South Sandwich arc. In: Larter, R.D., Leat, P.T. (Eds.), *Intra-Oceanic Subduction Systems: Tectonic and Magmatic Processes.* Geological Society, London Special Publications, 219, 285–313.

Liu, J. Y., Y. I. Chen, Y. I., Chuo, Y. J. and Chen C. S., 2006. A statistical investigation of preearthquake ionospheric anomaly, *J. Geophys. Res.*, 111, A05304, doi:10.1029/2005JA011333.

Loewe, C. A., and Prölss, G. W., 1997. Classification and mean behavior of magnetic storms, *J. Geophys. Res.*, 102 (A7), 14209– 14213, doi:10.1029/96JA04020.

Mandea, M. and Purucker, M., 2005. Observing, Modeling and Interpreting Magnetic Fields of the Solid Earth. *Surv Geophys* 26, 415–459. doi: 10.1007/s10712-005-3857-x

Perrone L., and De Franceschi G., 1998. Solar, ionospheric and geomagnetic indices, Ann. Geofis., 41 (5-6), 843-855.

Rostoker, G, Friedrich, E. and Dobbs, M., 1997. Physics of magnetic storms. *Magnetic storms*, 98, 149-160.

Rother M., Korte M., Morschhauser A. , Vervelidou F., Matzka J. and Stolle C., 2021. The Magnum core field model as a parent for IGRF-13, and the recent evolution of the South Atlantic Anomaly. *Earth, Planets and Space*, 50-73. https://doi.org/10.1186/s40623-020-01277-0.

Ruiz, F., Sánchez, M., Martínez. P., Giménez, M., Leiva, F., Álvarez, O. and Introcaso, A., 2011. La estación magnética Zonda: estudio de perturbaciones magnéticas relacionadas con terremotos. San Juan, Argentina. *Latinmag Letters*, 1, Special Issue, A16, 1-7.

Ryu, K., Parrot, M., Kim, S. G., Jeong, K. S., Chae, J. S., Pulinets, S. and Oyama K. I.. 2014. Suspected seismo-ionospheric coupling observed by satellite measurements and GPS TEC related to the M7.9 Wenchuan earthquake of 12 May 2008, *J. Geophys. Res. Space Physics*, 119, doi:10.1002/2014JA020613.

Skordas E. S. and Sarlis N. V., 2014. On the anomalous changes of seismicity and geomagnetic field prior to the 2011 Mw 9.0 Tohoku earthquake. *Journal of Asian Earth Sciences*. Elsevier 80, 161-164Ltd. doi.org/10.1016/j.jseaes.2013.11.008.

Spivak, A. A., and Riabova, S. A., 2019. Geomagnetic Variations during strong earthquakes. *Physics of the Earth*, 6, 3-12. Doi: 550.385.37:550.388.

Sugiura, M., 1964. Hourly values of equatorial Dst for the IGY, *Ann. lnt. Geophys. Year*, 35, 9.

Sugiura, M. and Chapman S., 1960. The average morphology of geomagnetic storms with sudden commencements. *Abh. Akad. Wiss.* Gottingen, Sonderheft 4.

Takeuchi, A. Okubo, K. and Takeuchi, N., 2012. Electric Signals on and under the Ground Surface Induced by Seismic Waves, *International Journal of Geophysics.* Volume 2012, Article ID 270809, 10 pages, doi:10.1155/2012/270809.

Takla E., A. Khashaba, Abdel Zaher M., Yoshikawa A. and Uozumi T., 2018. Anomalous ultra-low frequency signals possibly linked with seismic activities in Sumatra, Indonesia. *NRIAG Journal of Astronomy and Geophysics*, 7:2, 247-252. doi: 10.1016/j.nrjag.2018.04.004.

Thomas, C., Livermore, R. and Pollitz, F., 2003, Motion of the Scotia Sea plates. *Geophys. J. Int.,* 155, 789–804.

Tsurutani, BT and Gonzalez, WD., 1997. The interplanetary causes of magnetic storms. A review, (In) B T Tsurutam, W D Gonzalez, Y Kamide and J K Aiballo (Eds.) Magnetic Storms. Geophys. Monograph, 98, *AGU*, Washington, D. C., 77-89.

Tsurutani, BT, Kamide, Y. Arballo, JK, Gonzalez, WD and Lepping, R. P., 1999. Interplanetary causes of great and super intense magnetic storms, P*hysics and Chemistry of the Earth*, 24, 101.

U.S. Geological Survey, 2019. Scientific Agency of the Department of the interior, https://earthquake.usgs.gov/earthquakes/ last accessed on June 5, 2019.

Varotsos P. A., Sarlis N.V., Skordas E.S., Lazaridou M.S., 2013, Seismic Electric Signals: An additional fact showing their physical interconnection with seismicity, Tectonophysics, Volume 589, 116-125, doi.org/10.1016/j.tecto.2012.12.020.

Original paper

https://doi.org/10.22201/igeof.00167169p.2021.60.4.2124

Seismic signatures of atmospheric disturbances as a tool for reconstruction of their dynamics

Vyacheslav M. Zobin[1]*

Received: January 22, 2021; accepted: August 31, 2021; published online: October 1, 2021.

Resumen

El viento y los productos de las nevadas y lluvias que tocan el suelo generan las señales sísmicas. Durante décadas, el estudio de las firmas sísmicas de las perturbaciones atmosféricas, ciclones, se basó en el análisis del ruido sísmico ambiental en el rango de baja frecuencia que permitió la identificación de ciclones y la ubicación de la posición de la tormenta. Se propone la metodología de monitoreo de los eventos atmosféricos utilizando las señales sísmicas de período corto, registradas por un sensor instalado a una altura de aproximadamente 4 Km. sobre el nivel del mar en la cumbre del volcán inactivo Nevado de Colima. La metodología incluye la indicación de las señales sísmicas de las perturbaciones atmosféricas en las pantallas de helicorder de registros sísmicas diarias con el siguiente análisis de las formas de onda, producidas por el impacto de las lluvias y nevadas con la superficie del suelo, y sus características espectrales de Fourier. Luego, la reconstrucción del paso de los eventos atmosféricos, en base a las densidades espectrales de potencia de los registros sísmicos de una hora, que se realiza mutuamente con las observaciones satelitales. La metodología se aplicó para estudiar el paso del huracán *Dora* y su tormenta tropical precedente (junio de 2017) y el sistema de frente frío número 25 (enero de 2018). Se indicaron los periodos de acción de tormenta tropical, huracán y dos etapas del frente frío en las imágenes del helicorder. Luego se seleccionaron las formas de onda características para cada período. El análisis de las características espectrales de estas formas de onda demostró que las lluvias, ocurridas durante la tormenta tropical y el huracán y durante la etapa inicial del paso del frente frío, generaron las señales sísmicas dentro del rango de frecuencia entre 1.0-1.8 Hz mientras que las nevadas durante la segunda etapa del paso del frente frío generaron las señales sísmicas dentro del rango de frecuencia entre 2.6 y 3.7 Hz. La reconstrucción de la dinámica del paso de los eventos atmosféricos a partir de las densidades espectrales de potencia de los registros sísmicos de una hora permitió ver la intensidad comparable de tormenta tropical y huracán, y dos etapas del frente frío. Estos resultados demuestran la posibilidad de monitorear el paso de perturbaciones atmosféricas en tiempo real o realizar la reconstrucción de la dinámica de estos eventos durante el tiempo pasado utilizando las señales sísmicas de período corto registradas en las alturas altas.

Palabras clave: señal sísmica, tormenta tropical, huracán, frente frío, lluvia y nevada.

*Corresponding author: vzobin@ucol.mx

[1] *Centro Universitario de Estudios Vulcanológicos, Universidad de Colima, Colima, 28045, México*

Abstract

The wind and products of snowfalls and rainfalls touching the ground generate seismic signals. During decades, the study of seismic signatures of atmospheric disturbances, cyclones, was based on analysis of the ambient seismic noise in the low-frequency range allowing the identification of cyclones and location of the storm position. The methodology monitoring the atmospheric events using short-period seismic signals recorded by a sensor installed at an altitude of about 4 km above sea level at the summit of dormant volcano Nevado de Colima is proposed. The methodology includes the identification of the seismic signatures of atmospheric disturbances on the daily helicorder displays of seismic signals with following analysis of waveforms, produced by the impact of rainfalls and snowfalls with the ground surface, and their Fourier spectral characteristics. Then, the reconstruction of the tracks of the atmospheric events, based on the power spectral densities of the one-hour seismic records, is performed mutually with the satellite observations. The methodology was applied to study the tracks of hurricane *Dora* and its preceding tropical storm (June 2017) and the cold front system number 25 (January 2018). There were indicated the periods of actions of tropical storm, hurricane, and two stages of the cold front on the helicorder images. Then the characteristic waveforms for each period were selected. Analysis of the spectral characteristics of these waveforms demonstrated that the rainfalls, occurring during the tropical storm, hurricane and the initial stage of the cold front tracks, generated the seismic signals within the frequency range between 1.0-1.8 Hz while the snowfall during the second stage of the cold front tracks generated the seismic signals within the frequency range between 2.6 and 3.7 Hz. The comparison of the tracks of the atmospheric events and the power spectral densities of the one-hour seismic records allowed to see the comparable intensity of tropical storm and hurricane, and two stages of the cold front. These results demonstrate the possibility to monitor the tracks of atmospheric disturbances in real time or to perform the reconstruction of the dynamics of these events during past time using the short-period seismic signals recorded at the high altitudes.

Key words: seismic signal, tropical storm, hurricane, cold front, rainfall and snowfall

1. Introduction

Vibrations of the ground may be generated by different natural causes. Among them are the processes acting both below and above the Earth surface such as earthquakes and volcanic activity generated by the activity within the Earth interior as well as hurricanes and snowstorms produced by atmospheric disturbances. The mechanical vibrations, outside the solid Earth, represent a subject of so called "environmental seismology" (Lerose *et al.*, 2015). This article is focused on the study of seismic signals recorded during the tracks of air masses above the Mexican zone of the North American continent along the northwest coast and may be considered as a part of the environmental seismology.

An air mass is a large body of air with relatively uniform thermal and moisture characteristics. Once formed, the air masses migrate within the general circulation. Among the air masses that move above the North American continent, may be identified the continental polar and maritime Pacific tropical masses. A boundary between these two air masses is called a cold front. A cold front is the leading edge of a cooler mass of air, replacing at ground level a warmer mass of air, which lies within a fairly sharp surface trough of low pressure. A cold front occurs when a mass of comparatively colder air moves into where warmer air is presented. When the cold front is passing, winds become gusty; there is a sudden drop in temperature with appearance of heavy rains and snowstorms (Rauber *et al.*, 2012).

Figure 1A illustrates the generation of the cold front No 5 (Frente frio) occurring from 2 to 4 November 2016. The continental polar air masses of the frontal system No 5 entered into the northern part of México and interacted with the maritime Pacific tropical air mass that is shown with the arrows marked as "Entrada de humedad". It is seen that the surface trough of low pressure, shown with yellow dashed lines, was elongated along the total territory of the state. The interaction of cold and warm air masses was accompanied with strong winds reaching 60 km/h in the northern part of México (this zone is shown within a green ellipse). As a result, the rainfalls up to 90 mm and a drop of hails (3 to 5 cm) were observed in a few states of northern México (Reporte, 2016).

Tropical cyclones are low pressure systems that have thunderstorm activity and rotate counterclockwise. The tropical cyclones start from a tropical depression with winds of 60 km/h or less to a tropical storm whose winds reach 60-120 km/h. If the wind of the tropical storm exceeds 120 km/h and occurs in the Atlantic Ocean of northeastern Pacific Ocean, then is called "a hurricane". At this stage, the cloud-free hurricane eye typically forms because rapidly sinking air at the center dries and warms the area. The eye at a hurricane's center is a relatively calm, clear area approximately 30-60 km across. The eyewall, surrounding the eye, is composed of dense clouds that contain the highest winds in the storm. The Saffir-Simpson Hurricane Scale defines hurricane strength by categories. A category 1 storm is the weakest hurricane (winds 120-150 km/h); a category 5 hurricane is the strongest (winds greater than 250 km/h) (Hurricane basics, 1999).

The example of satellite image of hurricane is shown in Figure 1B. This image was obtained for the hurricane of category 5 *Willa* which occurred along the Mexican coast from 20 to 24 October 2018. The peak intensity of hurricane *Willa* was estimated equal to 260 km/h; it had relatively small eye diameter of 8-16 km. The minimum pressure was recorded as 925 mb (Brennan, 2018).

Direct measurements of tropical storm and hurricane dimensions and wind speed are taken primarily by reconnaissance aircraft, although ships and buoys also take important measurements. Once a hurricane is near and/or on land, Automated Surface Observation Systems (ASOS) provide surface conditions, and radio sondes take upper air measurements. Indirect observational methods include satellite imagery and Doppler radar. In particular, satellites have greatly improved our ability to monitor and understand hurricanes. Radar data are important once the storm comes close to shore and after landfall for forecasting hurricane-related weather (Rauber *et al.*, 2012).

The wind and products of snowfalls and rainfalls touching the ground generate the seismic signals (Diaz *et al.*, 2014; Dean, 2017). The spectrum of ambient seismic noise showed strong signals associated with tropical cyclones. Through the analysis of more than a decade of seismic data recorded at several stations located in and adjacent to the northwest Pacific Ocean, Gualtieri *et al.* (2018) showed the existence of persistent and frequency-dependent signatures of tropical cyclones in ambient seismic noise depending on characteristics of the storm and on the detailed location of the station relative to the storm. Fan *et al.* (2019) found that during large hurricanes the interaction of long-period ocean waves with shallow seafloor features, located near the edge of continental shelves, excites coherent transcontinental Rayleigh wave packets in the 20- to 50-s period band. Such interactions produce seismic sources, so called "storm-quakes", with equivalent earthquake magnitudes that can be greater than 3.5.

One of the first identification of hurricane was performed via microseisms by Ebeling and Stein (2011). They showed that the August 1992 category 5 hurricane *Andrew* was detected using

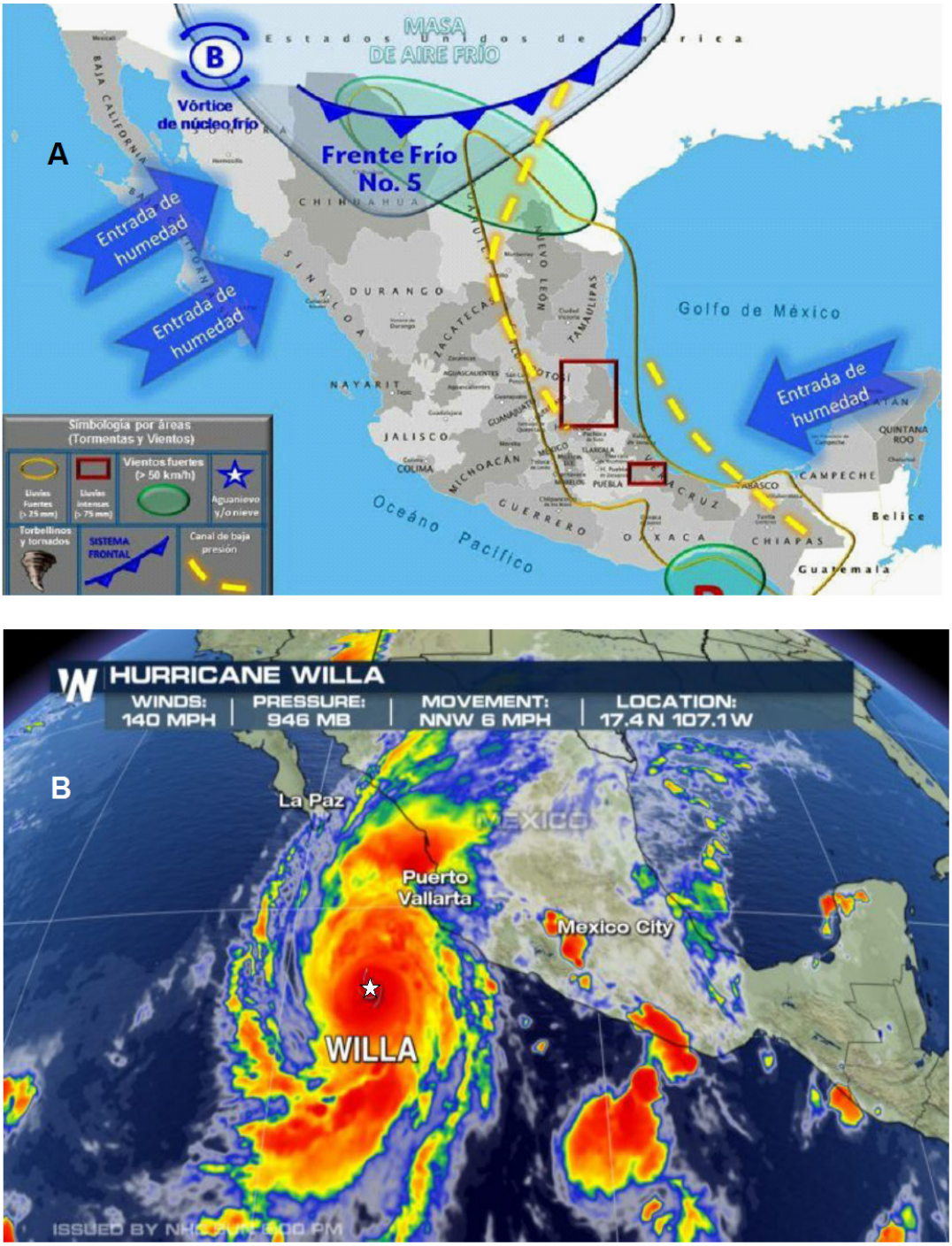

Figure 1. Examples of atmospheric disturbances occurring above the northwest Pacific coast of México. A, Scheme of the generation of the Cold front No 5 (3-4 November 2016) prepared by CONAGUA. There are shown the relative movement of the cold Polar air mass (Masa de aire frio) and of the Pacific maritime tropical masses (Entrada de humidad). Surface trough of low pressure (Canal de baja presión) is shown with a dashed line. The image was taken from *http://agendasanluis.com*, 3 November 2016. B, Satellite image of hurricane *Willa* of category 5 that was acting from 20 to 24 October 2018. Shown is the hurricane at peak intensity on 22 October. In the center is seen the eye of hurricane (shown with a star). The image was taken from *http://stlucianewsonline.com*, October 22, 2018.

microseisms recorded at the Harvard, Massachusetts, analog seismic station. The storm interacted with sea and was at a distance of about 2000 km from the station. *Andrew* continued to generate microseisms for a long time before it made its final landfall according to the position of the eye. Based on these results, there was adopted a normalized microseism pseudo power amplitude in the 200 to 143 mHz passband to identify and characterize a seismically identified hurricane.

Monitoring of a cyclone tracks ("cyclone" is named as "typhoon" in the northwestern Pacific Ocean) using the seismic waveforms recorded on the seafloor and on the land was studied by Chi *et al.* (2010). Using the waveforms, collected by land and ocean bottom seismic stations, equipped with Guralp CMG-3TC broadband three-component seismometers, which were very close to the path of typhoon *Shanshan*, they have documented at least two source regions: one trailing after the typhoon and another near the coast at shallow water depth.

The studies of excitation of seismic waves by atmospheric pressure changes during two tropical cyclones, tropical storm *Lee* (2011) and hurricane *Isaac* (2012), were performed basing on the low-frequency seismic signals in the range of 0.01 and 0.02 Hz (Tanimoto and Valovcin, 2015; 2016). They used the seismic and barometric data from the Earthscope network. The cyclones moved through this network after their landfalls. Seismic and surface pressure amplitudes showed a systematic decreasing trend with distance from the center of the hurricane. The decreasing rate was much higher for seismic waves than for pressure.

The time fluctuations of the surface pressure under the eyewall, surrounding the eye, which were reconstructed from seismic data, allowed to obtain some results about the behaviors of hurricane *Isaac* (Tanimoto and Lamontagne, 2014). At the time of the landfall, the eyewall was located at a distance of about 75 km from the hurricane center during approximately 10 hrs after the landfall. In the following 24 hrs, the eyewall moved outward from the center of the hurricane to a distance of about 200–300 km. At the end of this period (34 h after the landfall), the raw seismic data did not show any systematic, eyewall-like signature. Therefore, the lifetime of the air circulation for hurricane *Isaac* was about 1.5 days.

The studies of snowfalls dynamics derived from seismic signals are not widely developed. Practically, they are limited by the studies of the snow avalanches. Heavy snowfall leading to snow accumulation on slopes is one of the basic requirements for the occurrence of an avalanche. An avalanche is basically a moving mass of snow that slides down mountain slopes under the force of gravity and buries all that comes in its path. The main subject of seismic "snow" studies are represented by detection of snow avalanches and estimation of avalanche development and frontal velocities by seismic monitoring systems (Heck *et al.*, 2019; Surinach *et al.*, 2020).

In this article a methodology monitoring of atmospheric disturbances, based on analysis of short-period seismic signals, is developed. Two events are selected for this analysis: hurricane *Dora* and its preceding tropical storm (June 2017) and the cold front system number 25 (January 2018). For each event the following study was performed. At first, the general description of development of atmospheric event based on satellite observations is presented. Then the description of the waveforms of seismic signatures of the tracks of the atmospheric event and their Fourier spectral characteristics is done. Finally, the reconstruction of dynamics of the tracks of the atmospheric event based on the power spectral densities of the one-hour seismic records is realized. The following results are discussed from the point of view of specific generation of the seismic signals in the cases of rainfalls and snowfalls.

2. The system of seismic monitoring of atmospheric disturbances and the methodology of analysis

The summits of mountains with heights exceeding 3,000-3,500 m may serve as the best site for recording the drops of rain and snow emitted during atmospheric disturbances. In our case, the summit of dormant volcano Nevado de Colima (4,260 m), situated in Jalisco state, México at a distance of about 70 km from the Pacific Ocean coast, was selected (Figure 2A). The summit of dormant volcano, having low level of ambient seismic noise, is a good site for recording of the fall of products of atmospheric disturbances. As is shown in the photo (Figure 2B) of dormant Nevado de Colima and the neighboring active Volcán de Colima (3,860 m), the track of cold front left its snow trace on the dormant volcano but no snow on the summit of active volcano is seen.

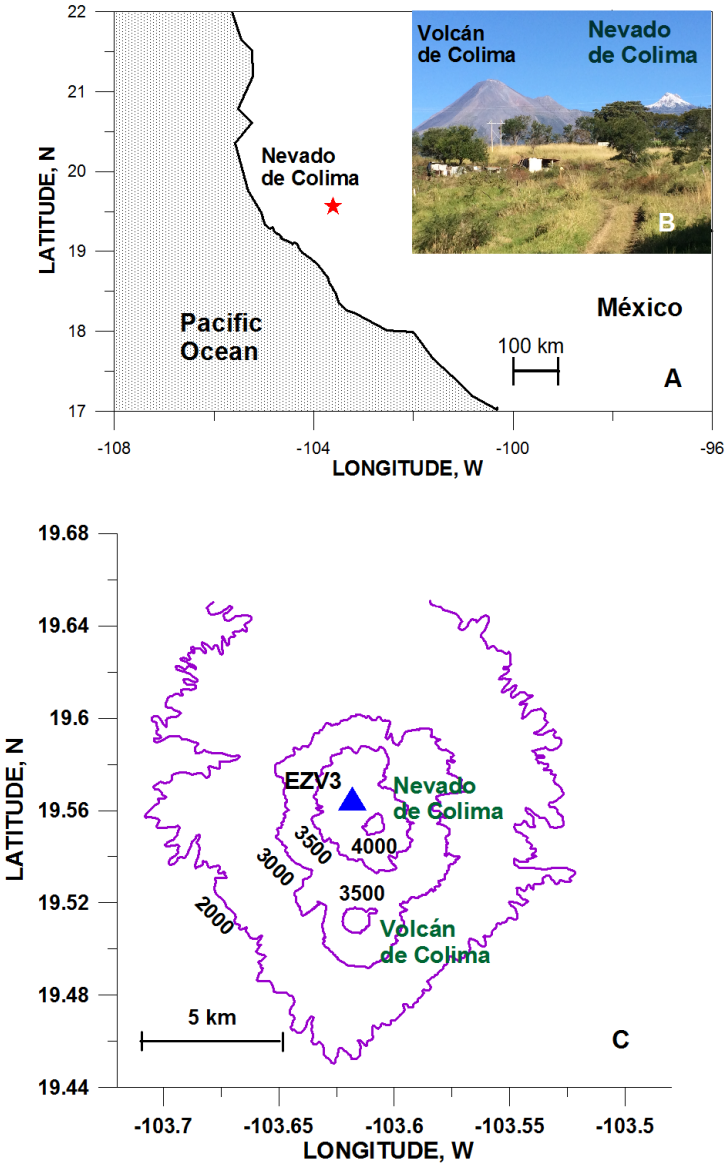

Figure 2. Position of the dormant volcano Nevado de Colima on the western coast of Mexico (A) and within the Colima Volcanic Complex together with the active Volcán de Colima (C). In B is shown the photo of both volcanoes taken on 8 February 2020 after the pass of the cold front 38. The seismic station EZV3 is shown as triangle. Photo was taken by author.

The seismic station EZV3, belonging to the seismic network of Colima University RESCO, was installed at the altitude of 3,957 m on the slope of summit of volcano (Figure 2C). The seismic signals were recorded by the short-period (T = 1.0 s) vertical-component analog sensor KINEMETRICS RANGER SS1. This sensor was placed inside the booth located on the ground surface.

The seismic signals, generated by the action of atmospheric disturbances, were studied analyzing their waveforms and their Fourier spectral characteristics. The entering of atmospheric disturbances in a zone of sensitivity of a seismic station and the total period of their activity are good seen on the daily helicorder displays of seismic records (it may be seen later in Figs. 6 and 13). These records represented a sequence of seismic signals of different amplitude and spectral parameters. In our study, one-hour seismograms (Figure 3) were taken in analysis using interactive MATLAB software *Seismo_volcanalysis* of Lesage (2009). These one-hour records were used for two purposes. At first, for study of the temporal development of atmospheric disturbances. For this purpose, the periodogram power spectral densities of each one-hour records, as is shown in Figure 3, were calculated using a Hanning window. Secondly, there was performed a selection of individual good-written waveforms of seismic signals occurring within every one-hour period of activity. The selected signals were saved separately and processed then with the program DEGTRA (https://degtra-a4-xp.updatestar.com/es). This processing step involved analyzing waveforms of characteristic individual seismic signals and calculation of their Fourier spectra.

In search for information about hurricanes in México, the Reports of National Hurricane Center (https://www.nhc.noaa.gov/) were used; in search for information about the snowfalls in México, the Reportes de Clima en México (https://smn.conagua.gob.mx/es/reporte-del-clima-en-mexico) were used.

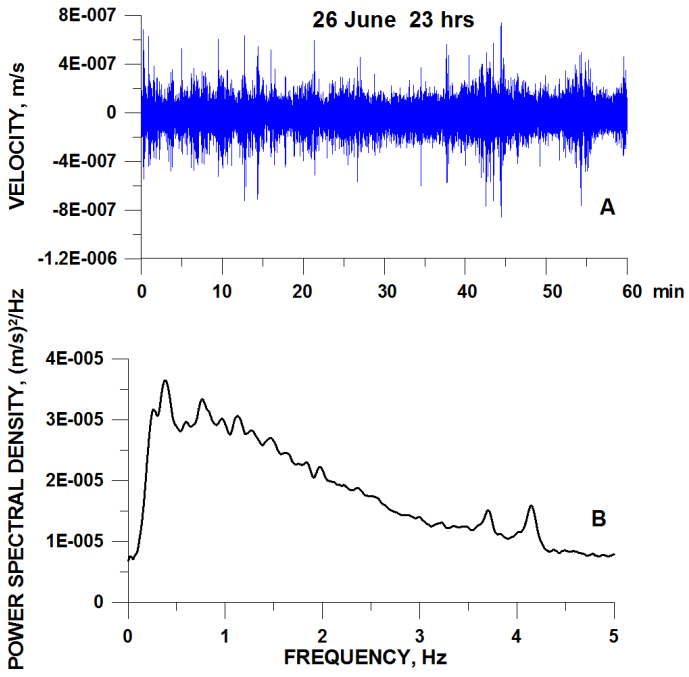

Figure 3. Example of the one-hour plot of seismic signals (short-period unfiltered seismic velocity waveforms, station EZV3) and their spectrum representing the periodogram power spectral densities vs frequency calculated using a Hanning window.

3. Description of the atmospheric events and their seismic signatures during the hurricane *Dora*

3.1. General description of development of hurricane *Dora*

Hurricane *Dora* (Figure 4A) developed from the combination of a large Central American gyre that formed around 15 June 2017 and a tropical wave that moved into the Pacific area of northwestern México by 23 June. *Dora* moved west-northwestward parallel to the coast of Mexico (Figure 4B) for about five days while located to the south of a mid-tropospheric ridge which extended from northern Mexico westward over the adjacent Pacific waters. *Dora* developed from a tropical depression, formed by 18:00 UTC (UTC- Coordinated Universal Time in June = CDT-Central Daylight Time +5 h) on 24 June, to a tropical storm by 06:00 UTC 25 June. Beginning from 18:00 UTC 26 June *Dora* became a hurricane of category 2 situated about 280 km south of Manzanillo, Mexico (See Figure 4B). The intensity of hurricane steadily decreased on 27 June (Berg, 2017).

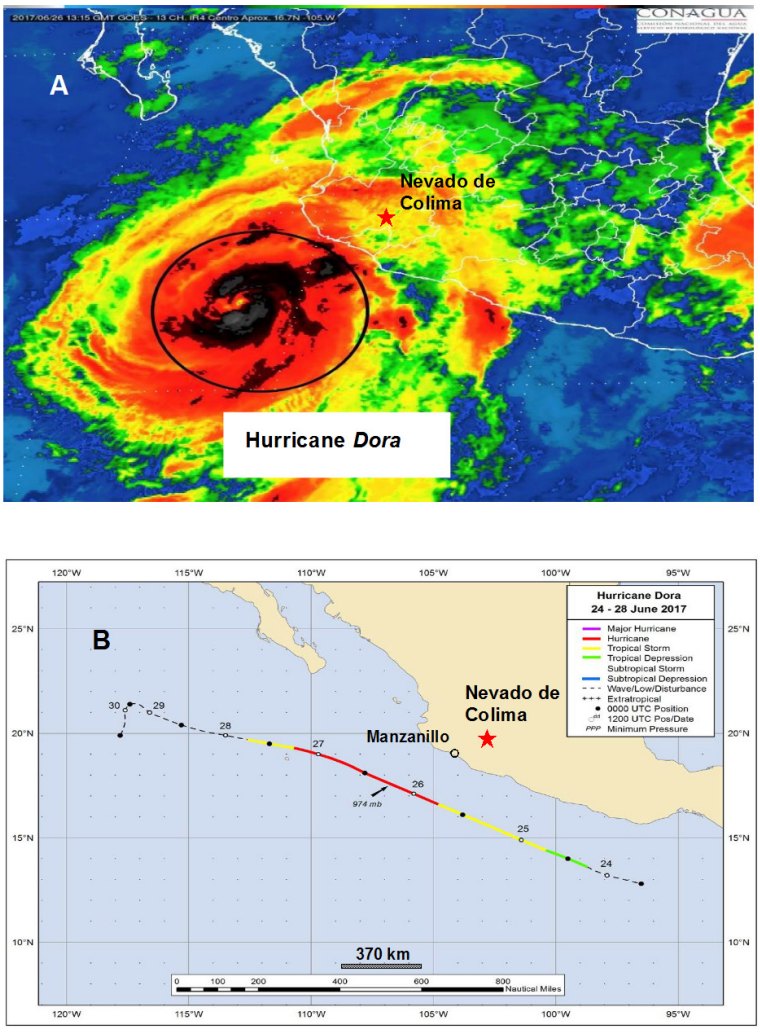

Figure 4. Satellite image of hurricane *Dora* (A) and its way along the Mexican coast (B). The satellite image was taken by the NOAA GOES-13 on 26 June 2017 at 13:15 UTC and presented by CONAGUA, Mexico (Huracán Dora, 2017). A circle in A mark the position of the eye of hurricane. Position of the dormant volcano of Nevado de Colima in A and B is shown with a star. The track positions for hurricane *Dora*, 24-28 June 2017, shown in B, are taken from (Berg, 2017).

Figure 5 demonstrates the variations in atmospheric pressure and the wind speed during development of the hurricane (based on the measurements presented in Berg, 2017). It is seen that the tropical storm occurred in conditions of decrease in atmospheric pressure from 1005 to 999 mb and increase of wind speed from 65 to 102 km/h while the hurricane was formed in conditions of atmospheric pressure varied as 999-974-990 mb and the wind speed ranging within 120-167-120 km/h.

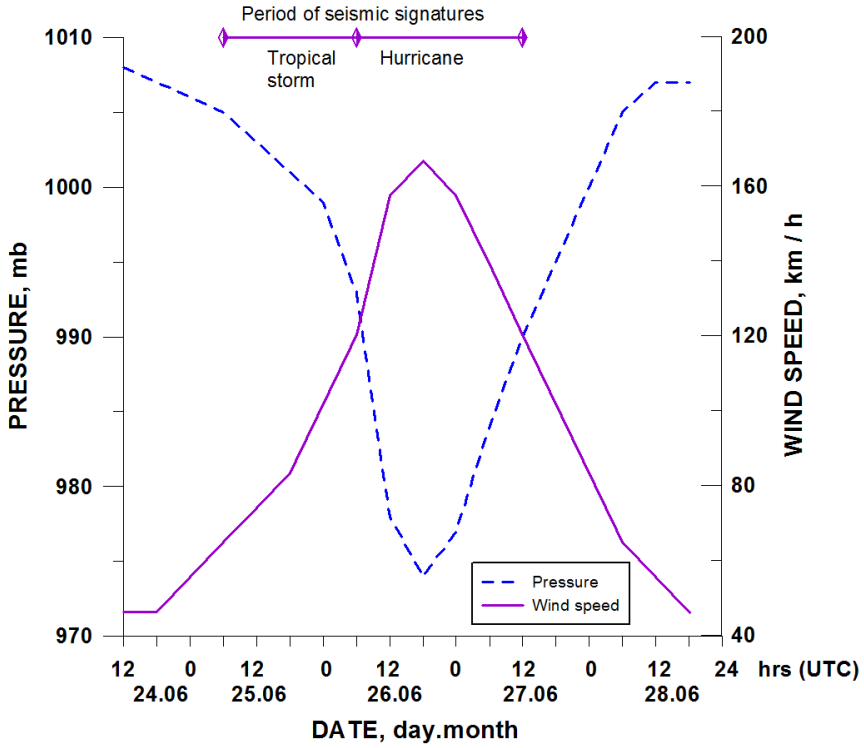

Figure 5. Variations in wind speed and atmospheric pressure during development of hurricane *Dora*. Data for this figure were taken from the measurements performed by the Cooperative Institute for Meteorological Satellite Studies/ University of Wisconsin-Madison and published in (Berg, 2017). Period of appearance of seismic signatures of the atmospheric disturbances is shown above the diagrams.

3.2. Seismic signatures of the tracks of the tropical storm and hurricane *Dora*

The sequences of seismic signals of footprints of atmospheric disturbances, recorded on the station EZV3, situated on the summit of dormant volcano Nevado de Colima, began to appear on seismograms (Figure 6) at 8 hrs (hereafter UTC) on 25 June, two hours later the generation of tropical storm from the tropical depression (Berg, 2017). The continuous seismic activity was observed until 14 hrs.

Figure 7A shows three typical signals, generated by rainfalls of tropical storm. They represent emergent phaseless waveforms having durations between 7 and 10 s. Their Fourier spectral peak amplitudes within the frequency range of 1.5-1.6 Hz varied from 1.8×10^{-7} to 2.5×10^{-7} m (Figure 7B). During the storm, the signals of this type appeared as the single events or in the dense sequences (See Figure 6).

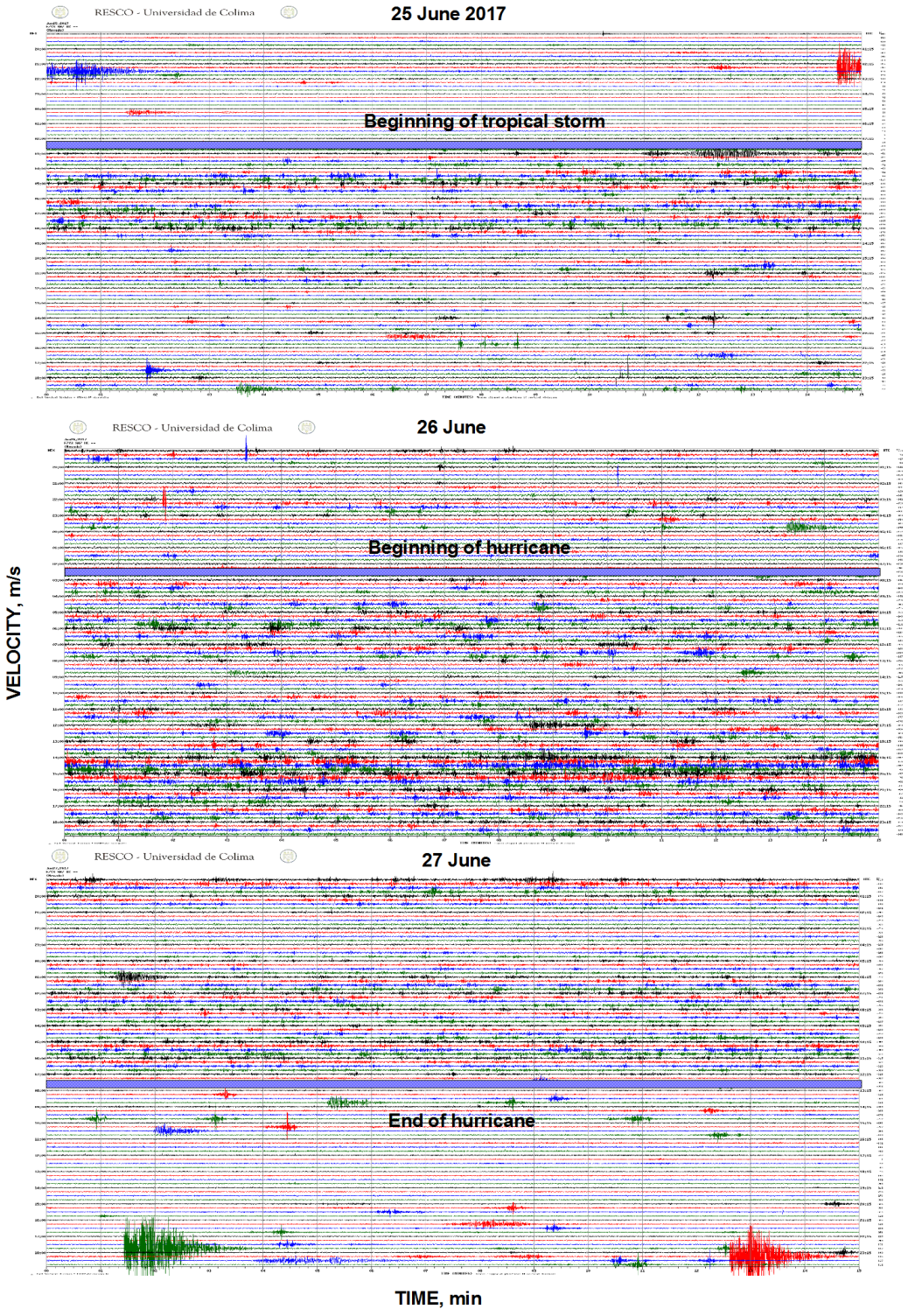

Figure 6. The daily helicorder displays of seismic signals (velocity, vertical component) recorded at short-period station EZV3, installed at the summit of the dormant volcano Nevado de Colima, are shown for 25, 26 and 27 June of 2017. There are indicated the moments of recording of vibrations generated with the arrivals of the tropical storm, of hurricane *Dora*, and the end of hurricane *Dora*. In the right side of seismograms is shown the UTC time; in the left side, local time CDT.

The stage of hurricane, which began after a short quiescence, was characterized with the dense sequences of the seismic signals. They filled the helicorder display from 7 hrs of 26 June to 12 hrs of 27 June. Among them may be indicated two groups of characteristic waveforms. The signals of the first group, shown in Figure 8A, differed from the signals, appearing during the tropical storm (Figure 7A), by their longer durations (24-30 s). Fourier spectra were characterized by a presence of dominant frequencies in the range of 1.1-1.5 Hz. The spectral peak amplitudes were slightly higher (between 3.6×10^{-7} and 5.9×10^{-7} m) than those observed for the tropical storm events (Figure 8B).

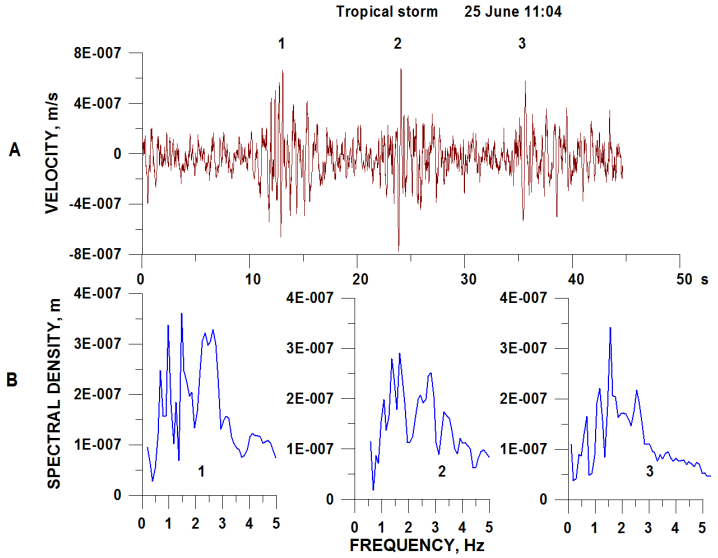

Figure 7. The short-period unfiltered seismic velocity waveforms, station EZV3 (A) and Fourier spectra of seismic signals (B) recorded during the action of the tropical storm on 25 June. 1, 2, and 3 indicate three seismic waveforms and their corresponding spectra.

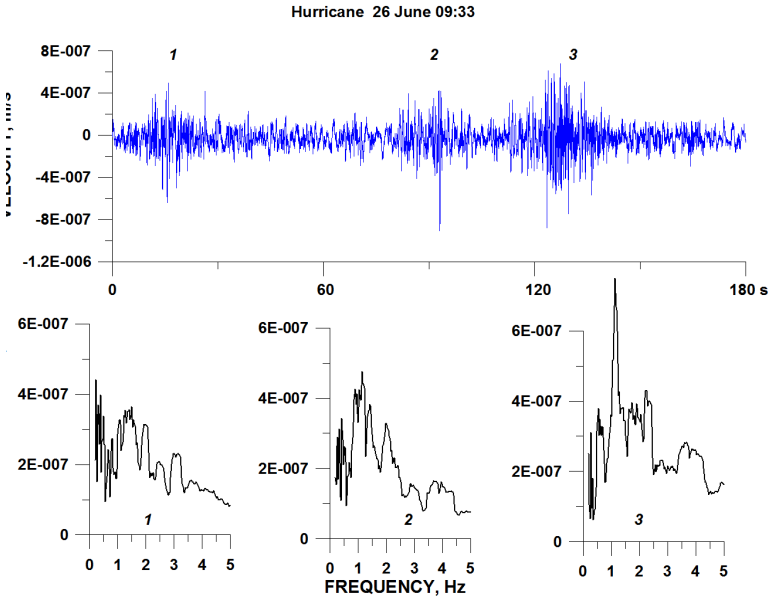

Figure 8. The short-period unfiltered seismic velocity waveforms, station EZV3 (A) and Fourier spectra of seismic signals (B) recorded during the action of the hurricane on 26 June. 1, 2, and 3 indicate three seismic waveforms and their corresponding spectra.

The signals of the second group more reflected the increased intensity of the atmospheric disturbances during the hurricane and might be produced by the storm whirlwinds (Figure 9). A part of these signals represented the sequences of long, spasmodic, high-amplitude waveforms (Figure 9A). The duration of the record, shown in Figure 9A, reached 90 s, the spectral amplitude was of $1x10^{-6}$ m, the peak frequency was of 1.4 Hz (Figure 9C). The next type of waveforms (Figure 9B) represented an individual impulsive signal of high amplitude ($5.4 x10^{-7}$ m) and of relatively long duration (17 s). Its peak spectral frequency was of 1.7 Hz (Figure 9C).

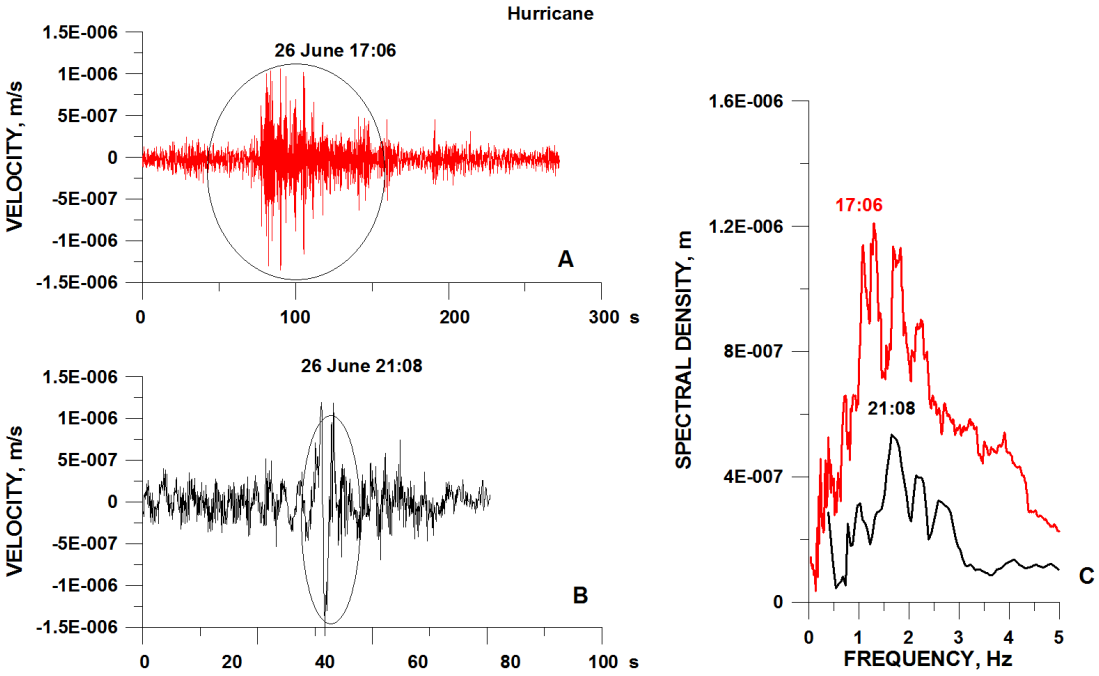

Figure 9. The short-period unfiltered seismic velocity waveforms, station EZV3 and Fourier spectra of seismic signals of large events recorded during the action of the hurricane on 25 June. A, characteristic waveform of a long sequence of events; B, the event of large amplitude; C, their Fourier spectra.

3.3. Reconstruction of dynamics of the tracks of tropical storm and hurricane *Dora*

The continuous record of the seismic signals during the tracks of tropical storm and hurricane *Dora* gave a possibility to reconstruct dynamics of the tracks of atmospheric disturbances. The power spectral densities (PSD hereafter) of one-hour seismic records were calculated (See Figure 3). Figure 10 demonstrates the temporal variations of the PSD amplitudes and corresponding frequencies of recorded one-hour waveforms during 25 to 27 June. They allow to specify our estimations of the dynamics of the tracks of tropical storm and hurricane *Dora* based on seismograms shown in Figure 6.

The variations in spectral amplitudes (Figure 10A) demonstrated the development of intensity of the process. The tropical storm began to appear at Nevado de Colima at 8 hrs of 25 June and reached its maximum activity during the period between 10 and 14 hrs. Then the activity of the storm decreased and reached its minimum at 19 hrs. After this moment, the storm began to develop into hurricane during 8 hrs. At 4 hrs of 26 June, the tropical storm turned into a hurricane. It had a stable development until 15 hrs. During the time interval between 16 and 20 hrs of 26 June, coinciding

with the maximum wind speed (See Figure 5), the hurricane reached its maximum intensity. Then its intensity steadily dropped and at 12° hrs of 27 June the hurricane completely wasted its power. As a result, the duration of the tropical storm may be estimated equal to 20 hrs and of hurricane, to 32 hrs.

The variations in frequency content of the seismic signals (Figure 10B) add some details in description of these atmospheric disturbances. At first, the signals, generated by the entrance of the tropical storm, were characterized by increase in frequencies from 0.2-03 Hz to 0.8-1.0 Hz. Then, with decrease of the tropical storm intensity and its development into hurricane, the signals of lower frequencies were formed. These low-frequency signals (0.3-0.4 Hz) were observed practically during the total period of the hurricane activity. The only moment of a sharp increase of frequency up to 1.2 Hz was observed when the wind speed reached its maximum (See Figure 5).

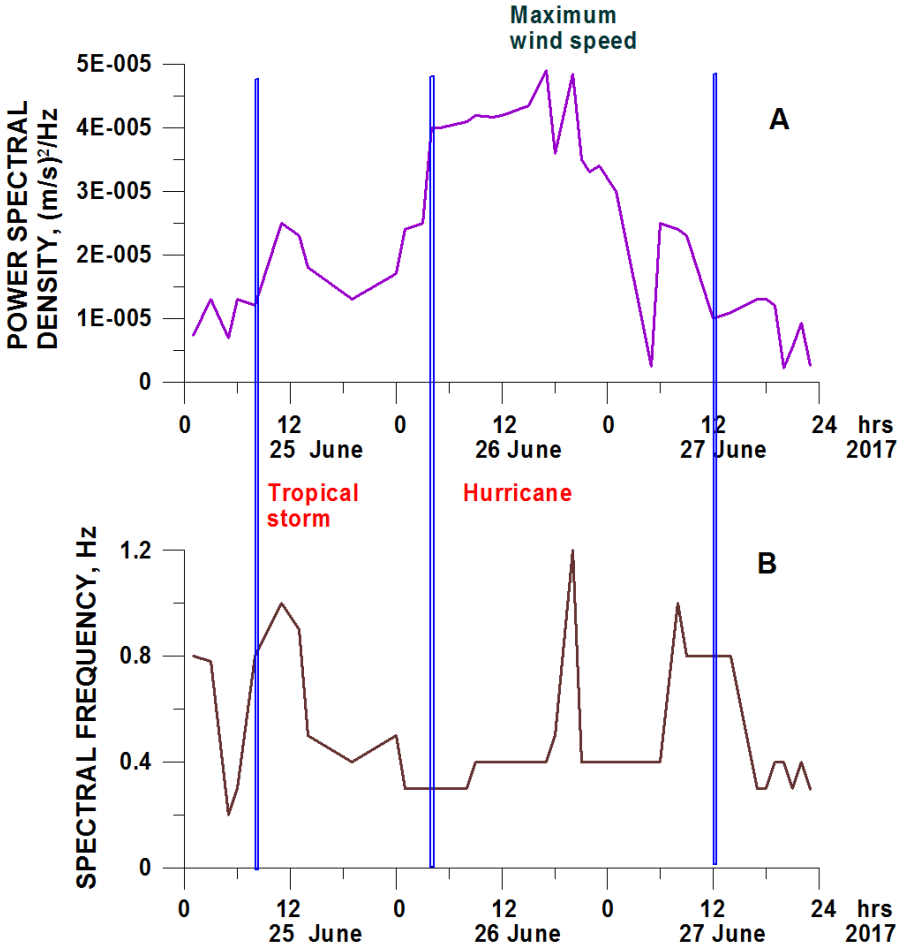

Figure 10. The development of tropical storm and hurricane during 25 to 27 June in variations of amplitudes of power spectral density (A) and corresponding frequencies (B) of one-hour seismic sequences. Vertical lines separate the stages of development.

Figure 11 demonstrates the existence of tendencies of direct relationship between the one-hour PSD of the seismic signals, generated by the tropical storm and following hurricane, and the wind speed and an inverse relationship between the one-hour PSD and atmospheric pressure. The values of atmospheric pressure and the wind speed, calculated for every 6 hours of the atmospheric disturbances, were taken from (Berg, 2017). Coefficients of correlations between these parameters

are within 0.73-0.76 that is significant at 95% confident level. Therefore, the maximum intensity of seismic signals recorded during hurricane tracks was observed at maximum wind speed and lowest atmospheric pressure.

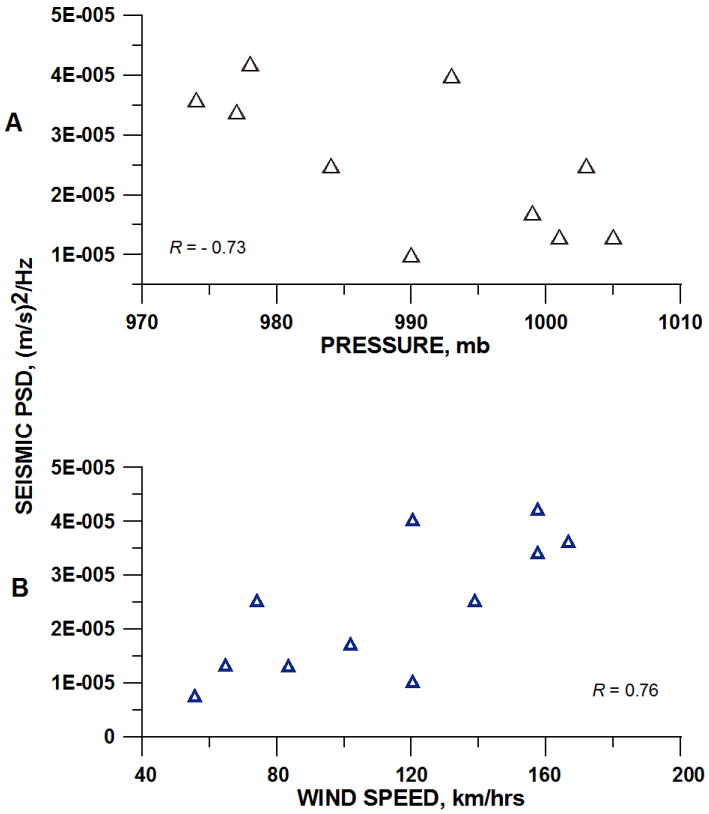

Figure 11. The plot of amplitudes of power spectral densities of one-hour seismic records vs atmospheric pressure (A) and wind speed (B). The values of atmospheric pressure and the wind speed were taken from (Berg, 2017).

4. Description of the atmospheric events and their seismic signatures during the tracks of the cold front No. 25

4.1. General description of development of the cold front No. 25

The system of cold front No. 25 was formed on 27 January 2018 (Figure 12A) and developed in México until 1 February (Reporte, 2018). According to CONAGUA (Comisión Nacional del Água de México), the continental polar air masses started at the United States, and in combination with the strong propagation of humid winds, generated by the southeastern warm Pacific Ocean tropical air masses, produced a significant drop in temperature in a large part of México. On 30 January (Figure 12B), the tropical air masses intersected the cold front distributed along the Mexican territory. On 31 January (Figure 12C), there were observed very strong to intense storms with squalls and hailstorms in the east and southeast of the territory. The intense snowfalls were recorded in the heights above 3000 m including the summit of volcano of Nevado de Colima. According to low temperatures and heavy snowfall, the entrance to the National Park of Nevado de Colima was closed by the Government of Jalisco State during 31 January (El Diario, 2018). Then the cold front began to move to the Gulf of Mexico and lost its activity on 1 February (Figure 12D).

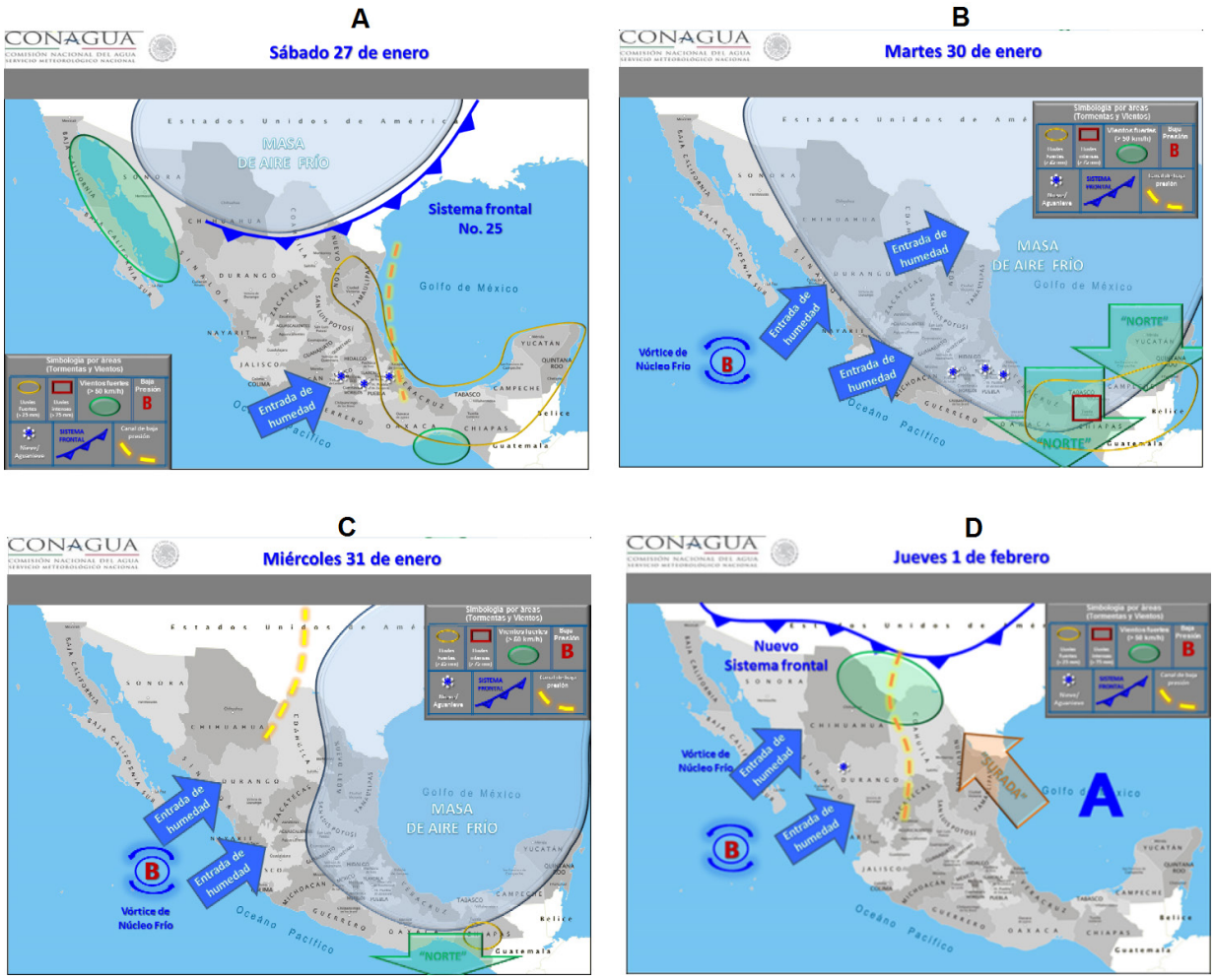

Figure 12. The development of the cold front (sistema frontal) No 25 presented on the satellite images according to CONAGUA (Comisión Nacional del Água de México). A, Entrance of the system of cold front No. 25 on the territory of México on 27 January 2018. B and C, tracks of the cold front during 30 and 31 of January above México. D, Withdrawal of the cold front to the Gulf of México on 1 February. In the map images are used the Spanish terms: masa de aire frio (cold air mass), entrada de humidad (humility entrance), vórtice de nucleo frio (cold core vortex) and nuevo sistema frontal (new frontal system). The images represent the courtesy of CONAGUA.

4.2. SEISMIC SIGNATURES OF THE TRACKS OF THE COLD FRONT NO 25

The seismic signals of atmospheric disturbances recorded on the station EZV3, situated on the summit of dormant volcano Nevado de Colima, began to appear on 30 January with the intersection of the tropical air masses and the cold front No 25 and continued until 1 February. Figure 13 demonstrates the daily helicorders of seismic signals recorded during 30 and 31 January. The appearance of seismic signals occurred due to active rainstorms, hailstorms and snowfalls occurring in this region.

It is possible to identify two stages in the development of the seismic activity generated by the cold front tracks. The arrival of the cold front was marked by the sequence of seismic signals which began to appear between 17 and 18 hrs UTC (UTC in January = CST-Central Standard Time +6 h) on 30 January. This stage I in seismic activity continued until 6 hrs of 31 January when the amplitudes

of seismic signals and the density of their appearance sharply increased indicating the beginning of the stage II (Figure 13). The stage II of intense seismic signals continued until 21 hrs of 31 January. Then the amplitudes of seismic signals decreased.

The seismic waveforms, recorded during stage I, were represented by individual events distributed with intervals from some seconds to some minutes. Their spectral frequencies varied between 1.2 and 2.0 Hz, the durations were within the interval of 10-30 s. The spectral amplitudes varied from $3x10^{-7}$ to $6x10^{-7}$ m. Three typical signals, shown in Figure 14, are characterized by the durations of these events between 25 and 30 s, their spectral amplitudes were of $(3\text{-}5)x10^{-7}$ m and the spectral frequencies varied between 1.2 and 1.5 Hz.

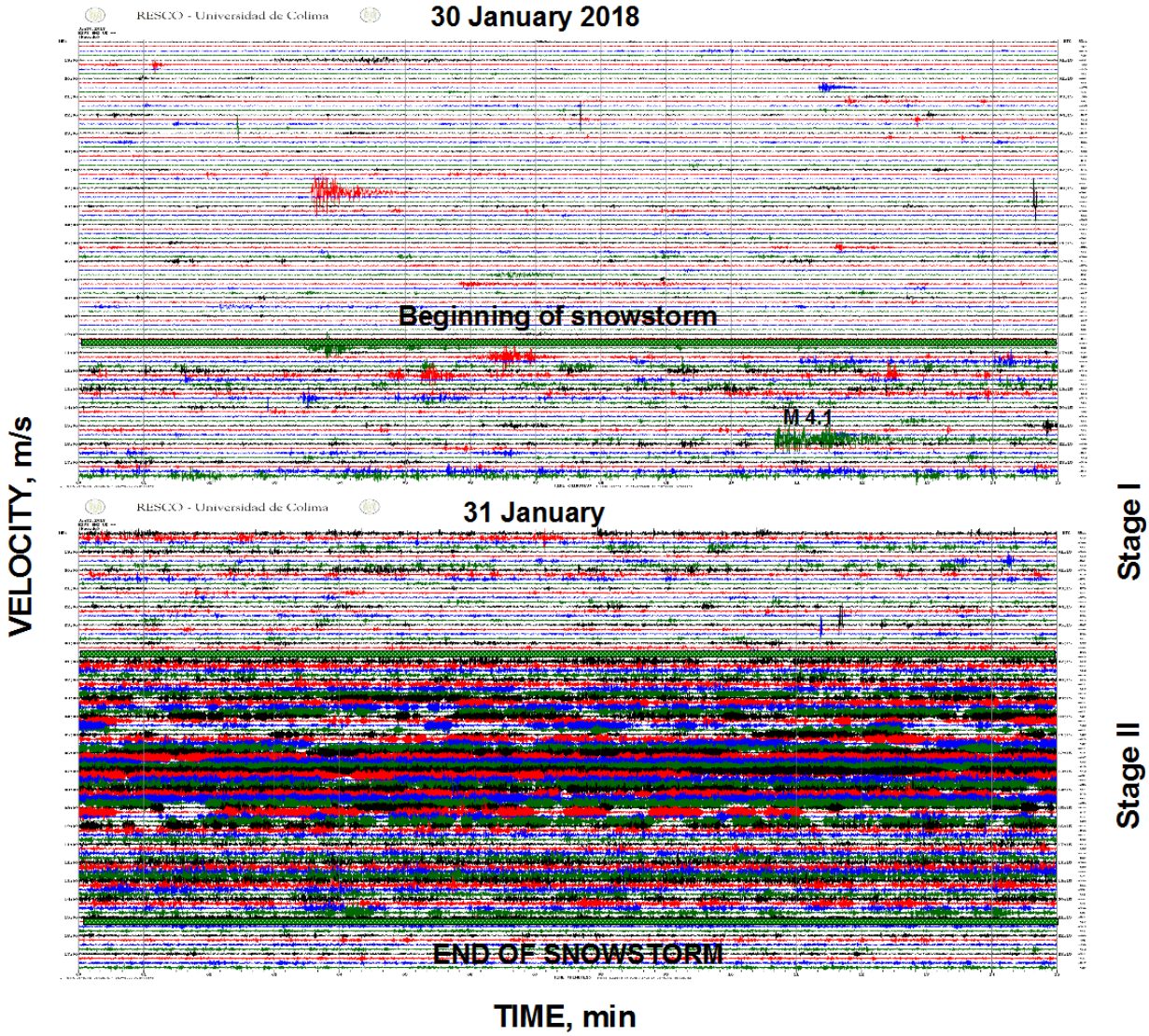

Figure 13. The daily helicorder displays of seismic signals (velocity, vertical component) recorded at short-period station EZV3, installed at the summit of the dormant volcano Nevado de Colima, are shown for 30 and 31 January 2018. There are indicated the moments of recording of vibrations generated with the arrivals of two stages of the tracks of the cold front No 25. In the right side of seismograms is shown the UTC time; in the left side, local time CST.

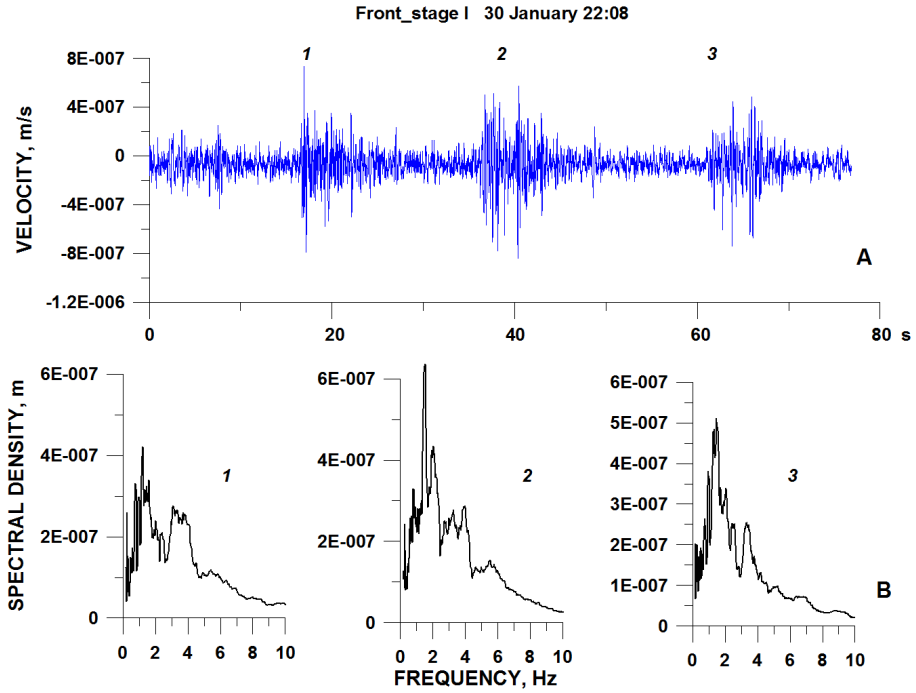

Figure 14. The short-period unfiltered seismic velocity waveforms, station EZV3 (A) and Fourier spectra of seismic signals (B) recorded during the action of the initial stage I of the tracks of cold front on 30 January 2018. 1, 2, and 3 indicate three seismic waveforms and their corresponding spectra.

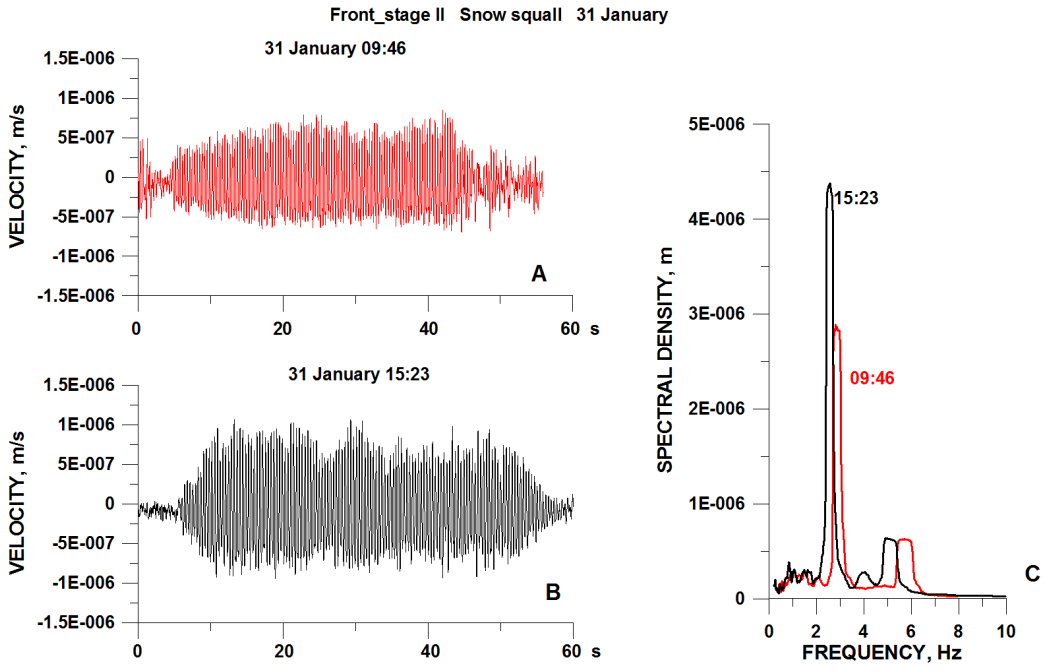

Figure 15. The short-period unfiltered seismic velocity waveforms, station EZV3 (A, B) and Fourier spectra of the long seismic signals (C) recorded during the action of the squall stage II of the tracks of cold front on 31 January 2018.

During the stage II, beginning at about 6 hrs UTC of 31 January (30 January, 23 hrs GST, in the night with decreasing of temperature), the character of waveforms of seismic signals significantly changed (Figure 13). The seismic waveforms were recorded in the dense groups of signals. They differed from the waveforms of the initial stage in their shape and spectral content, representing the harmonic vibrations (Figure 15 and 16).

Part of the signals was rather long, reaching durations of 50-70 s (Figure 15). These waveforms were characterized by two fundamental frequencies of between 2.6 and 2.9 Hz and between 5 and 6 Hz. The spectral amplitudes, corresponding to the first fundamental frequencies, varied between $2x10^{-6}$ and $4x10^{-6}$ m.

The characteristic short single events are shown in Figure 16. Their durations varied between 10 and 15 s. The arrivals were emergent as for long signals. They were characterized by two fundamental frequencies of similar range of fundamental spectral frequencies as for long waveforms (2.7-2.8 Hz and 5.4-5.5 Hz). Their spectral amplitudes, corresponding to the first fundamental frequencies, varied between $1.5x10^{-6}$ m and $2x10^{-6}$ m.

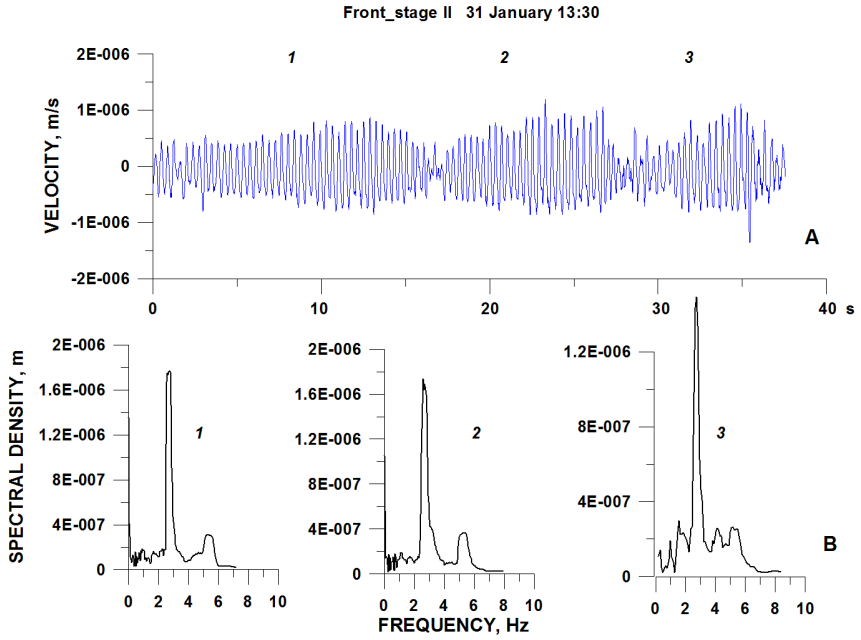

Figure 16. The short-period unfiltered seismic velocity waveforms, station EZV3 (A) and Fourier spectra of seismic signals (B) recorded during the action of the squall stage II of the tracks of cold front on 31 January 2018. 1, 2, and 3 indicate three seismic waveforms and their corresponding spectra.

4.3. Reconstruction of dynamics of the tracks of the cold front No 25

As was noted in the case of hurricane *Dora* (Section 3.3), the continuous record of the seismic signals during the tracks of atmospheric disturbances gives a possibility to reconstruct their dynamics basing on the spectral characteristics of one-hour seismic records. Figure 17 demonstrates the temporal variations of spectral amplitudes and frequencies of recorded one-hour waveforms generated by the cold front No 25 during 30 and 31 January.

The amplitude and frequency variations, shown in Figure 17, confirm a presence of two stages, pre-squall and squall, in development of the tracks of the cold front, indicated in Figure 13. The first stage, pre-squall, begins at 18 hrs on 30 January. The appearance of the cold front events was marked by an increase in the spectral frequency of the one-hour waveforms from 0.6-08 Hz to 1.0-1.5 Hz. The spectral amplitudes also increased but slightly. The stage II, squall, began on 5 hrs of 31 January with a significant change in both spectral content and spectral amplitudes. Seismic vibrations demonstrated a sharp increase in amplitudes, reaching their maximum between 10 and 13 hrs. The spectral frequencies became higher, reaching 2.4-3.3 Hz. With termination of the stage II at 21 hrs of 31 January, the one-hour spectral amplitudes of seismic vibrations became to be close to the background noise level. Totally, the pre-squall stage continued for 11 hrs and the squall stage, for 16 hrs.

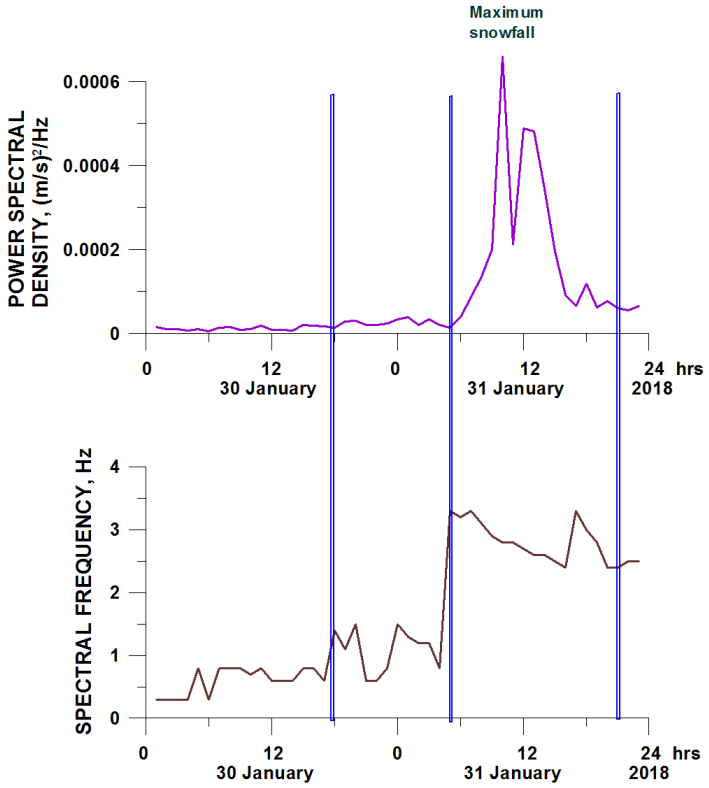

Figure 17. The development of the cold front No 25 during 30 and 31 January in variations of amplitudes of power spectral density (A) and corresponding frequencies (B) of one-hour seismic sequences. Vertical lines separate the stages of development.

5. The seismic signals recorded during the initial stages of the atmospheric disturbances

The arrivals of the tropical storm and the pre-squall stage of the cold front were marked with the seismic signals different from the following rainfall and snowfall vibrations (Figure 18). In the very beginning of the pattern of seismic signals of the tropical storm, on 25 June at 08:11, it is seen a waveform consisting of a sequence of three similar emergent, spindle-shaped seismic signals (Figure 18A, B) with frequencies of 1.3, 0.85, and 0.85 Hz, which differ in their durations (40, 90, and 50 s)

and spectral amplitudes ($0.7x10^{-6}$, $5x10^{-6}$, and $1.4x10^{-6}$ m). Each of the waveforms begins with a low-amplitude signal which gradually increases in amplitude and then slowly decreases. These are similar to the seismic records of rockfalls generated during eruption at active volcanoes (Zobin, 2017) or small debris flows (Coviello *et al.*, 2019) and may be identified as the seismic signals produced by the ground mass movement generated by a surge arriving with the tropical storm.

The arriving of cold front also generated a special type of the seismic signals. At 16:48 hrs on 30 January, in the very beginning of the seismic sequence associated with the cold front, it was recorded a 1-min duration 3-pulses waveform. This record (Figure 18C) represented a high-amplitude impulsive signal situated between two similar low-amplitude emergent waveforms. The maximum spectral amplitudes of all three pulses were observed at high frequencies, between 10 and 15 Hz (Figure 18D).

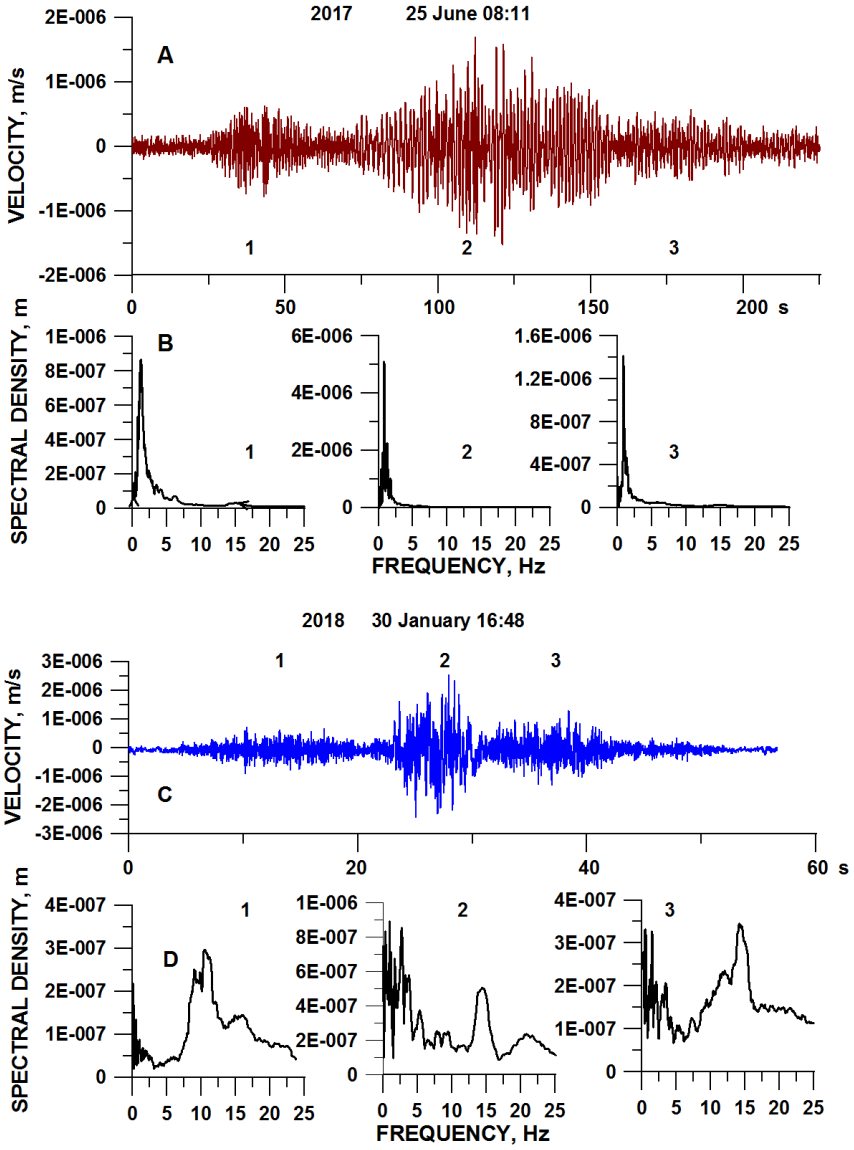

Figure 18. The short-period unfiltered seismic velocity waveforms, station EZV3 (A, C) and Fourier spectra of seismic signals (B, D) recorded during the initial entrance of the tropical storm on 25 June 2017 at 08:11 and of the cold front on 30 January 2018 at 16:48, respectively. 1, 2, and 3 indicate three seismic waveforms and their corresponding spectra.

These waveforms may represent the seismic reverberations created by the sound waves of thunders associated with lightning (Kappus and Vernon, 1991; Lin and Langston, 2009; Usoltseva, 2011). Kappus and Vernon (1991) studied the seismic signals of ground velocity recorded during 13 sequences of thunderstorms. The waveforms of thunder-induced ground velocity reverberations, presented in their article, are similar to those shown in Figure 18C. The spectra of these events were characterized by peaks at low frequency varying from 6 to 13 Hz.

5. Results and Discussion

The wind and products of snowfalls and rainfalls touching the ground generate the seismic signals. The study of seismic signatures of atmospheric processes recorded at a height of about 4 km above sea level at the summit of dormant volcano Nevado de Colima showed sensibility of the seismic sensor to the ground vibrations caused by the impact of these products of atmospheric disturbances. The following results may be formulated.

1. The seismic signals, generated by tropical storm and hurricane *Dora*, were characterized by different waveforms and spectral parameters. The maximum amplitudes of the power spectral densities of these signals corresponded to the lowest atmospheric pressure and highest wind speed.
2. The seismic signals, generated by two stages of the cold front No 25, were characterized by different waveforms and spectral parameters. While the spectral characteristics of pre-squall stage are generally similar to the same of the tropical storm and hurricane, during the stage of squall, the fundamental short-period frequencies appear.
3. Variations in the spectral peak frequencies and corresponding PSD amplitudes of the one-hour seismic signals gave a good description of development of atmospheric disturbances and allowed to estimate the lifetime of the air circulations for each stage of atmospheric disturbances: 20 hrs for tropical storm; 32 hrs for hurricane *Dora*; 11 hrs for pre-squall stage of the cold front and 16 hrs for the squall stage of the cold front.

Figure 19 summarizes the results demonstrating the mutual plot of spectral parameters of characteristic waveforms recorded during tropical storm, hurricane and two stages of the cold front activity. Here are presented nine measurements of the best readable waveforms for each type of atmospheric disturbances. It is seen that in the case of tracks of hurricane *Dora*, the stage of tropical storm was characterized by lower amplitudes of recorded seismic events comparative with the stage of hurricane. At the same time, the events recorded during the tropical storm and hurricane stages, were represented in the same range of spectral frequencies between 1.0 and 1.7 Hz.

In the case of tracks of the cold front No 25, the preliminary stage was characterized by lower amplitudes of recorded seismic events comparative with the stage of maximum activity. During the preliminary, pre-squall, stage, the events were characterized by the spectral frequencies between 1.2 and 1.9 Hz. The events of the stage of maximum, squall, activity generated the seismic signals of higher frequencies within a range from 2.6 to 3.7 Hz.

The comparison of spectral characteristics of the events of hurricane and cold front allows seeing a similarity in characteristics of the hurricane and preliminary stage of the cold front. They both may be considered as the heavy rainfalls. The significant difference in spectral characteristics of the

events occurring during the stage of maximum activity of the cold front comparing with other events associated with rain falling allows to propose that in this case the seismic signals were produced by heavy snowfall, or snow squall. The appearance of fundamental frequencies in seismic spectra of the squall events demonstrates the difference in interactions of rain-ground and snow-ground. Falling snowflake serve as a single resonator while the falling rain drop serve as a multiple resonator.

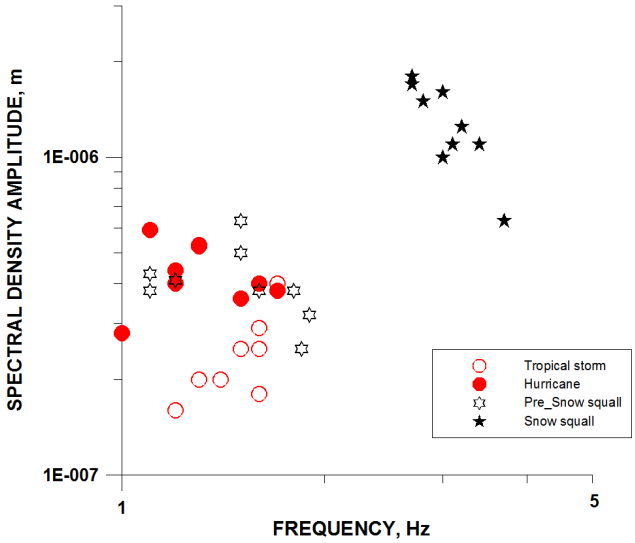

Figure 19. Plot of power spectral density vs frequency for characteristic waveforms recorded during tracks of the tropical storm and hurricane, and pre-squall and squall stages of the cold front.

6. Conclusions

The wind and products of snowfalls and rainfalls touching the ground generate seismic signals. The study of short-period seismic signatures of atmospheric disturbances during tracks of hurricane *Dora* and its preceding tropical storm (June 2017) and the cold front system number 25 (January 2018), which were recorded at a height of about 4 km above sea level at the summit of dormant volcano Nevado de Colima, allowed to develop a methodology of monitoring these atmospheric events. This study includes the indication of the seismic signatures of atmospheric disturbances on the daily helicorder displays of seismic signals with following analysis of waveforms, produced by the impact of rainfalls and snowfalls with the ground surface, and their Fourier spectral characteristics. Then, the reconstruction of the tracks of the atmospheric events, based on the power spectral densities of the one-hour seismic records, which is performed mutually with the satellite observations was performed. Application of this methodology allowed indicating the periods of actions of tropical storm, hurricane, and two stages of the cold front and estimating the characteristic waveforms for each period. Analysis of the spectral characteristics of these waveforms demonstrated that the rainfalls, occurring during the tropical storm, hurricane and the initial stage of the cold front tracks, generated the seismic signals within the frequency range between 1.0-1.8 Hz while the snowfall during the second stage of the cold front tracks generated the seismic signals within the frequency range between 2.6 and 3.7 Hz. This gives a possibility for monitoring the tracks of atmospheric disturbances in real time or reconstruction the dynamics of these events during past time.

Acknowledgements

The comments of two anonymous reviewers helped me to improve the manuscript. I thank the personnel of seismic network RESCO of Colima University and their head Rául Arámbula for providing me the seismic records of the station EZV3. I thank Cirilo Bravo Lujano (CONAGUA) for his help in acquisition of the images of development of the cold front No 25. The processing of the digital seismic signals was realized using the program DEGTRA provided by Mario Ordaz, UNAM and the Interactive MATLAB software *Seismo_volcanalysis* for the analysis of seismic volcanic signals prepared by Philippe Lesage (Lesage, 2009) and adapted by Miguel Gonzalez.

References

Berg, R. (2017). Hurricane Dora, 24 – 28 June 2017. Tropical cyclone report. National hurricane center. 12 p.

Brennan, M.J. (2018). Hurricane Willa, 20-24 October 2018. Tropical cyclone report. National hurricane center. 29 p.

Chi, W-C., Chen,W-J., Kuo, B-Y. and Dolenc, D. (2010). Seismic monitoring of western Pacific typhoons. *Mar. Geophys. Res.*, 31, 239–251. DOI 10.1007/s11001-010-9105-x

Coviello, V., Arattano, M., Comiti, F., Macconi, P., and Marchi, L. (2019). Seismic characterization of debris flows: Insights in to energy radiation and implications for warning. *J. Geophys. Res.*, Earth Surface, 124. https://doi.org/10.1029/2018JF004683

Dean, T. (2017), The seismic signature of rain. *Geophysics*, 82, 53–60.

Diaz, J., Ruiz, M., Crescentini, L., Amoruso, A., Gallart, J. (2014). Seismic noise generated by rainfall, snowmelt and floods on a Pyrenean mountain river. Abstracts, EGU General Assembly Conference.

Ebeling, C.W. and Stein, S. (2011). Seismological identification and characterization of a large hurricane. *Bull. Seismol. Soc. Am.*, 101, 399–403, http:// 10.1785/0120100175.

El Diario (2018). Cierran Parque Nacional Nevado de Colima por mal clima. *El Diario*, 31 de enero de 2018. http://www.ntrguadalajara.com/post.php?id_nota=91622

Fan, W., McGuire, J. J., de Groot-Hedlin, C. D., Hedlin, M. A. H., Coats, S., and Fiedler, J. W. (2019). Stormquakes. *Geophysical Research Letters*, 46. https://doi.org/10.1029/2019GL084217

Gualtieri, L., Camargo, S.J., Pascale, S., Pons, F.M.E. and Ekström, G. (2018). The persistent signature of tropical cyclones in ambient seismic noise. *Earth and Planetary Science Letters*, 484, 287–294

Heck,M., Hobiger, M., van Herwijnen, A., Schweizer, J., and Fah, D. (2019). Localization of seismic events produced by avalanches using multiple signal classification. *Geophys. J. Int*, 216, 201–217.

Huracán Dora (2017). Ciclones tropicales 2017. CONAGUA, 11 p.

Hurricane basics (1999). National Hurricane Center. http://www.nhc.noaa.gov.

Kappus, M.E. and Vernon, F.L. (1991). Acoustic signature of thunder from the seismic records. *J. Geophys. Res.*, 96, 10989-11006.

Lamontagne, A. (2018). Excitation of Seismic Waves by the Atmosphere: Monitoring Severe Weather with Modern Digital Seismic Data. PhD thesis, UC Santa Barbara. 190 pp.

Larose, E., Carrière, S., Voisin, C., Bottelin, P., Baillet, L., Guéguen, P., Walter, F., Jongmans, D., Guillier, B., Garambois, S., Gimbert, F., Massey, C. (2015). Environmental seismology: What can we learn on earth surface processes with ambient noise? *J. Appl. Geophys.*, 116, 62–74. doi: 10.1016/J.JAPPGEO.2015.02.001.

Lesage, P. (2009). Interactive Matlab software for the analysis of seismic volcanic signal. Computers Geosciences 35: 2137–2144.

Lin, T.-L. and Langston, C. A. (2007). Infrasound from thunder: A natural seismic source. *Geophys. Res. Lett.*, 34, L14304, doi:10.1029/2007GL030404.

Rauber, R.M., Walsh, J. and Charlevoix, D. (2012). Severe and hazardous weather: An introduction to high impact meteorology. 4th edition, 612 p. Kendall Hunt publishing company. ISBN 978-1-5249-9984-1.

Reporte (2016). Reporte de clima en México, Noviembre 2016. CONAGUA, México. 30 p.

Reporte (2018). Reporte de clima en México, Enero 2018. CONAGUA, México. 31 p.

Suriñach, E., Flores-Márquez, E.L., Roig-Lafon, P., Furdada, G., and Tapia, M. (2020). Estimation of avalanche development and frontal velocities based on the spectrogram of the seismic signals generated at the Vallée de la Sionne Test Site. *Geosciences*, 113; doi:10.3390/geosciences10030113

Tanimoto, T., and Lamontagne, A. (2014).Temporal and spatial evolution of an on-land hurricane observed by seismic data, *Geophys. Res. Lett.*, 41, 7532–7538, doi:10.1002/2014GL061934.

Tanimoto, T., and Valovcin, A. (2016). Existence of the threshold pressure for seismic excitation by atmospheric disturbances, *Geophys. Res. Lett.*, 43, 11,202–11,208, doi:10.1002/2016GL070858.

Usoltseva, O. A. (2011). Analysis of seismic record during of thunderstorm phenomena by the seismic array MHVAR (Mihnevo, Moscow region). Proc. Tula State Univ., *Natur. Sci.*, 2, 222-232 (In Russian).

Valovcin, A., and Tanimoto, T. (2017). Modeling the excitation of seismic waves by the Joplin tornado. *Geophys. Res. Letters*, 44, 10,256-10,261.

Zhang, J., P. Gerstoft, and P. D. Bromirski (2010), Pelagic and coastal sources of P-wave microseisms: Generation under tropical cyclones, *Geophys. Res. Lett.*, 37, L15301, doi:10.1029/2010GL044288.

Zobin, V.M. (2017). Introduction to Volcanic Seismology, 3d edition, Elsevier, Amsterdam-New York-Tokyo. 584 p., ISBN-13: 978-0444636317; ISBN-10: 0444636315. http://dx.doi.org/10.1016/B978-0-444-63631-7.00005-4

Original paper

https://doi.org/10.22201/igeof.00167169p.2021.60.4.2161

Coastal response to the passage of tropical cyclone Juliette on the Central Pacific Coast of Mexico

Anatoliy Filonov[1], Iryna Tereshchenko[1], Lydia B. Ladah*[2], Cesar Monzon[1], Federico Velázquez-Muñoz[1], Jorge Montes-Arechiga[1]

Received: May 6, 2021; accepted: August 31, 2021; published on-line: October 1, 2021.:

Resumen

Durante septiembre de 2001 se colectaron datos oceanográficos y meteorológicos costeros *in situ* en la costa del Pacífico tropical mexicano, cerca de Barra de Navidad, Jalisco, México, antes, durante y después del paso del huracán Juliette. El paso del huracán resultó en una profundización significativa de la termoclina, mezcla en de los 40 m superiores de la columna de agua, y un aumento en el nivel del mar de casi 50 cm en la costa, con efectos que duraron unos 5 días. Un descenso de la temperatura y un aumento de la salinidad ocurrió en aguas más someras de 20 m, con lo contrario ocurriendo a profundidades mayores de los 20 m. Aunque las respuestas en el océano abierto a los huracanes están ampliamente disponibles a partir de datos de satélite, los datos *in situ* en la columna de agua y del nivel del mar son difíciles de adquirir en zonas costeras, sin embargo, proveen información crítica para estudios de modelación. Este conjunto de datos ofrece una oportunidad única para explorar los efectos de los huracanes en esta costa.

Palabras clave: huracán, procesos costeros, aumento del nivel del mar, mareas excesivas y olas atrapadas en la costa.

Abstract

In situ coastal oceanographic and meteorological data were collected on the Mexican Tropical Pacific coast near Barra de Navidad, Jalisco, Mexico, during September 2001 from before, during and after the passing of Hurricane Juliette. The hurricane resulted in a significant deepening of the thermocline, mixing of the upper 40 m of the water column, and a rise in sea level of almost 50 cm at the coast, with effects lasting for about 5 days. A decrease in temperature and an increase in salinity occurred in the upper 20 m of the water column, with the opposite occurring below 20 m. Although analyses of open ocean responses to hurricanes are widely available from satellite data, *in situ* coastal water-column and sea-level data are difficult to acquire, yet crucial to inform modeling studies. This data set provides a rare opportunity to explore *in situ* hurricane effects on this coast.

Key words: hurricane, coastal processes, sea-level rise, over-tiding and coastally trapped waves.

**Corresponding author at lladah@cicese.mx*

[1] *University of Guadalajara, Department of Physics, Blvd. Marcelino García Barragán 1421, Guadalajara, CP 44430, Jalisco, Mexico.*

[2] *Department of Biological Oceanography, CICESE, Centro de Investigación Científica y Educación Superior de Ensenada, Carretera Ensenada-Tijuana 3918, Zona Playitas, CP 22860, Ensenada, BC, Mexico*

Introduction

The coastal impacts of hurricanes are well known, including an increase in winds in the right front quadrant, accompanying sea level surges, precipitation and compound flooding extending far inland, as well as costly ecosystem and infrastructure damage (Simpson and Riehl, 1981; Miller and Stone, 2001; Mallin and Corbett, 2006; Valle-Levison *et al.*, 2020; Reffitt *et al.*, 2020). Hurricanes can also trigger coastal upwelling and downwelling, turbulent mixing, coastally trapped waves, and near-inertial oscillations at the coast (Keen and Glenn, 1999; Dukhovskoy *et al.*, 2009; Guang-Bing *et al.*, 2017; Hughes *et al.*, 2019). These non-linear coastal processes cause feedbacks that can further modulate hurricane impacts at the coast that are difficult to model, yet *in situ* data encompassing these processes are often unavailable, especially from rural areas or in shallow waters. Recent work has shown the benefits of *in situ* coastal water-column data for hurricane model improvement, particularly with respect to non-linear baroclinic processes (Miles *et al.*, 2015; Zhang and Emanuel, 2018; Asher *et al.*, 2019; Wu *et al.*, 2020).

Hurricanes are common in Mexican waters and occur in the Mexican Pacific Ocean starting in May and in the Gulf of Mexico in June, lasting through November in both regions with a maximum in September (Jauregui, 2003), impacting areas which are internationally recognized for their fisheries, sea turtle conservation, and beach tourism importance. In the Gulf of Mexico, both models and *in situ* observations are well developed (reviewed in Levison *et al.*, 2010; Trepanier *et al.*, 2015), particularly because of the economic assets along the Gulf Coast of the USA. However, the coastal ocean in the hurricane-impacted region in the Eastern Mexican Pacific has received less attention, with more research focused on offshore, ship-based studies rather than *in situ* coastal observations (Wyrtki, 1965, 1966, 1967; Enfield and Allen, 1983; Fiedler, 1992, 2002; Badan, 1998; Kessler, 2002, 2006; Fiedler and Talley, 2006; Lavin *et al.*, 2006; Zamudio *et al.*, 2001), although this area has shown increasing coastal hurricane impacts over the last few decades (Jauregui, 2003). Understandably, because of the danger of the loss of lives and equipment, *in situ* coastal observations are often unavailable during hurricanes, however measurements of climatic and hydrodynamic conditions of the coastal zone along the Eastern Pacific during hurricanes are critical to inform models and predict hurricane impacts on sea level.

Hurricanes can cause baroclinic and barotropic trapped waves which can travel long distances without losing energy and can result in significant vertical and horizontal fluctuations in coastal sea level. The dynamics of cyclone induced wave movements in the Mexican Pacific show phase velocities of 1.5-2 m s^{-1} with scales of 500-1000 km along the coast and 100-200 km across the shelf, resulting in a 10-30 cm rise in sea level at the shore (Christensen *et al.*, 1983; Enfield and Allen, 1983; Brink, 1991; Gjevik, 1991; Gjevik and Merrifield, 1993). Coastal non-linear processes such as coastally trapped waves have been shown to modulate effects of hurricane-induced upwelling at the Mexican coast (Zamudio *et al.*, 2010).

Zamudio *et al.* (2002) presented dynamic simulations for hurricane Juliette as it moved along the Mexican Pacific Ocean, 350-400 km off the coast of mainland Mexico, showing it was a sustained Category 4 hurricane during the 2001 Pacific hurricane season. It made landfall in the state of Baja California Sur, Mexico in late September, resulting in 12 deaths and near $500 million USD in damage. In this contribution, we analyze *in situ* meteorological and oceanographic instrument measurements obtained directly on the continental shelf during the passage of hurricane Juliette off

the coast of Jalisco, Mexico, near Barra de Navidad. The results herein provide a unique opportunity to study coastal hurricane impacts on the nearshore water column on this stretch of coast.

Materials and methods

Hydrographic data were collected on the coast of Jalisco, Mexico using an SBE-16 conductivity-temperature-depth CTD (Sea Bird Electronics Inc.) deployed 8m above the bottom on a mooring near the 40 m isobath programmed to record pressure, temperature, and salinity at 5-min intervals, from September 20 to October 1, 2001. An autonomous meteorological weather station (Croweather system, Davis Instrument Corp.) was installed at 4 m above sea level, 110 m from the shore (Figure 1), and recorded meteorological parameters every 15 min during the same time.

Vertical water column profiles were taken with a CTD SBE-19plus (Sea Bird Electronics Inc.) on September 23, 2001, when the hurricane was 300 km to the South, and again on September 27, 2001, when the center of the hurricane had just passed and was 350 km to the Northwest.

Vertical profiles were taken at two sites on the shelf (see Figure 1), near the mooring (38 m depth, point 1), and at an offshore site, 2 km from the coast (120 m depth, point 2). Meteorological, mooring and CTD cast data were analyzed using the included instrument programs and further analyzed in Matlab 2010 (Mathworks Inc.) and Fortran 90.

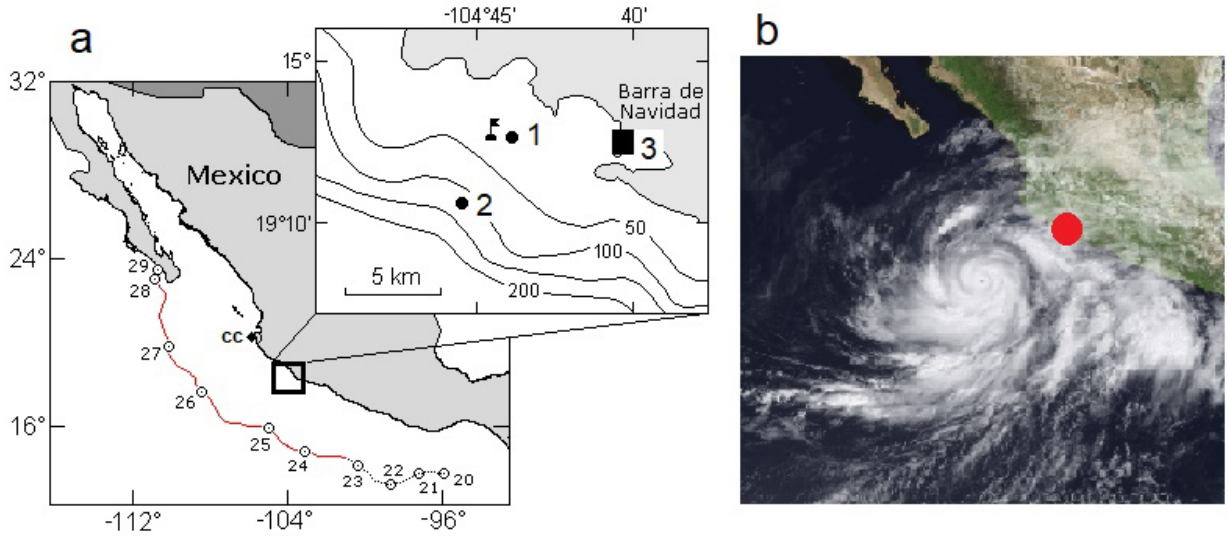

Figure 1. a) The study site, marked with a square, on the continental shelf in the central Mexican Pacific near Barra de Navidad, Jalisco, and a black arrow marking Cabo Corrientes to the north of the study site, with the trajectory of hurricane Juliette shown with the red line on different days of September 2001. The inset shows the mooring deployment of the SBE 16 (marked with a flag), the CTD profile cast sites (points 1 and 2), and the meteorological station (3) position near Barra de Navidad. b) The location of Hurricane Juliette on September 27, 2001, with the red circle showing the study site underneath the cloud cover.

Results

Tropical storm Juliette appeared on September 21, 2001, 265 km Southwest of Tapachula, Mexico (centered at approximately 13.4° N, 94° W) with a maximum wind speed of 85 km h^{-1}, wind gusts of up to 110 km h^{-1} and a minimum pressure of 996 hPa (www.nhc.noaa.gov). On the morning of September 23, 2001, Juliette intensified to a hurricane. From September 24 to 27, 2001, Juliette maintained a predominantly West-Northwest trajectory, increasing to a Category 4 on the Saffir-Simpson scale. On the morning of September 26, wind speeds reached 230 km h^{-1}, with gusts of 285 km h^{-1} and minimum pressure of 923 hPa at a distance of approximately 430 km to the Southwest of Cabo Corrientes (in the state of Jalisco, Mexico) (Figure 1, 2).

The vertical CTD profiles of temperature and salinity taken at the coast show that the pycnocline at our shallowest sampling site disappeared due to vertical and horizontal mixing after the passage of the hurricane, with a uniform layer of temperature and salinity throughout the entire water column.

This resulted in a decrease in surface temperature by 4 °C and an increase in surface salinity by 0.4 PSU, whereas at depth, the opposite pattern occurred, with similar magnitude (Figure 3a). At the deeper sampling site, surface layers also decreased in temperature and increased in salinity to 20 m depth, again with the opposite occurring below 20 m, showing a homogeneous mixed layer down to about 40 m depth (Figure 3b). The temperature and salinity profiles gradually restored their normal shape below 80 m (Figure 3b).

During the movement of the hurricane through the measurement area (see boxed area in Figure 4a-d), the wind increased from 5-7 m s^{-1} to more than 20 m s^{-1}, with an average stabilized direction of 85 degrees (west), from the morning of September 25 to the afternoon of September 27 (Figure 4c,d),

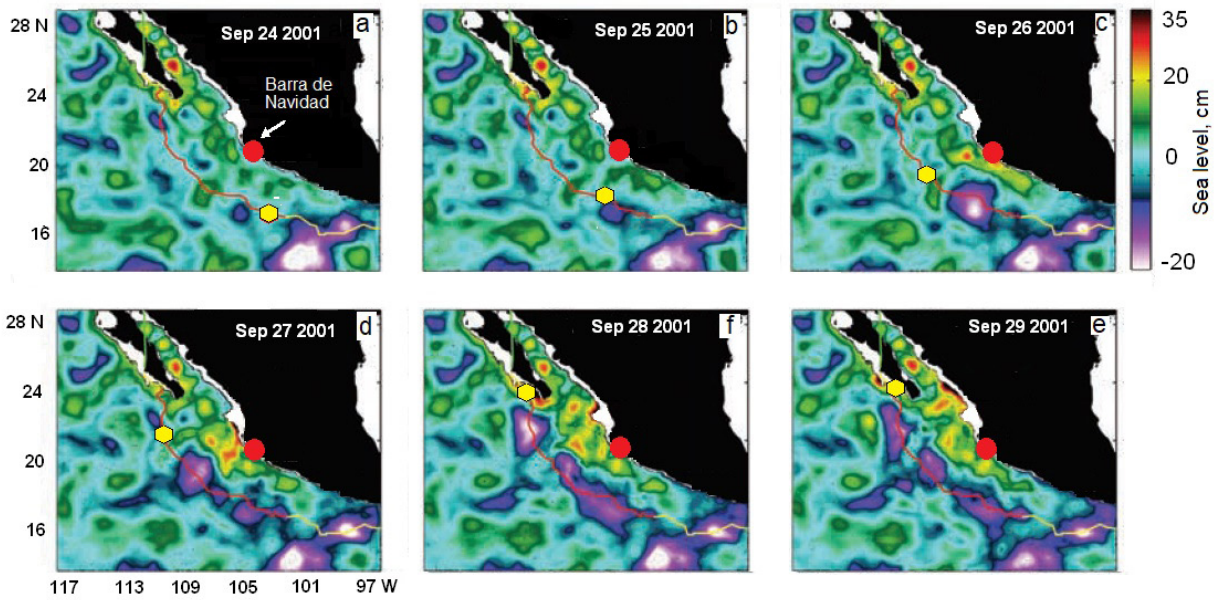

Figure 2. Sea surface height anomaly (colored contours in cm) from September 24 - 29, 2001 when Hurricane Juliette moved along the west coast of central Mexico (adapted from Zamudio *et al.*, 2002). The red circle marks the location of the study site near Barra de Navidad, Jalisco, and the yellow hexagon indicates the position of the hurricane center for each day.

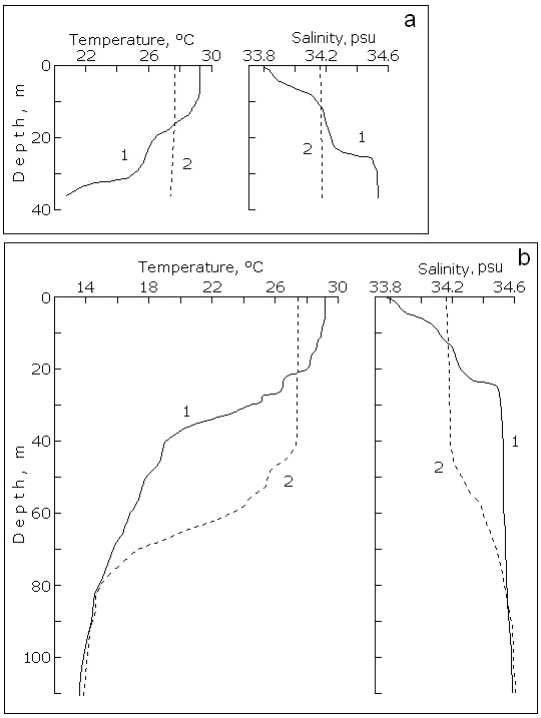

Figure 3. Temperature and salinity vertical water column profiles measured near the mooring (point 1 on Figure 1a) (a), and at the offshore site (point 2 on Figure 1a) (b), on September 23 (continuous line, marked 1) and on September 27 (dashed line, marked 2), 2001, before and after the passing of hurricane Juliette.

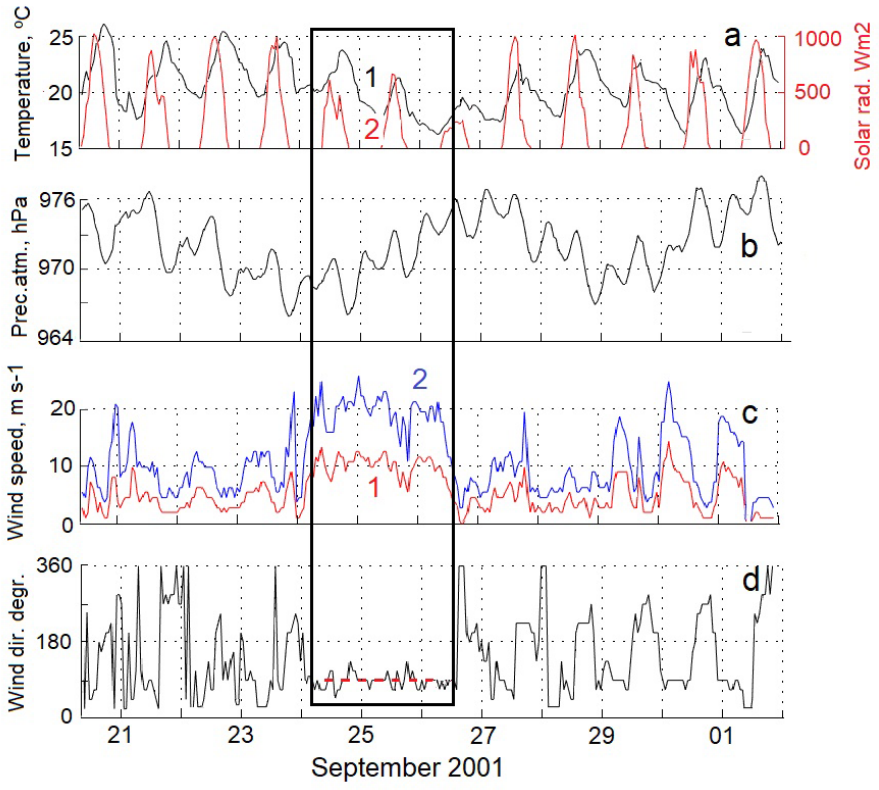

Figure 4. a) Temporal variation of air temperature (black curve, marked 1), solar radiation (red curve, marked 2), atmospheric pressure (b), wind speed (c) (with the red line marked 1 showing hourly averaged wind speed and the blue line marked 2 showing wind gusts), and wind direction (d) from an automatic weather station installed at the shore. The boxed area marks the time interval corresponding to the passage of the eastern edge of the hurricane through the study area, with the red dotted line in panel (d) showing the directional wind stability at that time.

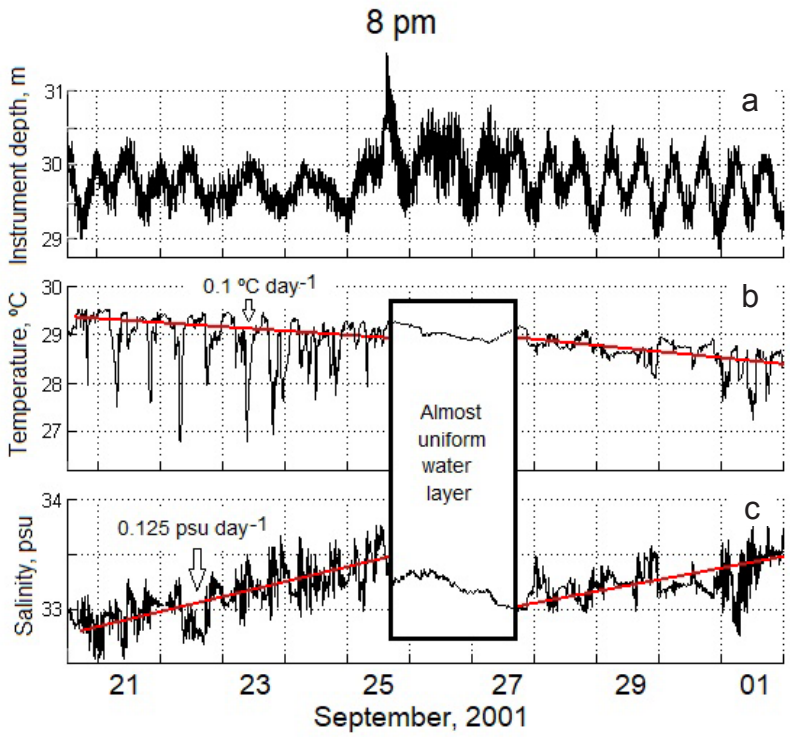

Figure 5. Time series at the mooring, measured by the SBE-16m showing, a) instrument depth, b) water temperature, and c) salinity. Instrument depth was de-tided and corrected for the atmospheric pressure load effect. The red lines in panels b and c show the general trend by smoothing with a 25-hr cosine filter. The boxed area represents the time of maximum hurricane impact off the coast of the state of Jalisco, Mexico, and clearly shows the abrupt mixing and stabilization of the water column, with reduced thermal variability during this time.

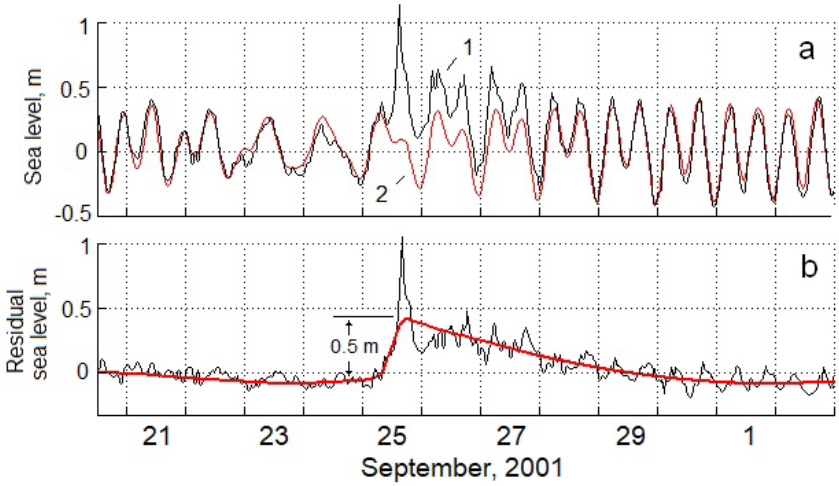

Figure 6. a) Sea level fluctuations in the mooring area showing, 1) hourly sea level fluctuations measured with the moored CTD SBE-16 in black, and, 2) predicted tidal fluctuations in red (CICESE, Mar Tidal Prediction Program, for the Manzanilla site, 25 km to the south of our instrument site), and b) residual sea level. The red line in panel (b) shows the residual level trend smoothed by a 36-hr cosine filter.

which contributed to the upwelling documented shortly thereafter in the water column (Figure 3a,b). At the same time, the air temperature cooled, with high clouds and a decrease in the solar radiation from 1000 to almost 230 Wm^2, and a significant drop in atmospheric pressure just before the increase in the wind, on the night of September 24 (Figure 4a,b).

The mooring measurements showed that sea level began to decrease slightly about four days before the arrival of the hurricane, yet by the evening of September 25, it rose abruptly by 50 cm (Figure 5a, 6a), just before the mixing of the water column resulted in the marked reduction in thermal variability and an almost uniform water layer at the depth of the moored instrument, lasting from the nights of September 25 to 27 (see boxed area in Figure 5b, c). Model calculations (see Figure 2c,e) showed coastally trapped waves present at the shelf edge on September 26 and 27, with a corresponding sea level rise of 20-25 cm, and our mooring measured a total rise in sea level exceeding 1 m. The over-tiding occurred for 4 to 5 days, during the time the area was under the influence of the hurricane (Figure 6a,b).

Discussion

In situ nearshore oceanographic and meteorological data taken on the coast of the Mexican Eastern Tropical Pacific during the passage of Hurricane Juliette in 2001 showed the expected pattern of upwelling, mixing, and sea level rise, with the potential effects of coastally trapped waves confounded in the sea level signal. The vertical pattern of surface cooling and warming at depth in the nearshore water column is common on the right side of the track of cyclones (Wu *et al.*, 2020). Zamudio *et al.* (2010) also showed the mixed layer reaching down to 40 m depth along the Southeastern coast of the Baja California peninsula, similar to what we found, and confirmed the nearshore *in situ* surface cooling with the broader signature of upwelling using satellite chlorophyll measurements.

The breakdown of stratification measured in the vertical profiles resulted in a notable reduction in the thermal variability of the water column during hurricane passage in the mooring instrument time series. The variability in the water column measured prior to and after the hurricane passed showed abrupt cold-water pulses occurring at the mooring, with over 2°C temperature drops in a matter of minutes, which have been characterized previously as part of the semidiurnal internal tidal signal in this region (Filonov *et al.*, 2000; Filonov and Konyaev, 2003; Filonov and Tereshchenko, 2003). This internal wave signal abruptly disappeared as the wave guide was broken down with the disappearance of the pycnocline and reappeared once stratification was re-established. This type of turbulent mixing is common within one radius of maximum hurricane winds, where stratification is often destroyed (Keen and Glenn, 1999), and it is well known that internal tidal fluctuations require stratified waters (Winant, 1974).

The simulated ocean level changes and position of Hurricane Juliette as it moved along the Mexican coast (Zamudio *et al.*, 2002; 2010) showed the formation of coastally trapped waves that propagated poleward along the Pacific coast of the mainland Mexico coast and into the Gulf of California. Model calculations from Zamudio *et al.* (2002) show coastally trapped waves present at the edge of the shelf near our *in situ* study site on September 26 and 27. In our time series, we clearly see over-tides measured as an abrupt sea level rise of almost 50 cm, which coincided with a higher tide period and lasted 4 to 5 days. Unfortunately, we were unable to tease apart the role of second-order coastally trapped waves in mixing and sea level fluctuations in our measurements from the first-

order sea surface elevation surge effects (Hubert *et al.* 1991). Multilayer ocean models have been used to numerically simulate the response of the baroclinic shelf to a moving hurricane along the western coast of Mexico and the Gulf of California (Gjevik, 1991; Gjevik and Merrifield; 1993) and show similar storm response features in the shelf region, such as narrow-band oscillations of barotropic shelf waves, near the inertial period, and long periodic baroclinic wave modes. Over-tides are common during extreme atmospheric events (Paniagua-Arroyave *et al.*, 2019), and combined approaches of both *in situ* measurements and modeling might help to tease apart their causes.

The results presented herein are limited yet are unique in that they expand on the models previously presented during this hurricane passage with *in situ* measurements taken on the open coast. Measuring *in situ* oceanographic changes under different atmospheric influences, such as hurricanes, is critical for informing coastal models and further understanding water column impacts of hurricanes.

Conclusion

In situ nearshore oceanographic and meteorological data on the coastline of the Mexican Eastern Tropical Pacific during the passage of Hurricane Juliette in 2001 showed the expected pattern of mixing and sea level rise, however it was difficult to separate the effects of surge from coastally trapped waves, and a combined approach of modeling and *in situ* data is recommended going forward. Although models are a useful approach to estimate oceanic conditions during hurricane passage when *in situ* measurements are difficult and dangerous to obtain, they cannot resolve hurricane effects on the shelf and very near the coast. *In situ* meteorological and oceanographic characteristics can fill this gap in understanding and might be particularly relevant for understanding coastal vulnerability and the coupling processes between the atmosphere and the coastal shelf off the Pacific coast of central Mexico.

Acknowledgments

This project was financially supported by Mexican National Science Foundation (CONACyT) projects 35553-T and 46674. The authors would like to thank Maxim Vasililiev for field assistance.

References

Asher, T., Luetticj, A., Felming, A., Blanton, B. 2019. Low frequency water level correction in storm surge models using data assimilation. *Ocean Modelling*, 144, 101483.

Badan, A. 1998. Coastal Circulation from the Galapagos to the Gulf of California, The Sea, vol. 11. The Global Coastal Ocean, Regional Studies and Syntheses, edited by A. R. Robinson and K. H. Brink, 315-343, John Wiley, Hoboken, N. J., USA.

Brink, K.H., 1991. Coastal-trapped waves and wind-driven currents over the continental shelf, *Annu. Rev. Fluid Mech.*, 23, 389-412.

Christensen, N., Jr., R. de la Paz, G., Gutierrez, A. 1983. study of sub-inertial waves off the west coast of Mexico, *Deep-Sea Res.*, 30, 835 – 850.

Dukhovskoy, D.S, Morey, S.L., O'Brien, J.J. 2009. Generation of baroclinic topographic waves by a tropical cyclone impacting a low-latitude continental shelf. *Continental Shelf Research* 29, 333-351.

Enfield, D.B., Allen, J.S. 1983. The Generation and Propagation of sea level variability along the Pacific Coast of Mexico, *J. Phys. Oceanogr.*, 13, 1012-1033.

Fiedler, P. C. 1992. Seasonal climatologies and variability of Eastern Tropical Pacific surface waters. *NOAA Technical Report NMFS* 109, 65pp.

Fiedler, P. C., Talley, L. 2006. The hydrography of the eastern Tropical Pacific: a review. *Progr. Oceanogr*, 69, 181-217

Fiedler, P.C. 2002. The annual cycle and biological effects of the Costa Rica Dome. *Deep-Sea Res.*, I, 49, 321-338.

Filonov, A.E., Konyaev, K.V. 2003. Nonlinear Internal Waves near Mexico's central pacific Coast. In Nonlinear Processes in Geophysical Fluid Dynamics (Velasco-Fuentes, O.U. *et al.*, eds). Kluwer Academic Publishers, 377-386.

Filonov, A.E., Tereshchenko, I.E. 2000. El Niño 1997-98 Monitoring in Mixed Layer of the Western Coast of Mexico. *Geophys. Res. Lett.*, 27, 705-710.

Filonov, A.E., Tereshchenko, I.E., Monzón, C.O., González-Ruelas, M.E., Godínez-Domínguez, E. 2000. Seasonal variability of the temperature and salinity fields in the coastal zone of the states of Jalisco and Colima, Mexico. Ciencias Marinas, 26, 303-321.

Gjevik, B., 1991. Simulation on shelf sea response due to travelling storms, *Contin. Shelf Res.*, 11,139-166.

Gjevik, B., Merrifield, M.A. 1993. Shelf-sea response to tropical storm the west coast of Mexico. *Contin. Shelf Res.*, 13, 25-47.

Guang-Bing, Y., Lian-Gang, L. Zhan-Peng, Z., Xue-Jun, X., Guan-Suo, W., Yan-Liang, G., Long, Y., De-Jing, M. 2017. Cruise observation of shallow water response to typhoon Damrey 2012 in the Yellow Sea, *Continental Shelf Research*, 148, 1-8.

Hughes, C.W., Fukumori, I., Griffies, S.M. 2019. Sea Level and the Role of Coastal Trapped Waves in Mediating the Influence of the Open Ocean on the Coast. *Surv Geophys* 40, 1467–1492.

Jaregui, E. 2003. Climatology of landfalling hurricanes and tropical storms in Mexico. *Atmosfera* 16, 193-204.

Keen, T., Glenn, S. 1999. Shallow water currents during hurricane Andrew, *Journal of Geophysical Research-Oceans*, 104, C10, 23443-458.

Kessler, W. S. 2002. Mean three-dimensional circulation in the Northeastern Tropical Pacific. *J. Phys. Oceanogr.*, 32: 2457-2471.

Kessler, W. S. 2006. The circulation of the eastern Tropical Pacific: a review. *Progr. Oceanogr.*, 69, 181-217.

Lavín, M. F., Beier, E., Gómez-Valdés, J., Godínez, V. M., and García, J. (2006), On the summer poleward coastal current off SW México, *Geophys. Res. Lett.*, 33, L02601

Levinson, D., Vickery, P., Resio, D. 2010. A review of the climatological characteristics of landfalling Gulf hurricanes for wind, wave, and surge hazard estimation. *Ocean Engineering*, 37: 13-25.

Mallin, M.A., Corbett, C.A. 2006. How hurricane attributes determine the extent of environmental effects: Multiple hurricanes and different coastal systems. *Estuaries and Coasts*, 29, 1046-1061.

Miles, T., Seroka, G., Kohut, J., Schofield, O., Glenn, S. 2015. Glider observations and modeling of sediment transport in Hurricane Sandy, *J. Geophys. Res. Oceans*, 120, 1771– 1791.

Miller, R., Stone, G. W. 2001. A Climatology of Tropical Storm and Hurricane Strikes to Enhance Vulnerability Prediction for the Southeast U.S. Coast. *Journal of Coastal Research*, 17, 949-956.

Paniagua-Arroyave, J. F., Valle-Levinson, A., Parra, S. M., Adams, P. N. 2019. Tidal distortions related to extreme atmospheric forcing over the inner shelf. *Journal of Geophysical Research: Oceans*, 124, 6688-6701.

Reffitt, M., Orescanin, M., Massey, C., Raubenheimer, B., Jensen, R., Elgar, S. 2020. Modeling storm surge in a small tidal wo-inlet system. *Journal of Water*, 146, 04020043.

Simpson, R., Riehl, H. 1981. The hurricane and its impact. Louisiana State University Press and Basil Blackwell, 398 pp.

Trepanier, J.C, Ellis. K.N, Tucker, C.S. 2015. Hurricane Risk Variability along the Gulf of Mexico Coastline. *PLOS ONE* 10(3): e0118196.

Valle-Levinson, A., Olabarrieta, M., Heilman, L. 2020. Compound flooding in Houston-Galveston Bay during Hurricane Harvey. *Sci Total Environ*.10;747:141272.

Winant, C.D. 1974. Internal surges in coastal waters. *J Geophys Res* 79: 4523–4526.

Wu, R, Zang. H., Chen D. 2020. Effect of Typhoon Kalmaegi (2014) on northern South China Sea explored using Muti-platform satellite and buoy observations data. *Progress in Oceanography*, 180, 102218.

Wyrtki, K. 1965. Surface Currents of the Eastern Tropical Pacific Ocean. *Bull. Inter-American Tropical Tuna Commission*. Vol. IX. (5), 269-304.

Wyrtki, K. 1966. Oceanography of the Eastern Equatorial Pacific Ocean. *Oceanography Marine Biological Annual Rev.*, 33-68.

Wyrtki, K. 1967. Circulation and Water Masses in the Eastern Equatorial Pacific Ocean. Int. Journal Oceanology Limnology. 1, 117-147.

Zamudio, L., Hurlburt, H.E., Metzger, E.J., Smedstad, O.M. 2002. On the evolution of coastal trapped waves generated by Hurricane Juliette along the Mexican Coast, *Geophys. Res. Lett.* 29, 2141.

Zamudio, L., Leonardi, A., Meyers, S., O'Brien, J. 2001. ENSO and eddies on the southwest coast of Mexico. *Geophys. Res. Lett.*, 28, 13-16.

Zamudio, L., Metzger, E.J., Hogan, P. 2010. Gulf of California response to Hurricane Juliette. Ocean Modelling 33, 20-32.

Zang, H., Chen D. 2020. Effect of Typhoon Kalmaegi (2014) on northern South China Sea explored using Muti-platform satellite and buoy observations data. *Progress in Oceanography*, 180, 102218.

Zhang, F., Emanuel, K. 2018. Promises in air-sea fully coupled data assimilation for future hurricane prediction. *Geophysical Research Letters*, 45, 13,173– 13,177